Integration of Functional Materials into Microfluidic Devices for Fluidic Control and Sensing

Janire Sáez Castaño[1]

Thesis submitted for the Degree of Doctor of Philosophy

Supervisor: Dr. Fernando Benito López[1]

Prof. Luis Ángel Fernández Cuadrado[2]

[1]Analytical Microsystems & Materials for Lab-on-a-Chip (AMMa-LOAC) Group, Microfluidics Gluster UPV/EHU, Analytical Chemistry Department, University of the Basque Country UPV/EHU, Vitoria-Gazteiz, Spain.

[2]Ikerkuntza eta Berrikuntza Analitikoa (IBEA) Group, Analytical Chemistry Department, University of the Basque Country UPV/EHU, Leioa, Spain.

eman ta zabal zazu

Universidad del País Vasco
Euskal Herriko Unibertsitatea

November 2017

“It always seems impossible until it is done”

Nelson Mandela

Declaration

I hereby certify that this material, which I now submit for assessment on the programme of study leading to the award of Doctor of Philosophy is entirely my own work, and that I have exercised reasonable care to ensure that the work is original, and does not, to the best of my knowledge, breach any law of copyright, and has not been taken from the work of others save and to the extent that such work has been cited and acknowledged within the text of my work

Signed: ______________________

Janire Sáez Castaño

ID No.: _____________________

Date: ________________________

Summary

Water is a key resource for human well-being and, in nature, is an essential food source, responsible, among many other things, of vegetables growth. Therefore, the monitoring of water quality is of great importance for society. In this thesis, a future with highly effective autonomous sensors that are able to measure and share information about the quality of our environment, particularly the water masses, is pursued. In this way, different modules have been developed in order to contribute to the monitoring of water quality with low cost and rapid fabrication technologies. In order to drive down the costs associated with the manufacturing of conventional components, smart materials have been implemented into microfluidic devices to get fluidic control and sensing.

Resumen

El agua es una fuente clave para el buen estado de las personas y, en la naturaleza, es una fuente nutritiva esencial responsable del crecimiento de la vegetación. Por ello, la monitorización de la calidad del agua es de gran importancia para la sociedad. En esta tesis se pretende contribuir a un futuro donde sensores altamente autónomos y eficaces sean capaces de medir y compartir la información de la calidad de nuestro medioambiente, en particular, de las diferentes matrices de agua. En este sentido, se han desarrollado diferentes módulos para contribuir a la monitorización continuada de la calidad del agua mediante el empleo de tecnologías de bajo coste y de rápida fabricación. Para conseguir reducir los costes asociados a la producción de componentes convencionales, se ha implementado el uso de materiales inteligentes dentro de dispositivos microfluídicos para conseguir el control fluídico y sensorización.

Laburpena

Ura funtsezko elementua da naturan, landareen hazkunderako edota gizakiaren ongizate eta osasun-egoera bermatzeko elikagai-iturri ezinbestekoa delako. Horregatik, uraren kalitatea kontrolatzea oso garrantzitsua da gizartearentzat. Zentzu horretan, ingurugiroaren kalitatea hobetzeko ekarpen bat egitea da tesi honen helburua, non ur matrize ezberdinen kalitateari buruzko informazioa neurtzeko eta partekatzeko gai diren sentsore autonomo eta eraginkorrak aurkezten diren. Uraren kalitatearen etengabeko jarraipenerako, hainbat modulu garatu dira kostu baxua bermatzen duten fabrikazio-teknologia azkarren bidez. Halaber, ohiko osagaiei lotutako kostuak murrizteko, emarien kontrola eta sentsorizazioa ahalbidetzen duten material adimendunak integratu dira gailu mikrofluidikoen barnean.

Contents

1

Aim and Outline of the Thesis

1.1 General Introduction

Water is the key molecule for life and ecosystems survival. It can be found in almost any place on Earth in the three different physical states of matter (solid, liquid and gas). Particularly for humans, potable water is capital to avoid diseases and ensure a proper quality of life. On the other hand, water in nature is an essential food source, being, along with light and nutrients, the responsible of vegetable growth. Therefore, continuous monitoring of water within water resources such as continental water, seawater, wastewater and drinking water is essential. Physico-chemical parameters such as temperature, pH, salinity, oxygen balance, acid neutralising capacity, and nutrient concentrations (nitrates and nitrates, phosphates, ammonium, silicates, etc.) need to be known and controlled to ensure an optimal water quality.

Traditionally, water samples are collected at the point of need and transported to specialised analytical laboratories for quality control. Spectroscopic (ultraviolet/visible[1], fluorescent[2], atomic[3], Raman[4] detection), electrochemical (by using ion-selective electrodes for the determination of water ions as magnesium, chloride, fluoride, nitrate and pH[5]), and chromatographic techniques such as gas chromatography/mass spectroscopy (GC-MS) and high performance liquid and ultra-high performance liquid chromatography (LC/HPLC/UHPLC) are commonly used to determine the analyte of interest present in the water sample[6]. Moreover, induced coupled plasma (ICP) techniques coupled with different detectors can be useful for the analysis of traces of metals[7, 8] in water. The main disadvantages of these analytical techniques are that they do not generally allow *in-situ* analysis, which is of major importance for the monitoring of pollutants in water due to their fast degradation.

Therefore, a future with highly effective autonomous sensors that are able to measure and share information about the quality of our environment, particularly the water masses, deployed in lakes and rivers, water supply systems and even in municipal and industrial wastewater treatment plants, is still a utopia. Ideally, these sensors would be densely deployed at multiple locations, and the information made available to citizens through the Internet.

Unfortunately, science and technology cannot deliver an effective platform to make this idyllic vision a reality yet, and the gap between what is currently available, and what is actually needed remains significant. Huge efforts to develop innovative sensors over the past 20 years have been made, which have generated thousands of papers in the literature[9], without delivering yet a practical solution to the real issues associated with distributed environmental sensing. In recent years, many of these papers describe the ingenious use of nanostructured materials[10-12], which, under controlled laboratory conditions, exhibit greatly improved characteristics compared to conventional sensors. Therefore, these new types of sensors have the potential to improve environmental analysis systems.

The current state-of-the-art for autonomous environmental sensors to monitor the chemical and biological status of our water resources is based on flow systems that employ conventional pumps, valves and fluid handling components, and because of this, these systems are very expensive (often > €20K per unit) and therefore the traditional deployment model is inherently not scalable. The key to change this model is to drive down the unit cost, making autonomous chemical sensors available for €20 or €2, not €20.000 per unit cost.

Figure 1.1 presents the strategy followed in this thesis: (1) to use evolutionary improvements in existing platforms to drive the cost down and at the same time improve reliability and, thus, promote scalability and (2) to use real scalable sensors and actuators that can be fabricated through revolutionary breakthroughs that emerge from fundamental materials science research (the main focus of this thesis).

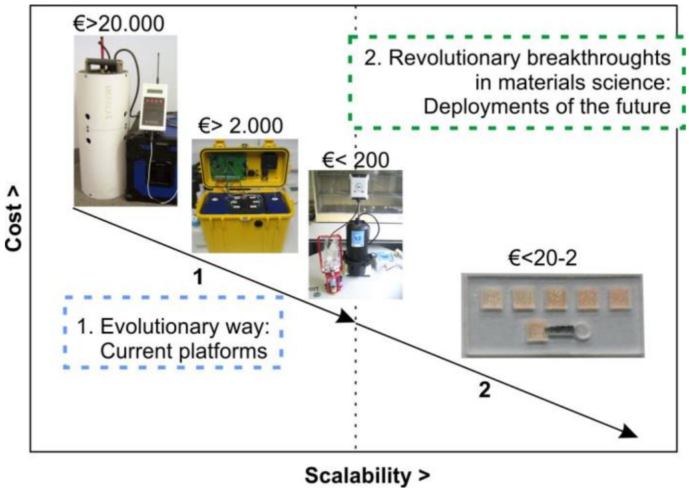

Figure 1.1: Overall strategy of the proposal for this thesis.

1.2 Aim and Chapter Overview

This thesis aims to contribute to the development of sensors and components for Lab-on-a-Chip (LOC) applications at low cost, pursuing sensor autonomy, in order to be able to achieve microfluidic devices for *in-situ* analysis. These sensors and components will be fabricated by rapid prototyping techniques with integrated smart materials. These smart materials are in some cases used as the sensing area where the analyte can be detected and, in other cases, the materials will act as active components that perform actuation for fluid control and handling in the microfluidic device. In order to prove the suitability of the developed systems, each microfluidic device will be designed and tested with the intention to be used in real environmental scenarios. Therefore, the aim of this thesis is to investigate different aspects of microfluidic technology, such as microfluidic fabrication, microactuators and sensors integration, combining microtechnology and materials science, in order to generate autonomous analytical systems for the continuous monitoring of water quality (*e.g.* detection of bacteria and nutrients).

To reach the stated main goals, the following sub-objectives have been established:

- To investigate new fabrication protocols, by using the Origami technique, for the fabrication of low-cost microfluidic devices.
- To integrate smart materials into microfluidic devices that will perform as actuators and sensors. In particular, these smart materials will be integrated as:
    - Biocompatible hydrogels, for the *in-situ* generation of valves.
    - Photoswitchable ionogel-based actuators, for flow control in Lab-on-a-Disc devices.
    - Thermoresponsive actuators, for flow control.
    - Perfluorinated polymers as phantom membranes or beads for pollutants sensing.
    - Ionogel-based sensors for nitrite and nitrate sensing.

1.3 Chapter overview

A detailed overview of each chapter, together with particular contributions from research collaborators (where applicable), are given below:

Chapter 2 provides a general overview on microfluidics, focusing in polymeric microfluidics. It also defines and explains the different functional materials used in this thesis, when integrated into microfluidic devices and their applications. Finally, the chapter describes the state-of-the-art on microfluidic devices and platforms for environmental sensing in real water samples.

In **Chapter 3** the fabrication of easy and cheap hybrid microfluidic devices by the *Origami* technique is discussed. This fast fabrication method was applied, as a proof of concept, for the generation of a micromixer with 3D stepped serpentine design.

Chapter 4 deals with the on-demand, generation and removal of alginate microvalves into microfluidic devices with biocompatible capabilities for fluidic control. The microfluidic devices were fabricated using the *Origam*i technique by folding several layers of cyclic olefin polymer followed by thermocompression bonding. The hydrogels could be dehydrated at mild temperatures or chemically erased using ethylenediaminetetraacetic acid disodium salt solution to completely open the channel, ensuring the reusability of the whole device.

Chapter 5 describes the fabrication and the performance of a reusable photoswitchable ionogel-based actuator *in-situ* photopolymerised into a disc platform for flow control. During storage and spinning, the swollen actuator provides a permanent liquid barrier due to the specific chemical characteristics of the ionogel. The actuator is easily actuated using a white light LED allowing selected channel opening at the desired time. The actuation mechanism is chemically reversible when an acid solution is provided to the actuator through a perpendicular channel.

Chapter 6 describes the characterisation and performance of thermoresponsive crosslinked tributylhexyl phosphonium sulfopropylacrylate poly(ionic liquid) (PILc) hydrogels as temperature controlled valves in microfluidic devices.

The synthesis of the PILc hydrogels and their characterisation was carried out in collaboration with Dublin City University (DCU) in Ireland, in particular with Dr Alexandru Tudor, Professor Dermot Diamond and Dr Larisa Florea.

Chapter 7 presents the integration of perfluorinated membranes with a refractive index similar to that of water hosted in a novel multilayer cyclic-olefin polymer and pressure sensitive adhesive hybrid microfluidic device. The membrane enables combining filtration and label-free sensing of pollutants in environmental water samples. The sensing capabilities of the device were tested with real water samples containing a lot of particles, without showing clogging of the membrane and enabling nonspecific quantification of pollutants in few minutes.

The material for the membrane and performance of the final device were carried out in collaboration with Università Degli Studi di Milano in Milan, in particular with Dr Roberta Lanfranco, Emanuele Di Nicolò and Professor Marco Buscaglia.

In **Chapter 8** the integration of innovative amorphous perfluorinated polymers as microbeads for surfactant detection in water in a microfluidic device is demonstrated. It describes the fabrication and characterisation of phantom microbeads integrated into the microfluidic device, for the easy and non-invasive optical detection of surfactants in water in a continuous mode.

The microbeads synthesis and the performance of the device were carried out in collaboration with Università Degli Studi di Milano in Milan, in particular with Dr Roberta Lanfranco, Deborah Abati and Professor Marco Buscaglia.

Chapter 9 deals with a novel hand-held device for nitrite and nitrate detection in water using an ionogel-based colorimetric sensor. The sensor consists of a small poly(methyl)methacrylate device cut by CO_2 laser system where both the detection and the calibration zones are integrated. A simple photograph of the whole device, followed by colour processing of the different sections of the device was used for the determination of nitrite concentrations.

Finally, in **Chapter 10** the final remarks and future work is presented.

1.4 References

1 B. S. Gentle, P. S. Ellis, M. R. Grace and I. D. McKelvie, *Anal. Chim. Acta,* 2011, 704, 116-122.
2 C. Erger and T. C. Schmidt, *TrAC Trends Anal. Chem.,* 2014, 61, 74-82.
3 D. Kusic, B. Kampe, P. Rosch and J. Popp, *Water Res.,* 2014, 48, 179-189.
4 S. G. Silva, J. A. Nóbrega, B. T. Jones and G. L. Donati, *Microchem. J.,* 2014, 117, 250-254.
5 A. Lewenstam, M. Maj-Zurawska and A. Hulanicki, *Electroanal.,* 1991, 3, 727-734.
6 W. B. Wilson, U. Hewitt, M. Miller and A. D. Campiglia, *J. Chromatogr. A,* 2014, 1345, 1-8.
7 M. J. Duane and S. Facchetti, *Sci. Total Environ.,* 1995, 172, 133-144.
8 D. V. Biller and K. W. Bruland, *Mar. Chem.,* 2012, 130–131, 12-20.
9 V. A. VanderNoot, R. F. Renzi, B. P. Mosier, J. L. Van de Vreugde, I. Shokair and B. L. Haroldsen, *Electrophoresis,* 2010, 31, 2632-2640.
10 F. E. Legiret, V. J. Sieben, E. M. Woodward, S. K. Abi Kaed Bey, M. C. Mowlem, D. P. Connelly and E. P. Achterberg, *Talanta,* 2013, 116, 382-387.
11 V. M. Rerolle, C. F. Floquet, A. J. Harris, M. C. Mowlem, R. R. Bellerby and E. P. Achterberg, *Anal. Chim. Acta,* 2013, 786, 124-131.
12 M. Czugala, R. Gorkin 3rd, T. Phelan, J. Gaughran, V. F. Curto, J. Ducree, D. Diamond and F. Benito-Lopez, *Lab Chip,* 2012, 12, 5069-5078.

2

Microfluidics and Smart Materials: Application in Environmental Monitoring*

This Chapter provides a general overview on microfluidics, focusing in polymeric microfluidics. It also defines and explains the different functional materials used in microfluidic devices and its applications. Finally, the chapter describes the state-of-the-art on microfluidic devices and platforms for environmental sensing in real water samples.

---

*Parts of this Chapter have been published in: T. Akyazi; J. Saez; A. Tudor; C. Delaney; W. Francis; D. Diamond; L. Basabe-Desmonts; L. Florea; F. Benito-Lopez, Application of Ionic Liquid Materials in Microfluidic Devices, Ionic Liquids Devices, The Royal Society of Chemistry, Smart Materials N° 28, *Ed:* Ali Eftekhari, 2018, 234-271.

2.1 Introduction

Miniaturisation is a leading strategy followed in many research areas in both science and technology. The general advantages of miniaturisation are the possibility of increasing performance, save time, space, cost and materials by integrating miniaturised components. Miniaturisation provides with tools and fabricated devices in which an elevated number of functionalities per square millimeter can be allocated[1].

In the areas of chemistry and life sciences, the introduction of microfluidics technology has allowed for the miniaturisation of bio-chemical processes, mainly for (bio-)analytical applications. Microfluidic devices are defined as miniaturised reaction containers fabricated by microtechnology and precise engineering methods, consisting in microchannels with typical diameters in the range of 10 - 500 µm, which are used to manipulate or manage samples or reagent solutions[2, 3]. The goal is to generate devices that automate and include all necessary steps for a defined (bio)-chemical analytical operation such as sampling, sample transport, filtration, dilution, chemical reaction, separation or detection to be carried out; this concept is called micro Total Analysis System (µTAS)[4].

A wide variety of materials and techniques has been used for the fabrication of microfluidic devices. In this regard, fabrication protocols have evolved from processes that manipulate more expensive materials such as silicon and glass to processes easier to implement in conventional laboratories; therefore, they use cheaper polymers such as cyclic-olefin polymer (COP)[5], cyclic-olefin copolymer (COC)[6, 7], the elastomer poly(dimethylsiloxane) (PDMS)[8, 9], poly(methylmethacrylate) (PMMA)[10, 11], and polycarbonate (PC)[12]. For example, PDMS polymer, which is commonly processed by the so-called “soft lithography” fabrication technology, is widely used for the fabrication and fast prototyping of microfluidic devices. In general, PDMS (liquid) is mixed with a cross-linking agent and is poured into a microstructured mould and heated to obtain an elastomeric replica of the mould (cross-linked PDMS), which becomes the microfluidic device when adhered to a flat surface[13].

Commercial suppliers mix polymers with additives to optimise their flow properties as a hot melt during injection moulding. These multi-component commercial materials use trade names and are commonly referred to as plastics[11, 14]. It is important to mention PMMA as one of the plastics that have been most widely used for microfluidics. It is particularly useful because of its low cost, high optical transparency, and well definable electric and mechanical properties. Compared with other polymeric materials, PMMA is the least hydrophobic polymer[10, 15], shows unique absorption characteristics to the infrared regime and is amenable by direct CO_2 ablation systems, which highly simplifies microfluidic fabrication protocols with this material. Other commonly used plastic is PC, which nowadays is frequently used in the fabrication of optical data storage media such as compact disks[16]. Its high durability, strength, temperature resistance, low density and good optical properties have also made PC a popular material for the fabrication of microfluidic devices[17, 18]. In recent years, both cyclic olefin polymers, COP, and COC are the materials that are being used for the fabrication of microfluidic devices. These thermoplastics possess high optical clarity, even into the deep-UV range[19], low water absorption and high resistance to solvents[5, 20-22]. In particular, COP has been used in bioprocesses due to its biocompatibility[21]. In the following Chapters, microfluidic devices will be fabricated using some of the materials described here, in particular, COP and PMMA. Table 2.1 presents the physical and chemical properties of these materials for comparison. When thinking about the design and the fabrication of a microfluidic device for a particular application, the properties of the material used for the fabrication of the device need to be carefully considered prior to fabrication.

Table 2.1: Basic physical and chemical properties of polymeric materials.

Polymeric materials	Tg[1] (°C)	Physical Properties	Chemical Properties	Other Properties	Fabrication Techniques
Polycarbonate (PC)[12]	147	Highly transparent in visible, excellent light transmission.	Resistant against: water, benzene, mineral oils, alcohols, ether, ester.	No biocompatible- Contains harmful Bisphenol A.	Injection moulding. Hot embossing. Laser photoablation.
Cyclic olefin polymer; (COC and COP)[5-7]	123-156	Highly transparent, low autofluorescence, low water absorption. Heat resistance.	Resistant against: acetone, methylethylketone, methanol, ethanol, isopropanol.	Biocompatible.	Injection moulding. Hot embossing.
Polymethylsiloxane (PDMS)[8, 9]	- (elastomer)	Viscoelastic. Transparent. UV resistance. Thermally stable. Deformable.	Resistant against: water, mineral oils, fuel, fatty oils. Chemically inert.	Biocompatible.	Soft-lithography. Direct laser plotting.
Polymethylmethacrylate (PMMA)[10, 11]	85-165	Tensile strength. Transparent. UV resistance. Good abrasion resistance. Low water absorption.	Resistant against: water.	Biocompatible.	Injection moulding. Hot embossing. Laser photoablation. X-ray lithography.

[1] Glass-transition temperature

Moreover, the election of the fabrication technique depends not only on the polymeric material but on the size and aspect ratio of the required features to be implemented as well. Currently, there is a huge variety of methods for the fabrication of microfluidic devices, including hot embossing[14, 23-25], injection moulding[26], laser photoablation[27] or laser micromachining, direct laser plotting[28], and lithography[29], among others. Furthermore, recently developed and low-cost microfabrication techniques based on rapid prototyping techniques, *e.g.* xurography[30, 31] and 3D printing[32, 33] are gaining importance for the development of microfluidic devices [23]. Table 2.2 presents a comparison of the most commonly used techniques for the fabrication of polymeric microfluidic devices.

Table 2.2: Fabrication methods for polymeric microfluidic devices.

Methods	Equipment	Consumables	Advantages	Drawbacks
Hot embossing[14, 23-25]	Hot embosser.	Mould; polymeric material.	Fast; inexpensive.	Needs dedicated press equipment; robust mould (time-consuming).
Injection moulding[26]	Moulds	Thermoplastic pellets; mould.	Large production	Expensive equipment.
Laser photoablation[27]	High-powered pulse laser.	Polymeric material; laser.	Direct-write process.	Not suitable for large production.
Lithography[29]	Lithography; UV lamp, hot plate; printer.	Mask; SU-8; photoresist.	High resolution; sharp barriers.	Expensive equipment, expensive reagents; complex steps.
Xurography[30, 31]	Computer; X-Y plotter.	Polymeric material.	Medium-high resolution, fast fabrication; cheap equipment.	Roughness of the channel walls.
Direct laser plotting[28]	Laser system.	Polymeric material.	Fast, inexpensive; suitable for large production.	Medium-low resolution.
3D-printing[32, 33]	3D printer; UV lamp.	Resin.	Able to generate 3D structures; suitable for large production.	Low resolution.

2.2 General properties of Microfluidic Devices

The small characteristic dimensions of microfluidic devices result in small internal volumes and high surface-to-volume ratios, which lead to improved heat and mass transfer rates. Therefore, it is possible to optimise conventional bio/chemical analytical processes by improving the selectivity, product quality and safety, having at the same time a precise control of the temperature of the process. In addition, diffusive mixing is rapid due to the small length of microfluidic devices, increasing the speed and accuracy of bio/chemical reactions.

Moreover, microfluidic devices use quite a low sample/solvent volume ratio, leading to reduced reagents consumption decreasing the overall costs associated with reagents and allowing precious samples (*e.g*. biomolecules) to be wisely used. Furthermore, waste products are also reduced, so microfluidics can be named as an environmentally friendly type of technology.

Another advantage is the possibility of generating µTAS, due to the high integration capabilities of microfluidics, where different fluidic operations can be integrated into a miniaturised system by exploiting appropriate fabrication technologies. Indeed, a µTAS, also called as lab-on-a-chip (LOC) system, aims to the shrinking of an entire laboratory to a chip format, see Figure 2.1. This novel formatting saves protocol times, reduces risks of sample losses or contaminations and reduces costs by avoiding the use of bulky expensive laboratory instrumentation. Furthermore, microfluidics allows for full automation, thus increasing throughput, improving ease of use and repeatability by reducing human errors. Automation is especially useful in remote operation, performing continuous monitoring of biological or chemical analysis in inaccessible locations.

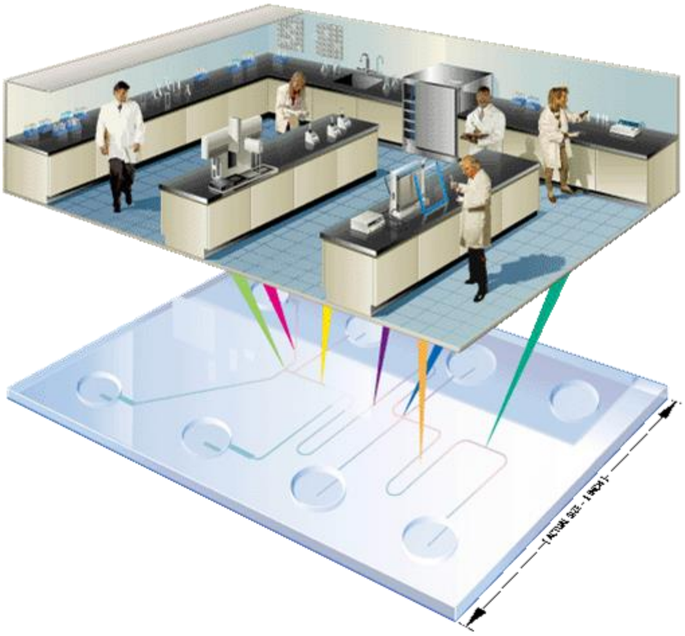

Figure 2.1: Concept of Lab-on-a-Chip (LOC)[34].

Integrated microfluidic devices also offer the feature of portability, enabling *in-situ* analysis at the point-of-care (POC)[35]. POC is defined as an *in-situ* medical diagnostic testing, that is, at the time and place for the patient or environmental care. Examples of these tests are the pregnancy test or the glucose test for diabetic patients. POC analysis reduces costs, time and sample contamination. If microfluidic devices were cheaply produced, devices could be disposable, eliminating cross contamination between tests.

From the physical point of view, forces at the macro-scale interact in a different way than at the micro-scale. As an example, surface effects, which are often neglected at the macro-scale, become increasingly dominant when size is diminished, while volume forces and gravity, which are essential in our daily life, become unimportant in microfluidics.

A parameter to be considered in microfluidics is the Reynolds number, which is a non-dimensional parameter that gives the ratio of the inertial forces to the viscous forces. The Reynolds number is given by the Equation 2.1:

$$Re = \frac{\rho u L}{\mu} \tag{2.1}$$

where ρ is the density of the fluid, u the average velocity, L the characteristic length for the flow and μ the viscosity. In microfluidics, the critical dimension, which is often the channel height, becomes increasingly small corresponding with small Reynolds numbers. Thus, the ratio of inertial forces to viscous forces decreases, indicating that the viscous forces dominate over the inertial forces at these length scales[36]. Due to the small dimensions of microchannels, the Re is usually smaller than 100, often less than 1. In this Reynolds number regime, flow is completely laminar, and no turbulence occurs. The transition to turbulent flow generally occurs in the range of Reynolds number 2000. Laminar flow provides a means by which molecules can be transported in a relatively predictable manner through the microchannels.

In microfluidics, the hydraulic resistance, R_{yhd}, depends on the cross-sectional shape of the straight channel. Typically, if a rectangular cross section in microfluidics is assumed, R_{yhd} is given by Equation 2.2:

$$R_{hyd} = \frac{12\eta L}{1 - 0.63\left({}^{h}/_{\omega}\right)} \frac{1}{h^3 \omega} \tag{2.2}$$

where η = 1 mPa s (water), L is the length of the channel, h is the height of the channel, and ω is the width of the channel. Hydraulic resistance is a key concept when characterising and designing microfluidic channels dimensions in LOC devices[37].

Centrifugal microfluidics or lab-on-a-disc (LoaD) platforms (see Chapter 5) exploit the centrifugal force to manipulate liquids in microfluidics. Centrifugal microfluidics offer many intrinsic advantages compared with pump-driven systems. Rotational actuation is simply implemented by controlling the frequency of a spindle motor to rotate the disc. As the spinning frequency can easily be controlled over more than three orders of magnitude, the range of forces covers approximately six orders of magnitude, which is far superior to common, pressure-driven lab-on-a-chip systems. The volumetric flow rate is dependent on the speed at which the disc spins, the geometry, dimensions and surface functionality of the fluidic channels, the distance the liquid is from the centre of the disc, and the properties of the fluid, such as density and viscosity. A wide range of flow rates can be achieved with high degree of accuracy and precision, simply by using combinations of different spin speeds and channel geometries. Another advantage of the centrifugal technology is the independence of the fluid movement from parameters such as conductivity and pH. Furthermore, due to the inertia of the disc, the spinning motion is self-stabilising, thus eliminating jittering from reciprocating or syringe pumps.

The fluid manipulation within centrifugal discs primarily relies on the three rotationally induced (pseudo) forces in the plane of rotation of the disc.

1. A particle or fluid volume density, ρ, on a planar substrate rotating at a distance, r, from a central axis experiences a radially directed centrifugal force density according to Equation 2.3:

$$f_{\mathrm{CE}} = \rho r \omega^2 \tag{2.3}$$

which scales with the square of the rotational frequency, ω.

2. Secondary effects, which are induced by the spinning frame of reference, are the Euler force density, represented by Equation 2.4:

$$f_{\mathrm{Euler}}\, \rho \, \frac{d\omega}{dt} \tag{2.4}$$

which is directed against a change in fluid velocity and results in swirling currents propelled by rotational acceleration.

3. Finally, the Coriolis force density, represented by Equation 2.5:

$$f_{\mathrm{Coriolis}} = 2\rho\omega v \tag{2.5}$$

which deflects objects perpendicular to their direction of motion at the velocity, v, in the plane of rotation (see Figure 2.2).

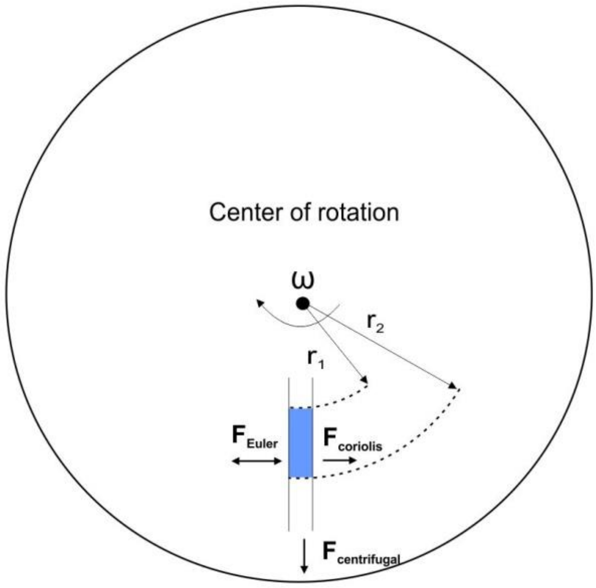

Figure 2.2: Forces acting in centrifugal microfluidics.

2.3 Integration of Functional Materials into Microfluidic Devices

Stimuli-responsive materials, known as “smart materials” have gained increasingly high attention due to their autonomous behavior in response to changes in their local environment. Smart polymers are characterised by their stimuli-responsive behavior, which is essentially dictated by the functional groups present within their polymer chains. Smart materials are able to perform functions by external stimuli (magnetic or electric field, temperature, light, pH, chemical or solvent composition), without human manipulation. In this Section, the different stimuli-responsive materials used in this thesis will be introduced and linked to their type of actuation/sensing capabilities. These capabilities will be later demonstrated and implemented in the devices studied in each of the following Chapters.

In general, this work will try to evidence that in order to minimise the complexity of integrated microfluidic devices for environmental applications, all electronically controllable components (*e.g.* valves, pumps and sensors) could be made with smart materials and so, reduce the complexity and the final dimensions of the system, improving portability, while at the same time, minimise costs on electronic components.

2.3.1 Hydrogels as Thermoactuators

Thermoresponsive hydrogel materials are a kind of smart materials that respond to an external temperature source by uptaking (swelling) or releasing (shrinking) a large quantity of water, leading to an abrupt change in their structural volume.

2.3.1.1 poly(*N*-isopropylacrylamide) (pNIPAAm) Hydrogels

pNIPAAm hydrogel is one of the best temperature-sensitive multifunctional hydrogels used in microfluidic applications. At a temperature above the lower critical solution temperature (LCST), 32 °C, pNIPAAm chains undergo a rapid and reversible entropy driven phase transition from extended hydrated coils to collapsed hydrophobic globules that precipitate in water, reducing the volume of the hydrogel. This behaviour opens the possibility to use pNIPAAm as actuators in microfluidic device applications. PNIPAAm hydrogels are typically controlled by electronic heating elements[38, 39], magnetic fields[40, 41] or light[42-44]. An illustrative example of this methodology is the work published by Liang *et al.*[45] where, for the first time, pNIPAAm was proposed as an actuator in a microfluidic device. A few years later, Kuckling *et al.*[46] and later on, Harmon *et al.*[47] presented pNIPAAm hydrogels integrated as actuators in microfluidic devices for flow control, as in the example presented in Figure 2.3. This hydrogel will be the base material for the synthesis of the smart material presented in Chapter 5.

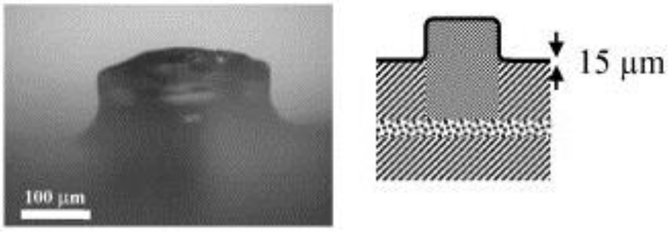

Figure 2.3: Picture of a pNIPAAm hydrogel in the microfluidic device. The hydrogel is flowing inside the microchannel[47].

Other types of polymeric materials have been also employed as thermo-actuator components in microfluidic devices such as pNIPAAm derivatives[48] and poly[ethylene-*co*-(vinyl acetate)] (cPEVA)[49]. This thesis will investigate the thermo-responsiveness of materials such as alginate hydrogels, which are a network of sodium alginate chains typically polimerised with Ca^{2+} ions. This biomaterial has been widely explored for drug delivery and medical or surgery purposes[50]. Alginate hydrogels could be used as biocompatible alternative actuators in microfluidic devices, as demonstrated in Chapter 4.

Despite the huge potential of hydrogels in microfluidic device applications, their practical applicability is limited due to the discrete shrinking with increasing temperature, low material robustness, rather slow expansion kinetics and degree of actuation. All these drawbacks lead to look for alternatives such as ionogels and poly(ionic liquid) hydrogels.

2.3.1.2 Poly(ionic liquid) hydrogels

Chapter 6 will investigate the thermo-responsiveness of poly(ionic liquid) hydrogel materials (PILs) as an example of actuators in microfluidic devices. PILs are polymers formed through the polymerisation of ionic liquid monomers, which feature a polymerisable group in the anion, the cation or both (see the scheme of Figure 2.4[51]). The research focus is generally exerted on linear PILs. Nevertheless, there are several reports dealing with crosslinked PIL networks that are explored either as ion conductors[52-54], templates for multilamellar structured nanoparticles[55-57] or, more importantly, as actuators[58, 59]. PILs can be categorised basically on two criteria:

- which ion possesses the polymerisable group, cationic and anionic PILs.

- the presence or absence of a crosslinking agent used during the polymerisation phase of the PILs, which leads to either crosslinked or linear PILs.

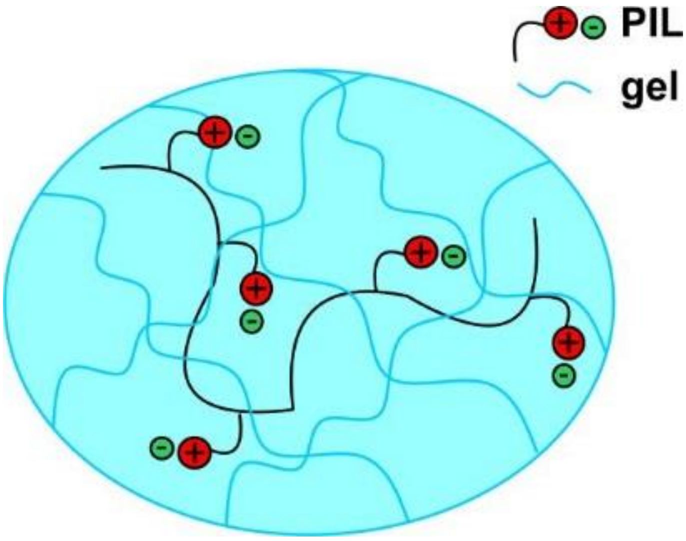

Figure 2.4: Schematic representation of a PIL hydrogel.

Crosslinked PILs have been applied as membranes[60], electrolytes[61], sensors[62], and actuators[63, 64], among others. Ziółkowski *et al.*[65] synthesised for the first time a PIL that featured a phosphonium ionic liquid monomer (ILM) with an LCST at 60 °C. The study focused on the synthesis of PILs based on the tetrabutylphosphonium styrenesulfonate and the tributylhexyl sulfopropylacrylate ($P_{4,4,4,6}$ SPA) ILMs. The resulting crosslinked polymers, using 5 mol % poly(ethylenglycol) diacrylate PEG700 or PPO800, swelled in deionised water, forming stable and transparent PIL hydrogels, which presented potential applications as actuators in microfluidic devices. Later, Gallagher *et al.*[66] investigated further the thermo-response capabilities of these PIL hydrogels by adding a linear pNiPAAm polymer in the PIL matrix, thus creating a semi-interpenetrating network. Results indicated that the hydrogels containing an amount of 1.2 molar units of linear pNiPAAm compared to the amount of phosphonium sulfopropyl acrylate tended, in general, to shrink to a greater extent when heated to 70 °C. The addition of linear pNiPAAm to the PIL matrix also increased the hydrogel swelling capacity.

Interestingly, Zhao *et al.*[63] published in 2014 an interesting paper where PIL hydrogels were used as actuators with a fast actuation speed, large-shape deformation, and robust responsiveness. These actuators are easy-to-make by mixing a cationic PIL, poly(3-cyanomethyl-1-vinylimidazolium bis (triofuoromethanesulfonyl)imide), and a carboxylic acid and resisted even after hydrothermal processing (200 °C, 24 h) and pressure (100 MPa) treatments[63].

2.3.2 Ionogels as Sensors and Actuators (Thermo- and Photoactuation)

Chapters 5 and 9 will directly deal with the integration and performance of ionogel materials as actuators and sensors in microfluidic devices. An ionogel can be defined as a hydrogel that contains an ionic liquid in its polymer matrix. Ionic liquids (ILs) are salts that melt below 100 °C and are comprised entirely by cations and anions. ILs typically contain a large bulky asymmetric cation together with a small π-delocalised anion, which exhibits mere electrostatic interactions. By choosing the appropriate ion pair, the physicochemical properties of the IL such as viscosity, density, melting point and conductivity can be tuned to some degree to suit a particular need. A sub-class of ILs, known as room temperature ionic liquids (RTILs), with a melting point below *ca.* 25 °C, have attracted special interest. These ILs have many interesting properties such as elevated ionic and electronic conductivity, rather high thermal stability, negligible vapour pressure, and in some cases high salvation power. This last property enables ILs to dissolve substances, *eg.* monomers *N*-isopropylacrylamide and crosslinkers *N,N*-methylene-bis(acrylamide) (MBAAm) that are difficult to dissolve in conventional solvents (see Chapter 5). An excellent review by Bideu *et al.*[67] presented ionogels as hybrid materials in which the properties of the IL are combined with those of the components (organic[68], inorganic[69], or hybrid organic-inorganic[70]) that form part of the ionogel matrix. Therefore, an ionogel has properties arising from both the polymeric network stabilising the ionogel and the functionalities of the immobilised IL. Due to their low vapour pressure and their ability to plasticise the gel network, ionogels exhibit high resistance to cracking and drying, which renders them as attractive materials in soft actuators and so, in microfluidic device applications. Several applications have been already presented in the literature with regards to ionogels in microfluidics, such as valves or actuators (photo-, thermo-responsive)[39, 71, 72], electrolytes[73], biomolecule storage[74], and optodes for sensing[75, 76].

In particular, Benito-Lopez *et al.*[71, 72] published several papers where ionogels were used as valves/actuators and sensors inside microfluidic devices. They developed different valves with a photoswitchable molecule that, when irradiated with light, changes its configuration and shrinks allowing the fluid flow through the microchannels of the microfluidic device. When in the dark, the molecule reverts to its initial state, swelling and closing the microchannel[71, 72]. This photoresponsive valves and actuators will be discussed specifically and in detail in Section 2.3.3 due to its importance.

Thermo-responsive actuation (see Chapter 6) was also proposed for microvalves fabricated using pNiPAAm ionogels[39]. To synthesise these materials, all the components of the monomer mixture were dissolved in 1-ethyl-3-methyl imidazolium ethyl sulfate [EMIM][EtSO$_4$]. The addition of this IL, as demonstrated before by Gallagher *et al.*[77]*,* improves the swelling and shrinking capabilities of the pNIPAAm material, lowering the LCST. The ionogel valves were fully characterised and their performance demonstrated. Moreover, valves were found to resist pressures up to 1100 mbar (see Figure 2.5).

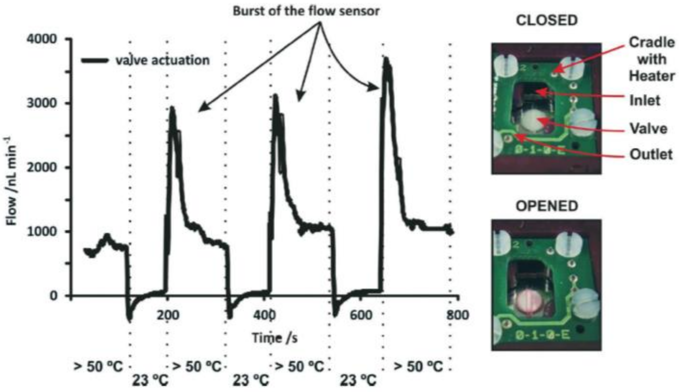

Figure 2.5: Flow profile during three full actuation cycles (left) and a photo of the device containing the thermo-actuated valve and the chip holder with integrated heaters at the bottom[39].

Electro-actuation of IL-based microvalves has also been studied. Ghamsari *et al.*[78] demonstrated the use of bucky ionogels based on the 1-ethyl-3-methyl imidazolium tetrafluoroborate ionic liquid ([EMIM][BF$_4$]), poly(vinylidene fluoride) (PVDF), and single-walled carbon nanotubes (SWCNT), respectively, as low-voltage microvalve actuators. Bucky gels are gel-like mixtures of carbon nanotubes and ILs, which benefit from both the high electrical conductivity associated with carbon nanotubes and the properties of ILs, such as high temperature and electrochemical stability. Applying voltage to this ionogel makes it bend in the direction of the applied voltage (Figure 2.6a and b). Three different ionogels were fitted to microfluidic devices to cover an inlet channel that was fabricated from a tube (Figure 2.6c and d). The results indicated that the higher the voltages and the lower the frequency, the better they are suited for use as microfluidic valves, in which the best results were obtained at 10 V and 0 mHz, at which the flow rate was reduced by 93 %.

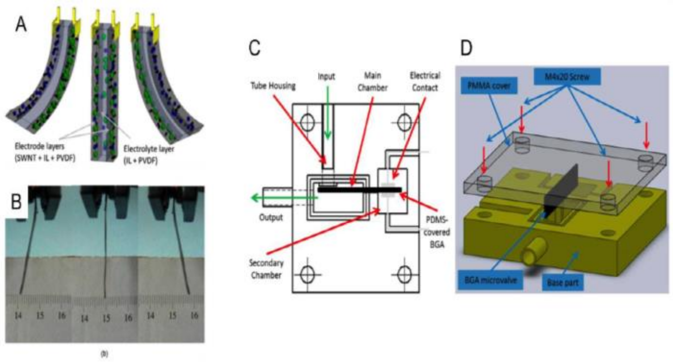

Figure 2.6: (a) BGA bending motion as a result of ion transfer between layers; the direction of bending can be reversed by changing the polarity of the applied potential; (b) BGA strip bent (10 V, 0.1 Hz). (c) Base part and (d) 3D view of the flow regulator assembly.

Ionogels have been employed within optodes, mainly as the plasticiser to produce the film. Zhou *et al.*[75] used phosphonium based ionogels with a formal chromoionophore for the detection of important inorganic acids such as HCl and H_2SO_4. In another approach, Kavanagh *et al.*[76] presented an ionogel/optode that changed colour in the presence of Cu^{2+} and Co^{2+} ions. The use of functional materials for sensing in microfluidic devices continues to gain traction, due to the ability of these materials to offer a matrix, which can respond to a chemical and/or a physical stimulus. The wide electrochemical windows, high conductivity, propensity to stabilise enzymes and liquid state at room temperature have carved a niche for these exciting new materials in the field of sensing chemical and physical changes[79]. Their ability to immobilise molecules to be used for pH analysis, catalysis and in electrochemistry have also brought additional applications of ionogels as biomolecular sensors.

The serendipitous growth of POC technologies, in particular through organic electronics, has buttressed the development of these compounds with a tangible need for efficient protein solubilisation in specific pH and temperature ranges. For instance, Khodagholy *et al.*[73] used the combination of an Organic Electrochemical Transistor (OECT) and an ionogel, which found applications in sensing biomolecules. These simple transistors operate through migration of ions from an electrolyte into a semiconductor, which is often fabricated from a doped polymer, such as poly(3,4-ethylenedioxythiophene) with poly(styrene sulfonate) (PEDOT : PSS). In this case, a flexible ionogel based on NIPAAm, MBAAm and [EMIM][$EtSO_4$] incorporating the lactate oxidase (LOx) enzyme was polymerised on the OECT device. The introduction of the specific analyte (in this case lactate), resulted in an increase in the drain current, which can be directly correlated to the lactate concentration, as seen in Figure 2.7a. Figure 2.7b shows a prototype fabricated from parylene worn on the forearm.[73] Such a flexible prototype, coupled with detection levels suitable for use in the clinical range, was proved to be extremely exciting in the fields of sports science and patient care.

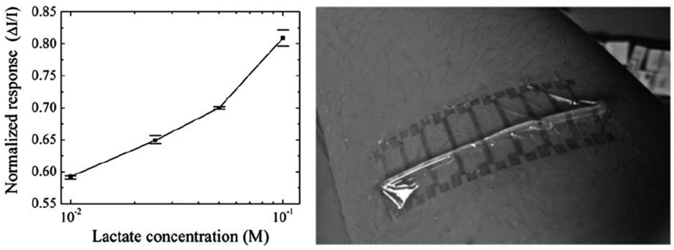

(a) (b)

Figure 2.7: (a) Normalised response *vs.* lactate concentration for the OECT and (b) Flexible OECT on the forearm[73].

A true understanding of the effect that ILs have on enzymes was recently developed by Curto *et al.*,[80], in particular for choline-based ILs containing the LOx enzyme. It was concluded that hydrated ILs can provide the necessary hydrogen bonding for the necessary stabilisation of proteins, in addition to controlling the proton buffering within the medium. Interestingly, when stored in choline chloride, over a 140 day period at 5 °C, an 80 % of the initial activity of LOx was retained. Following this concept, ionogels could be used for the immobilisation of enzymes or other sensing molecules such as dyes. Through ion-pair interactions, a charged dye molecule was held in the ionogel matrix without leaching. Czugala *et al.*[81] developed a direct application of such a system, using a centrifugal disc with functionalised ionogel sensing areas. The ionogel, based on pNIPAAm and MBAAm and the ionic liquid tetrabutylphosphonium dicyanamide $[P_{4,4,4,4}][DCA]$ were used to entrap the molecule, bromocresol purple. Photopolymerisation yielded to an ionogel, which responds to the variation of pH in the range 4 - 10 (see Figure 2.8).

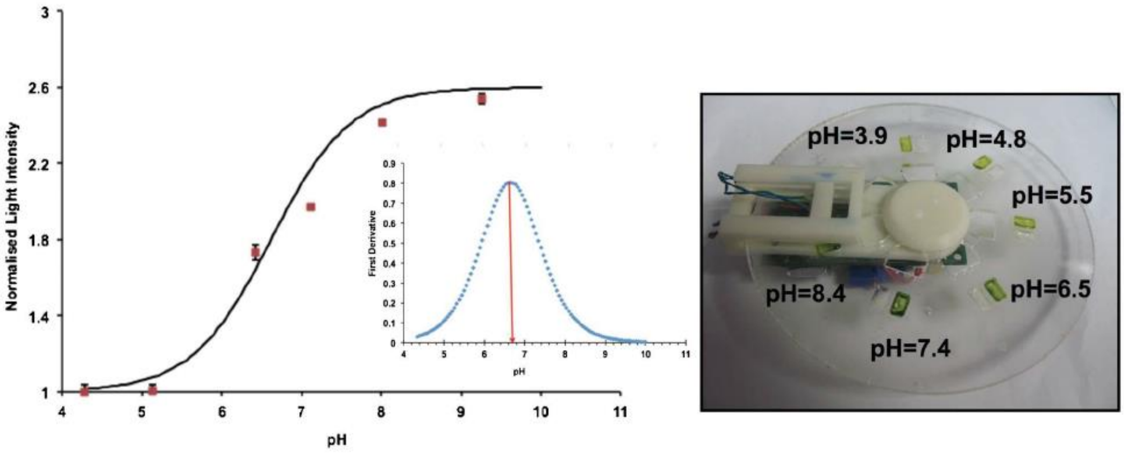

Figure 2.8: (a) Calibration curve of the sensing area of the microfluidic device using pH buffer solutions. (b) Image of the disc platform with the sensing area[81].

In a similar fashion, Curto *et al.*[82, 83] extended the use of ionogels with encapsulated pH-responsive dyes to fabricate a simple barcode device capable of measuring sweat pH in real time, using colorimetric imaging through a mobile phone application (Figure 2.9). By applying an algorithm which mapped to the HUE saturation value colour space it was possible to use a mobile phone application to generate calibration curves with R^2 value greater than 0.995.

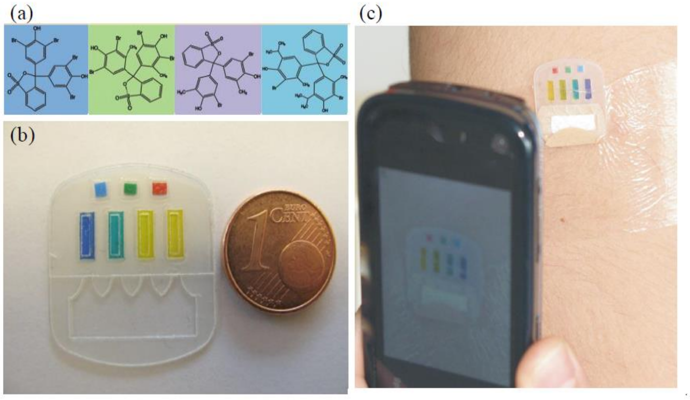

Figure 2.9: (a) Chemical structures of the pH-sensitive dyes: Bromophenol Blue, Bromocresol Green, Bromocresol Purple and Bromothymol Blue; (b) Fabricated microfluidic device. (c) Smartphone application imaging on-body device[82, 83].

Due to their versatility, promising solvation properties and interactions with solute species, ionic liquids have been long proposed as alternative solvents[84, 85]. Building upon this and adding their high thermal stability, negligible vapour pressure and enzymatic stability, ionic liquids[86] and ionogels have been recently proposed as storage media in microfluidic devices. Tijero *et al.*[74]

demonstrated that an ionogel could be used as reagent storage unit in microfluidic devices. They released biotin molecules after being stored for one month at room temperature inside an ionogel array in a microfluidic device. This was possible by using the thermos-actuation capabilities of the ionogel. Using an ink-jet printing approach, UV-cured ionogel-based microarrays were fabricated and used for long-term storage of biotin-647 molecules in a microfluidic device, Figure 2.10.

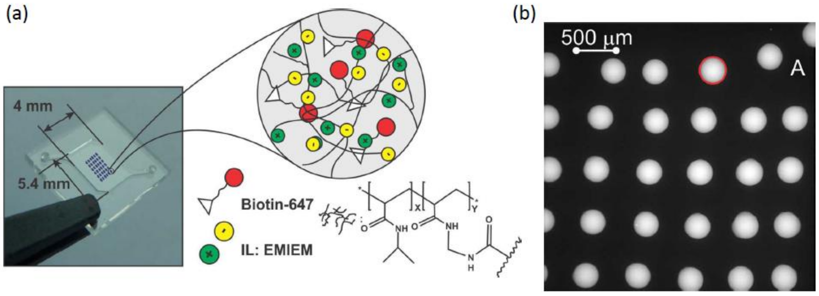

Figure 2.10: (a) Inkjet printed ionogel microarray in the microfluidic device and representation of the composition of the ionogel spots. (b) Fluorescence images of biotin-647 inside an ionogel-based microarray[74].

2.3.3 Hydrogels and Ionogels as Photoactuators

Chapter 5 describes for the first time the use of a photoresponsive actuator into Lab-on-a-Disc device. Therefore, this section deals with these types of materials and their integration in microfluidic devices.

Switchable materials offer intriguing possibilities and the potential to integrate sophisticated functions in a microfluidic device. Because of their relative ease of fabrication and simple control, stimuli-responsive materials integrated into microfluidic devices could significantly advance the development of fully integrated microfluidic systems[87, 88].

One of the most attractive strategies to implement fluid manipulation on integrated microfluidic platforms is light irradiation, which allows not only for non-contact operation but also independent and remote manipulation of multiple fluids. Photoresponsive polymeric materials have been studied by many research groups, and many polymers and polymer hydrogels functionalised with azobenzene, leukochromophore, and spirobenzopyran have been examined[89].

One of the first reports of a spiropyran monomer copolymerised with vinyl monomers to obtain a photoresponsive polymer hydrogel was published by Smets *et al.*[90] in 1978. In this publication, a crosslinker consisting in two connected spiropyran molecules, each with a vinyl group attached, was synthesised. In 2007, Sugiura *et al.*[91] proposed photoresponsive microfluidic hydrogel valves by copolymerising NiIPAAm with a photochromic acrylic benzospiropyran ester (BSP) moiety. Prior to photopolymerisation, the cocktail mixture of the monomer and the photochromic unit was dissolved in 1-butanol, together with a UV initiator and the crosslinker. The photoresponse mechanism of these hydrogels comes as a result of the benzospiropyran moiety present in the copolymer matrix. When the copolymer has been kept in the dark and exposed to an aqueous solution of HCl, the benzospiropyran moiety protonates, changing its conformation to the protonated merocyanine form. When in this conformation, the presence of charges on its backbone contributes to it being more hydrophilic than the closed benzospiropyran conformation, thus absorbing more water. By irradiating the hydrogel with white light, the process can be reversed to the more hydrophobic benzospiropyran form, together with the release of water. Authors showed that valves obtained from this material can perform, if preconditioned overnight in acidic conditions, to open and stop the flow inside a PDMS microfluidic device.

Building on this work, Benito-Lopez *et al.*[72] synthesised photoresponsive ionogel valves in microfluidic channels by copolymerising NiPAAm and BSP using a mixture of 1-butanol and phosphonium ionic liquids as the solvent. Four different ILs were used, namely triisobutyl(methyl) phosphonium tosylate ($[P_{1,4,4,4}][Tos]$), trihexyltetradecyl phosphonium dicyanamide ($[P_{6,6,6,14}][DCA]$), trihexyltetradecyl phosphonium bis(trifluoromethanesulfonyl) imide ($[P_{6,6,6,14}][Ntf_2]$), and trihexyltetradecyl phosphonium dodecylbenzenesulfonate ($[P_{6,6,6,14}][DBSA]$), respectively. Their swelling and shrinking behaviour as valves integrated into a microfluidic device were characterised. This example demonstrated that, through the incorporation of different ionic liquids of varying hydrophilic/hydrophobic character inside ionogel matrices, valve actuation times can be modulated on demand in the microfluidic device (Figure 2.11).

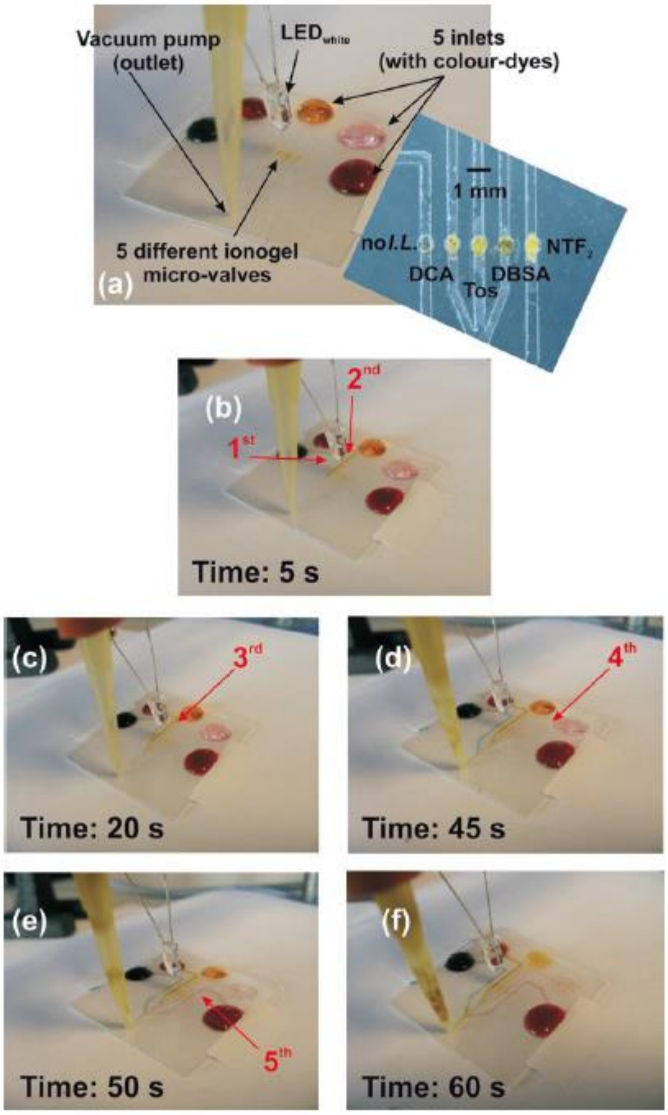

Figure 2.11: Image of the microfluidic manifold showing the performance of the ionogel valves: (a) valves closed under the applied vacuum. White light is applied for the time specified in each picture. (b) Hydrogel (no IL present) valve is first to actuate followed by ionogels incorporating [DCA]$^-$ (c), [Tos]$^-$ (d), [DBSA]$^-$ (e), [NTf$_2$]$^-$ (f). Numbers and arrows indicate when the channel is filled with the dye due to microvalve actuation[72].

In a more comprehensive study, the photoresponsive ionogel materials were systematically studied by Czugala *et al.*[92, 93]. The behaviour as valves of the NIPAAM/BSP ionogels synthesised with phosphonium ILs (trihexyltetradecyl-phosphonium chloride [P$_{6,6,6,14}$][Cl], Trihexyltetradecyl-phosphonium dicyanoamide [P$_{6,6,6,14}$][DCA] and trihexyltetradecyl-phosphonium bis(trifluoromethanesulfonyl)-amide [P$_{6,6,6,14}$][Ntf$_2$]) was investigated and their swelling and shrinking behaviour was fully characterised (see Figure 2.12). Later, based on these results, the [P$_{6,6,6,14}$][Ntf$_2$] ionogel was incorporated in a glass-poly(dimethyl siloxane) microfluidic device as a light actuated valve. By using a fiber optic to irradiate the ionogel valve with white light, it opened after 180 s, allowing liquid to pass through the microfluidic channel.[93]

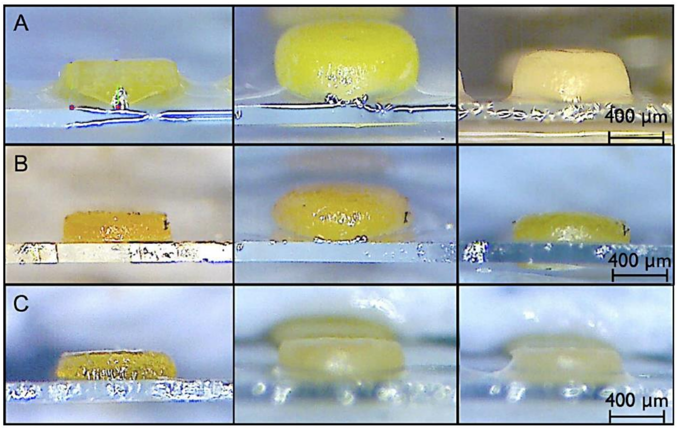

Figure 2.12: Microscope images of ionogel discs made of: (a) $[P_{6,6,6,14}][NTf_2]$. (b) $[P_{6,6,6,14}][DCA]$ and (c) $[P_{6,6,6,14}][Cl]$ after photopolymerisation (left); swelling in 1 mM HCl solution for 2 h (middle) and shrinking upon white light irradiation (right).

An application of these materials was demonstrated by Czugala *et al.*[71] by using the $[P_{6,6,6,14}][DCA]$ ionogel as a photoresponsive valve in a microfluidic analytical platform for the detection of nitrite anions in water. The nitrite assay was done using the Griess reagent and the change in colour was determined using a Paired Emitter Detector Diode (PEDD) integrated into the microfluidic holder (see Figure 2.13). Freshwater samples from the Tolka River in Dublin, Ireland, were analysed with the portable platform.

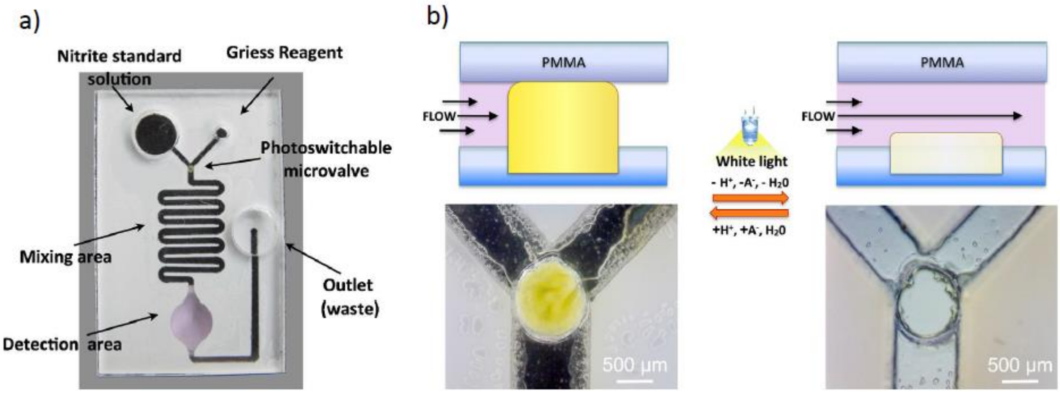

Figure 2.13: (a) Picture of the microfluidic device fabricated in PMMA: PSA polymer by CO_2 laser ablation. (b) Schematic (top) and images (bottom) of the photoresponsive microvalve in closed and opened state.

2.3.4 Membranes and colloids in Microfluidic Devices

Membranes are popular due to the low cost of their manufacture. Common membrane separation processes include gas separation, pervaporation, dialysis, electrolysis, reverse osmosis and micro-, ultra- and nano-filtration. Sample separation is achieved because a pressure head, electric field or a concentration gradient is applied through the permeable membranes. The required membrane properties for separation depend on particle size (distribution) and/or the separation mechanism. Based on their structure, the most common types of membranes are thin-film composite membranes[94, 95] and porous membranes[96].

Many different approaches have been described to combine membrane and microfluidics:

- Incorporation of commercial membranes[97, 98].

- Novel membrane preparation and integration[99-101].

- *In-situ* generation of membranes[102, 103].

These integrated membranes have been applied in different fields such as ions[97, 98, 104] or molecules transportation[104, 105], separation[106-108], and sensing[109-111]. These applications have been reviewed elsewhere[112, 113], therefore they will not be deeply presented in this Chapter. Specifically, membranes have been widely investigated as gas sensors. For instance, PDMS, due to its high permeability for gases and vapours, is often applied as material to sense oxygen[114],CO_2[115], H_2S, and SO_2[116], among others.

On the other hand, colloids are a mixture of dispersed insoluble particles suspended in a solvent. Colloids have been fabricated within microfluidics[117, 118] and have been integrated into microfluidics for several applications[119, 120].

Perfluorinated polymers have been used for the fabrication of both, membranes and colloids. The principle of these materials is that the scattered light increases significantly when sub-nanometer layers of molecules are formed on their surfaces. This approach enables the development of extremely simple, though highly sensitive, label-free biosensing devices. The integration of perfluorinated polymers as membranes and colloids, with a refractive index similar to that of water, in microfluidic devices for sensing applications will be presented in Chapters 7 and 8.

2.4 Microfluidic Devices for Water Monitoring

Microfluidic devices provide a way to perform analysis in remote locations, enabling *in-situ* analysis at the point of need[121]. Reduced measurement times, improvement in sensitivity, enhance of selectivity and high repeatability are advantages of microfluidic devices when integrated into µTAS[122]. However, despite the huge efforts of researchers in providing fully integrated, portable and feasible platforms for environmental sensing, µTAS are not yet commercially available. In a recent editorial in *Lab on a Chip,* George Whitesides referred to this issue, stating that *"LOC technology is now shifting from fundamental areas to serious explorations of uses and to demonstrations and applications with real potential to provide the incentive for further and more extensive industrial engineering development, and ultimately to incorporation into products"*[123]. Previously, in an Analytical Chemistry editorial Royce W. *Murray*[124] highlighted that *"to develop low cost analytical platforms for environmental monitoring is the fundamental challenge now facing the analytical chemistry community"*[124]. Therefore, during the last few years several microfluidic devices and platforms have been delivered for the monitoring of pollutants in a variety of water matrices: drinking water[110-118], waste and sewage waters[119-122], continental water (rivers, lakes, etc.)[80,123-132], and seawater[133-145] The state of the art of promising deployable microfluidic devices and field-deployable microfluidic systems for *in-situ* chemical analysis in different water matrices will be presented in this section. Using suitable examples, this section will describe general modes of operation; data that can be obtained; design factors that determine effectiveness; and challenges to wider adoption.

2.4.1 Drinking water

One of the biggest concerns in monitoring water quality is the assessment of the bacteria and other pathogens that could be harmful to humans through the consumption of drinking water. Since bacteria and pathogens are present in very low numbers in potable water, large volumes of water need to be concentrated to be appropriate for current detection methods. Multiple methods, including spectroscopy[125], cytometry[126] and electrophoresis[127] have been adopted in microfluidics. These integrated devices overcome the limitation arising from the extremely low number of bacteria to be analysed in the sample by increasing the concentration of the target bacteria via electrical techniques and, for instance, combine dielectrophoresis (DEP) and impedance measurements for detection[128]. Recently, high sample throughput and low bacterial number detection biosensors have been developed for potable water samples by concentrating the sample to smaller volumes prior to measurement[129]. A good example is the *E. coli* microfluidic detector reported by Kim *et al*.[130] for drinking water quality monitoring. To decrease the detection limit and achieve high-throughput, the proposed device increases the concentration of bacteria by DEP force-mediated *E. coli* focusing and senses the trapped *E. coli* by measuring dielectrophoretic impedance. An interesting approach for environmental monitoring was presented by Curtis *et al.*[131] based on a portable cell-based impedance sensor for toxicity testing of drinking water. It is known that a major limitation of using mammalian cell-based biosensor for field testing is the difficulty of maintaining cell viability and sterility outside a cell culture facility. To solve this problem, a compact, self-contained disposable media delivery system was incorporated.

Other analytes of interest in drinking water that have been investigated in microfluidic devices are metals such as copper[132-134], lead[135], water safety indicators such as nitrite and nitrate[136], total concentration of calcium and magnesium[137] and chlorine[138]. For instance, the presence of copper in drinking water usually does not exceed from more than few milligrams per liter, although higher concentrations could be detected in water delivered through newly installed copper pipes. Copper is an important element for the metabolism of living species, but as with many other metals, at high concentrations is toxic. Zhao *et al*.[133] developed a microfluidic analyser of heavy metal ions such as copper in drinking water samples that were taken from Tønsberg´s pipes in Norway. Bioluminescence was used for detection and it was carried out following the inhibition of light emission of *V. fischeri* in response to copper toxicant effect.

2.4.2 Wastewater

Waste and sewage waters are generated by a variety of sources and the concentration and type of contaminants found in them vary in each water source. Thus, the detection methodology employed for analysis should be adaptable to comply with regulations and quality standards.

For example, aromatic amines, which have been demonstrated to be carcinogenic and mutagenic at very low concentrations, can be released into the environment from industry along with waste. Li *et al.*[139] established a simple, rapid and sensitive method for the separation and determination of five aromatic amines by a microfluidic electrophoresis device with a low-cost laser-induced fluorescence detector using an easy-to-make and disposable COC microfluidic device.

Other contaminants of interest are metals, such as copper. In this regard, a hybrid glass/PDMS microfluidic device coupled to the anoptical sensor was applied for the determination of Cu (II) in industrial wastewater[140].

Del Mar Baeza *et al.*[141] described a micro-flow-injection analysis (µFIA) structure micromachined in silicon and sealed with anodically bonded pyrex glass. The µFIA was used for nitrite determination, using the Griess-Ilosvay reaction, online in a wastewater treatment plant. The optical measurements were performed using an LED as emitter and a photodiode as a detector. Later on, Calvo-López *et al*.[142] developed and tested a low temperature co-fired ceramics based continuous flow potentiometric microanalyzer to simultaneously monitor the presence of potassium and nitrate in samples from a water recycling process in space missions. The microsystem integrates microfluidics and the detection system in a single substrate and it is smaller than a credit card. The detection system is based on two ion-selective electrodes, built with nitrate and potassium polymeric membranes and a screen-printed Ag/AgCl reference electrode.

2.4.3 Continental water

Continental water bodies are flowing waters, lakes, reservoirs, and groundwater. When rain falls into the groundwater keeps moving along the land surfaces to streams or lakes. Some of it evaporates into the atmosphere and some soak into aquifers from which the public drinking water is usually obtained. Unfortunately, the groundwater can be contaminated by chemicals or pollutants and, consequently, the deposits of public water and hence the monitoring of these waters is of great importance. Nitrite and nitrate were determined by a low-cost µFIA with an integrated microfluidic device containing a cadmium microcolumn. Deep UV photolithography was used to create the urethane-acrylate resin microfluidic device where cadmium granules were manually packed before the device was sealed. The device was validated with freshwater samples (collected in three different areas of Paranóa lake (Brasília-DF, Brazil)[143]. Fluorimetric determination of sulfite and nitrite using *N*-(9-acridinyl)maleimide and 2,3-diaminonaphthalene as fluorescence reagents was performed in a PDMS microfluidic device. Rainwater, pond water, and river water samples were collected from the Sansiro Pond and the Arakawa River in Tokyo[144].

Organophosphate nerve agents such as paraoxon and methyl parathion spiked in river samples (Rio Grande, Las Cruces, NM) were separated and detected by coupling a micromachined capillary electrophoresis device with a thick-film amperometric detector. The glass microfluidic device consisted of two crossed channels and three reservoirs, including a four-way injection cross (connected to the reservoirs) and a 72 mm separation channel. The integrated system offered rapid simultaneous measurements of micromolar levels of both poisons[145]. Jayawardane *et al*.[146] prepared and evaluated a paper-based device for the determination of reactive phosphate in natural and soil waters based on the formation of phosphomolybdenum blue. The described device is low cost, fast and portable, and in a green chemistry perspective, the device uses less reagent than conventional laboratory methods.

Martinez *et al*.[147] developed and characterised a microfluidic inmunosensor device coupled with a FIA system that was used for the rapid and sensitive quantification of ethinylestradiol in river water samples taken from six rivers of San Luis State, Argentina.

Yakovleva *et al*.[148] developed a microfluidic immunosensor based on the affinity of proteins coated on the surface within hydrophilic polymers such as polyethylenimine, dextran, polyvinyl alcohol and aminodextran and cathodoluminescence detection. The device was applied for atrazine determination in surface water samples, from Höje Å river in Sweden.

Czugala *et al.*[81] described a wireless paired emitter detector diode device as an optical sensor for water quality monitoring in a lab-on-a-disc device. The microfluidic platform, based on an ionogel sensing area, is applied for quantitative pH and qualitative turbidity monitoring of water samples at the point-of-need. Local freshwater samples form Tolka River (Ireland) and brackish sources were analysed using the device, obtaining a very good correlation with standard bench-top systems.

A microfluidic device integrated with a fluorescence detection system was developed for the on-line determination of ammonium in aqueous samples. A light-emitting diode as an excitation source was mounted into a PDMS based microfluidic device. Ammonium was determined by its reaction with *o*-phthaldialdehyde on-chip with sodium sulfite as reducing reagent to produce a fluorescent isoindole derivative. The system was applied to determine the ammonium concentration in rain and river waters from the surface of a polluted lake[149].

Hydrogen peroxide present in rainwater is an efficient oxidiser of sulphur dioxide to produce sulfuric acid, an important compound in acid rain formation. Marle *et al.*[150] used the luminal chemiluminescence reaction within a glass microfluidic device for the determination of hydrogen peroxide in rainwater and snow collected from the roof of the chemistry building at the University of Hull, United Kingdom, as a proof of principle of this type of technology.

Nuriman *et al.*[151] presented a low-cost alternative to atomic absorption spectrometry for the colorimetric determination of Hg^{2+} ions based on an optical fiber chemical sensor in a microfluidic device containing a selective tripodal chromoionophore-PVC film with a detection limit of 0.5 µM. The microfluidic device was evaluated with water samples from the Bedadung river in Jember, Indonesia, obtaining good reproducibility and fast responses. Wang *et al.*[152] also determined Hg^{2+} ions in a microfluidic device coupled with a near-infrared fluorescence detector based on Hg^{2+}-induced aggregation of label-free ssDNA wrapped SWNTs. The microfluidic device was fabricated with PDMS and water samples were taken from a nearby river at Fudan University, China[152].

Jung *et al.*[153] presented a microfluidic device with a reusable sensor for heavy metal monitoring, in particular, for the detection of Pb^{2+}. The chip consists of a sensor, which integrates silver counter and quasi-reference electrodes. The device was applied for the measurement of soil pore water and groundwater.

2.4.4 Seawater

The quality of seawater depends in a great stand on the equilibrium in the concentration of compound as nitrite, nitrate, ammonium, and phosphate, which are denominated as nutrients. In addition, chemical parameters such as pH, temperature, and conductivity, among others are of importance for preserving water quality.

Several implementations of microfluidics for seawater environmental monitoring have been reported to date. Diamond's group published a microfluidic device sensor for long-term monitoring of phosphate that incorporates fluid sampling, reagent storage, detection and wireless communication into a portable platform[154-156]. Recently, the same group presented a portable sensor platform for *in-situ* pH measurements within aqueous environments containing reagents storage. The reagents were stable for over 8 months showing good reproducibility[157]. In addition, Zou *et al.*[158] presented an on-site water analyser capable of automatically performing long-term continuous sampling for heavy metals measurement using a continuous flow sensing method with an array of disposable polymer chips[158].

Hwang *et al.*[159] developed a centrifugal microfluidic device for simultaneous determination of nitrate, nitrite, ammonium, orthophosphate, and silicate in coastal seawater samples collected from Chunsu Bay, Korea. The device integrated all processes (sample filtering, metering, mixing, reaction, colorimetric detection) and liquid flow was controlled by laser irradiation on ferro-wax based microvalves.

Legiret *et al.*[160] reported an autonomous analytical system based on the vadomolybdate method for the determination of phosphorous in seawater. This method is based on the rapid reaction of orthophosphate with an acidified vanadomolybdate reagent, which produces a yellow colored complex. The system combined a PMMA microfluidic device, a custom syringe pump, embedded control electronics and onboard calibration standards. As a field evaluation, the microfluidic analyser was tested off the south-west coast of England near Plymouth, UK, onboard the RV *Plymouth Quest*.

Rerolle *et al.*[161] reported a low cost microfluidic colorimetric pH sensor device with a robust optical set-up achieved with the use of a custom-made polymeric flow cell coupled to a three wavelengths Light Emitting Diode detector. The system demonstrated to be deployed with high accuracy and precision, during short-term sampling, in European shelf waters. Previously in 2011, Beaton *et al.*[162] described the development of an automated and compact nitrite sensor device very low power and with minimal reagent use. The Griess method was used for nitrite detection, as in the case of the device presented in Chapter 9. The microfluidic device integrates all fluidic processing and optical detection on a common platform, yielding a low cost, miniature, portable and sensitive environmental nitrite sensor device that has LOD of 15 nM. In a new version of the platform, reagent bags were suspended above the outside of the sensor housing so that they could be accessed and changed weekly without terminating the deployment[163].

Kim *et al.*[164] showed an integrated microfluidic sensor module for measuring temperature, conductivity, and salinity during the seawater reverse osmosis process. The module was applied to product water harvested from a pilot-scale desalination plant over a five-day period. In 2016, Perez de Vargas San Salvador *et al.*[165] developed a portable sensor for *in-situ* measurement of pH (4-9) within aqueous environments by the combination of several pH sensitive dyes. Many real samples of different matrices such as effluent, drinking water, and surface water were tested. The results were compared to the ones provided by a reference method showing acceptable reproducibility (< 3.85 %).

Recently, Cao *et al*.[166] presented a sensor device that is able to measure continuously silicate in seawater samples. The reaction mechanism of the sensor is based on the reaction of silicate with ammonium molybdate to form a yellow complex and its further reduction to silicomolybdenum blue by ascorbic acid. The device has several advantages such as high accuracy, high integration, low water consumption, and strong anti-interference ability. It has been successfully applied to measure silicate in seawaters at Jiaozhou Bay, China.

2.5 Conclusions

Microfluidic devices have been gaining attraction as reflected in both, the growing number and the improved quality of articles published on this topic. Microfluidics have appeared as an alternative to conventional systems, which are not adequate for on-site use, mainly due to the difficulties of transportation and connectivity. Even though significant progress is continuously appearing in microfluidics, fluid manipulation and sensing are major problems to overtake in order to implement these types of devices in remote locations.

Following these premises, the European FP7 funded project (NAPES: Next Generation Analytical Platforms for Environmental Sensing), which is the core of this thesis, claims that the future on environmental microfluidics will be achieved when “highly effective autonomous sensors will be able to measure and share information about the quality of our environment, and particularly water”. For this reason, smart materials that are capable of undergoing changes in their conformational structure by an external stimulus should be introduced as alternatives to conventional valves, reagents reservoirs and even sensors in microfluidic devices. Therefore, this thesis will tend to contribute to the integration of functional materials into environmental microfluidic devices for fluidic control and sensing.

2.6 References

1 T. Thorsen, S. J. Maerkl and S. R. Quake, *Science,* 2002, 298, 580-584.

2 G. M. Whitesides, *Nature,* 2006, 442, 368-373.

3 A. Van Den Berg and P. Bergveld, *Lab Chip,* 2006, 6, 1266-1273.

4 D. R. Reyes, D. Iossifidis, P. Auroux and A. Manz, *Anal. Chem.,* 2002, 74, 2623-2636.

5 P. S. Nunes, P. D. Ohlsson, O. Ordeig and J. P. Kutter, *Microfluid Nanofluid.,* 2010, 9, 145-161.

6 N. Keller, T. M. Nargang, M. Runck, F. Kotz, A. Striegel, K. Sachsenheimer, D. Klemm, K. Länge, M. Worgull, C. Richter, D. Helmer and B. E. Rapp, *Lab Chip,* 2016, 16, 1561-1564.

7 D. S. Kima and K. W. Oh, in *Lab on a chip Technolgy: fabrication and microfluidics,* ed. ed. K. E. Herold and A. Rasooly, Caister Academic Press, 2009, pp.139-161.

8 J. C. McDonald, D. C. Duffy, J. R. Anderson, D. T. Chiu, H. Wu, O. J. A. Schueller and G. M. Whitesides, *Electrophoresis,* 2000, 21, 27-40.

9 M. Armani, R. Probst and B. Shapiro, in *Lab on a chip Technolgy: fabrication and microfluidics,* ed. K. E. Herold and A. Rasooly, Caister Academic Press, 2009, pp.139-161.

10 Y. Chen, L. Zhang and G. Chen, *Electrophoresis,* 2008, 29, 1801-1814.

11 K. Liu and Z. H. Fan, *Analyst,* 2011, 136, 1288-1297.

12 T. Ghandoori, W. Gao, L. Kong and S. Dharmalingam, *Adv Sci Enginee Med,* 2014, 6, 50-55.

13 S. K. Sia and G. M. Whitesides, *Electrophoresis,* 2003, 24, 3563-3576.

14 H. Becker and C. Gärtner, *Analytical and Bioanal. Chem.,* 2008, 390, 89-111.

15 J. Rossier, F. Reymond and P. E. Michel, *Electrophoresis,* 2002, 23, 858-867.

16 T. Wang, J. Wu, T. Chen, F. Li, T. Zuo and S. Liu, *Microsys.Technol.,* 2017, 23, 1405-1409.

17 I. Banerjee, T. Salih, H. Ramachandraiah, J. Erlandsson, T. Pettersson, A. C. Araújo, M. Karlsson and A. Russom, *RSC Advs.,* 2017, 7, 35048-35054.

18 M. Shen, J. Lai, C. Hong and G. Wang, *Sens. Bio-Sens. Res.,* 2017, 13, 75-80.

19 A. Piruska, I. Nikcevic, S. H. Lee, C. Ahn, W. R. Heineman, P. A. Limbach and C. J. Seliskar, *Lab Chip,* 2005, 5, 1348-1354.

20 S. A. Aghvami, A. Opathalage, Z. K. Zhang, M. Ludwig, M. Heymann, M. Norton, N. Wilkins and S. Fraden, *Sens. Actuators B, Chem.,* 2017, 247, 940-949.

21 W. D. Niles and P. J. Coassin, *Ass. Drug Dev. Technol.,* 2008, 6, 577-590.

22 K. M. Weerakoon-Ratnayake, C. E. O'Neil, F. I. Uba and S. A. Soper, *Lab Chip,* 2017, 17, 362-381.

23 H. Becker and C. Gärtner, *Electrophoresis,* 2000, 21, 12-26.

24 H. Becker and U. Heim, *Sens. Actuators A, Phys.,* 2000, 83, 130-135.

25 D. Wu, J. Sun, Y. Liu, Z. Yang, H. Xu, X. Zheng and P. Gou, *Polym. Eng. Sci.,* 2017, 57, 268-274.

26 D. Royet, Y. Hériveaux, J. Marchalot, R. Scorretti, A. Dias, N. M. Dempsey, M. Bonfim, P. Simonet and M. Frénéa-Robin, *J Magn Magn Mater,* 2017, 427, 306-313.

27 J. Cai, J. Jiang, F. Gao, G. Jia, J. Zhuang, G. Tang and Y. Fan, *Microsys. Technol.,* 2017, , 1-7.

28 L. Wang, R. Kodzius, X. Yi, S. Li, Y. S. Hui and W. Wen, *Sens. Actuators B, Chem.,* 2012, 168, 214-222.

29 D. Qin, Y. Xia and G. M. Whitesides, *Nat. Protoc.,* 2010, 5, 491-502.

30 D. Bartholomeusz A., R. Boutté W. and J. Andrade D., *IEEE/ASME J. Microelectromech. Sys.,* 2005, 14, 1364-1374.

31 M. Islam, R. Natu and R. Martinez-Duarte, *Microfluid.Nanofluid.,* 2015, 19, 973-985.

32 N. Bhattacharjee, A. Urrios, S. Kang and A. Folch, *Lab Chip,* 2016, 16, 1720-1742.

33 S. Waheed, J. M. Cabot, N. P. Macdonald, T. Lewis, R. M. Guijt, B. Paull and M. C. Breadmore, *Lab Chip,* 2016, 16, 1993-2013.

35 M. Boyd-Moss, S. Baratchi, M. Di Venere and K. Khoshmanesh, *Lab Chip,* 2016, 16, 3177-3192.

36 S. Prakash, M. Pinti and B. Bhushan, *Philos. Trans. R. Soc. A Math. Phys. Eng. Sci.,* 2012, 370, 2269-2303.

37 H. Bruus, *Theoretical microfluidics*, Oxford Press, Oxford, 2009.

38 A. Li, A. Khosla, C. Drewbrook and B. L. Gray, *Proceedings of SPIE - The International Society for Optical Engineering,* 2011, 7929.

39 F. Benito-Lopez, M. Antoñana-Díez, V. F. Curto, D. Diamond and V. Castro-López, *Lab Chip,* 2014, 14, 3530-3538.

40 M. Rahman, Y. Nahar, W. Ullah, A. Elaissari and H. Ahmad, *J. Polym. Res.,* 2015, 22.

41 X. Lin, R. Huang and M. Ulbricht, *J. Mater. Chem. B,* 2016, 4, 867-879.

42 N. Sharma, H. Keshmiri, X. Zhou, T. I. Wong, C. Petri, U. Jonas, B. Liedberg and J. Dostalek, *J. Phys. Chem. C,* 2016, 120, 561-568.
43 W. Jeong, S. Kim and S. Yang, *ACS Appl. Mater. Interfaces,* 2014, 6, 826-832.
44 L. Breuer, M. Raue, M. Kirschbaum, T. Mang, M. J. Schöning, R. Thoelen and T. Wagner, *Physica Status Solidi (A) Appl. Mater. Sci.,* 2015, 212, 1368-1374.
45 L. Liang, X. Feng, J. Liu, P. C. Rieke and G. E. Fryxell, *Macromol.,* 1998, 31, 7845-7850.
46 D. Kuckling, A. Richter and K. Arndt, *Macromol. Mater. Engin.,* 2003, 288, 144-151.
47 M. E. Harmon, M. Tang and C. W. Frank, *Polym.,* 2003, 44, 4547-4556.
48 A. Akimoto, T. Ueki and R. Yoshida, *Thermoresponsive polymers*, Springer, Berlin Heidelberg, 2014.
49 M. Behl, K. Kratz, U. Noechel, T. Sauter and A. Lendlein, *Proc. Natl. Acad. Sci. U. S. A.,* 2013, 110, 12555-12559.
50 A. D. Augst, H. J. Kong and D. J. Mooney, *Macromol. Biosci.,* 2006, 6, 623-633.
51 J. Yuan and M. Antonietti, *Polymer,* 2011, 52, 1469-1482.
52 P. Kallem, M. Drobek, A. Julbe, E. J. Vriezekolk, R. Mallada and M. P. Pina, *ACS Appl. Mater. Interfaces,* 2017, 9, 14844-14857.
53 A. T. Nasrabadi and L. D. Gelb, *J Phys Chem B,* 2017, 121, 1908-1921.
54 R. Pant, M. Kumar and A. Venkatnathan, *J. Phys. Chem. C,* 2017, 121, 7069-7080.
55 K. Manojkumar, D. Mecerreyes, D. Taton, Y. Gnanou and K. Vijayakrishna, *Polym. Chem.,* 2017, 8, 3497-3503.
56 L. Miao, H. Duan, M. Liu, W. Lu, D. Zhu, T. Chen, L. Li and L. Gan, *Chem. Eng. J.,* 2017, 317, 651-659.
57 W. Wu, J. Li, S. Zou, J. Guo and H. Zhou, *Front. Mater. Sci.,* 2017, 11, 42-50.
58 B. Ziólkowski and D. Diamond, *Chem. Commun.,* 2013, 49, 10308-10310.
59 S. Gallagher, L. Florea, K. J. Fraser and D. Diamond, *Int. J. Mol. Sci.,* 2014, 15, 5337-5349.
60 M. G. Cowan, D. L. Gin and R. D. Noble, *Acc. Chem. Res.,* 2016, 49, 724-732.
61 B. Yu, F. Zhou, C. Wang and W. Liu, *Eu. Polym. J.,* 2007, 43, 2699-2707.
62 C. Yuan, J. Guo and F. Yan, *Polym.,* 2014, 55, 3431-3435.
63 Q. Zhao, J. W. C. Dunlop, X. Qiu, F. Huang, Z. Zhang, J. Heyda, J. Dzubiella, M. Antonietti and J. Yuan, *Nat. Comm.,* 2014, 5.
64 Q. Zhao, J. Heyda, J. Dzubiella, K. Täuber, J. W. C. Dunlop and J. Yuan, *Adv. Mat.,* 2015, 27, 2913-2917.
65 B. Ziólkowski and D. Diamond, *Chem. Comm.,* 2013, 49, 10308-10310.
66 S. Gallagher, B. Ziolkowski, E. Fox, K. J. Fraser and D. Diamond, *Macromol. Chem. Phys.,* 2014, 215, 1889-1895.
67 J. Le Bideau, L. Viau and A. Vioux, *Chem. Soc. Rev.,* 2011, 40, 907-925.
68 N. Mohmeyer, D. Kuang, P. Wang, H. Schmidt, S. M. Zakeeruddin and M. Grätzel, *J. Materials Chem.,* 2006, 16, 2978-2983.
69 L. Viau, C. Tourné-Péteilh, J. Devoisselle and A. Vioux, *Chem. Comm.,* 2010, 46, 228-230.
70 F. Gayet, L. Viau, F. Leroux, F. Mabille, S. Monge, J. Robin and A. Vioux, *Chem. Mater.,* 2009, 21, 5575-5577.
71 M. Czugala, C. Fay, N. E. O'Connor, B. Corcoran, F. Benito-Lopez and D. Diamond, *Talanta,* 2013, 116, 997-1004.
72 F. Benito-Lopez, R. Byrne, A. M. Radut^a, N. E. Vrana, G. McGuinness and D. Diamond, *Lab Chip,* 2010, 10, 195-201.
73 D. Khodagholy, V. F. Curto, K. J. Fraser, M. Gurfinkel, R. Byrne, D. Diamond, G. G. Malliaras, F. Benito-Lopez and R. M. Owens, *J. Mater. Chem.,* 2012, 22, 4440-4443.
74 M. Tijero, R. Díez-Ahedo, F. Benito-Lopez, L. Basabe-Desmonts, V. Castro-López and A. Valero, *Biomicrofluid.,* 2015, 9.
75 J. Zhu, J. Zhai, X. Li and Y. Qin, *Sens. Actuators B, Chem.,* 2011, 159, 256-260.
76 A. Kavanagh, R. Byrne, D. Diamond and A. Radu, *Analyst,* 2011, 136, 348-353.
77 S. Gallagher, A. Kavanagh, B. Zíolkowski, L. Florea, D. R. Macfarlane, K. Fraser and D. Diamond, *Phys. Chem. Chem. Phys.,* 2014, 16, 3610-3616.
78 A. K. Ghamsari, E. Zegeye, Y. Jin and E. Woldesenbet, *ACS Appl. Mater. Interfaces,* 2013, 5, 5408-5412.
79 K. Behera, S. Pandey, A. Kadyan and S. Pandey, *Sensors (Switzerland),* 2015, 15, 30487-30503.
80 V. F. Curto, S. Scheuermann, R. M. Owens, V. Ranganathan, D. R. Macfarlane, F. Benito-Lopez and D. Diamond, *Phys. Chem. Chem. Phys.,* 2014, 16, 1841-1849.
81 M. Czugala, R. Gorkin III, T. Phelan, J. Gaughran, V. F. Curto, J. Ducrée, D. Diamond and F. Benito-Lopez, *Lab Chip,* 2012, 12, 5069-5078.

82 V. F. Curto, C. Fay, S. Coyle, R. Byrne, D. Diamond and F. Benito-Lopez, *15th International Conference on Miniaturized Systems for Chemistry and Life Sciences 2011, MicroTAS 2011,* 2011, 1, 577-579.
83 V. F. Curto, C. Fay, S. Coyle, R. Byrne, C. O'Toole, C. Barry, S. Hughes, N. Moyna, D. Diamond and F. Benito-Lopez, *Sens. Actuators B, Chem.,* 2012, 171-172, 1327-1334.
84 J. P. Hallett and T. Welton, *Chem. Rev.,* 2011, 111, 3508-3576.
85 W. L. Hough and R. D. Rogers, *Bull. Chem. Soc. Jpn.,* 2007, 80, 2262-2269.
86 S. Weidmann, S. Kemmerling, S. Mädler, H. Stahlberg, T. Braun and R. Zenobi, *Eu. J. M. Spec. (Chichester, England),* 2012, 18, 279-286.
87 M. O'Toole, R. Shepherd, G. G. Wallace and D. Diamond, *Anal. Chim. Acta,* 2009, 652, 308-314.
88 R. Byrne, C. Ventura, F. Benito Lopez, A. Walther, A. Heise and D. Diamond, *Biosens. Bioelectron.,* 2010, 26, 1392-1398.
89 L. Florea, D. Diamond and F. Benito-Lopez, in *in Opto-Nano-Mechanics: Material Systems, fundamentals, and applications" in Research Perspectives on Functional Micro-and Nanoscale Coatings,* ed. ed. A. Zuzuarregui and M. C. Morant, 2016, pp.265-288.
90 G. J. Smets, in *in Molecular models of photoresponsiveness,* ed. G. Montagnoli and B. F. Erlanger, Springer, Boston, 1978, 281-289.
91 S. Sugiura, K. Sumaru, K. Ohi, K. Hiroki, T. Takagi and T. Kanamori, *Sens. Actuators A, Phys.,* 2007, 140, 176-184.
92 M. Czugala, C. O'Connel, A. McKeon, C. F. Sanchez, X. Munoz-Berbel, A. Llobera, D. Diamond and F. Benito-Lopez, *2013 Transducers and Eurosensors XXVII: The 17th International Conference on Solid-State Sensors, Actuators and Microsystems, TRANSDUCERS and EUROSENSORS 2013,* 2013, 1695-1698.
93 M. Czugala, C. O'Connell, C. Blin, P. Fischer, K. J. Fraser, F. Benito-Lopez and D. Diamond, *Sens. Actuator B, Chem.,* 2014, 194, 105-113.
94 M. Asadollahi, D. Bastani and S. A. Musavi, *Desalination,* 2017, 420, 330-383.
95 N. Mehwish, A. Kausar and M. Siddiq, *Polym. - Plastics Technol. Engin.,* 2014, 53, 1290-1316.
96 D. M. Stevens, J. Y. Shu, M. Reichert and A. Roy, *Ind. Engin. Chem. Res.,* 2017, 56, 10526-10551.
97 M. Pham and D. P. J. Barz, *J. Membr. Sci.,* 2017, 537, 310-314.
98 A. Kusoglu, D. Kushner, D. K. Paul, K. Karan, M. A. Hickner and A. Z. Weber, *Adv. Funct. Mater.,* 2014, 24, 4763-4774.
99 J. De Jong, R. G. H. Lammertink and M. Wessling, *Lab Chip,* 2006, 6, 1125-1139.
100 X. Chen and J. Shen, *J. Chem. Technol. Biotechnol.,* 2017, 92, 271-282.
101 J. A. Hernández-Castro, K. Li, A. Meunier, D. Juncker and T. Veres, *Lab Chip,* 2017, 17, 1960-1969.
102 G. J. Sommer, J. Mai, A. K. Singh and A. V. Hatch, *Anal. Chem.,* 2011, 83, 3120-3125.
103 S. Dziomba, M. Araya-Farias, C. Smadja, M. Taverna, B. Carbonnier and N. T. Tran, *Anal. Chim. Acta,* 2017, 955, 1-26.
104 C. Park, D. R. Jacobson, D. T. Nguyen, S. Willardson and O. A. Saleh, *Rev. Sci. Instrum.,* 2016, 87.
105 B. Jin and A. S. Verkman, *Lab Chip,* 2017, 17, 887-895.
106 J. P. Dijkshoorn, M. A. I. Schutyser, R. M. Wagterveld, C. G. P. H. Schroën and R. M. Boom, *Sep. Purif. Technol.,* 2017, 173, 86-92.
107 K. Ikemoto, T. Seki, S. Kimura, Y. Nakaoka, S. Tsuchiya, F. Sassa, M. Yokokawa and H. Suzuki, *Anal. Chem.,* 2016, 88, 9427-9434.
108 C. Prechtl, M. Kraut, M. Franzreb, G. Brenner-Weiß and R. Dittmeyer, *Chem. Engin. Technol.,* 2017, 40, 670-677.
109 F. Li, P. Smejkal, N. P. Macdonald, R. M. Guijt and M. C. Breadmore, *Anal. Chem.,* 2017, 89, 4701-4707.
110 T. Ramon-Marquez, A. M. Sesay, P. Panjan, A. L. Medina-Castillo, A. Fernandez-Gutierrez and J. F. Fernandez-Sanchez, *Sens. Actuators B, Chem.,* 2017, 250, 156-161.
111 S. M. Grist, J. C. Schmok, A. D. Gaxiola and K. C. Cheung, *14th IEEE International NEWCAS Conference, NEWCAS 2016,* 2016, .114-116
112 P. Wang, D. L. DeVoe and C. S. Lee, *Electrophoresis,* 2001, 22, 3857-3867.
113 L. N. Moskvin and O. V. Rodinkov, *Russ. Chem. B.,* 2012, 61, 723-740.
114 A. P. Vollmer, R. F. Probstein, R. Gilbert and T. Thorsen, *Lab Chip,* 2005, 5, 1059-1066.
115 S. Herber, J. Borner, W. Olthuis, P. Bergveld and A. Van Den Berg, *Digest of Technical Papers - International Conference on Solid State Sensors and Actuators and Microsystems, TRANSDUCERS '05,* 2005, 2, 1146-1149.
116 S. Ohira and K. Toda, *Lab Chip,* 2005, 5, 1374-1379.
117 G. Yi, T. Thorsen, V. N. Manoharan, M. Hwang, S. Jeon, D. J. Pine, S. R. Quake and S. Yang, *Adv. Mater.,* 2003, 15, 1300-1304.

118 J. Wan, L. Shi, B. Benson, M. J. Bruzek, J. E. Anthony, P. J. Sinko, R. K. Prudhomme and H. A. Stone, *Langmuir,* 2012, 28, 13143-13148.
119 S. Hoi, X. Chen, V. S. Kumar, S. Homhuan, C. Sow and A. A. Bettiol, *Adv. Funct. Mater.,* 2011, 21, 2847-2853.
120 Y. Hu, C. Wang, Z. Wu, J. Xu, H. Chen and X. Xia, *Electrophoresis,* 2011, 32, 3424-3430.
121 A. M. Nightingale, A. D. Beaton and M. C. Mowlem, *Sens, Actuators, B Chem.,* 2015, 221, 1398-1405.
122 R. Pol, F. Céspedes, D. Gabriel and M. Baeza, *TrAC - Trends in Analytical Chemistry,* 2017, 95, 62-68.
123 G. Whitesides, *Lab Chip,* 2014, 14, 3125-3126.
124 R. Murray, *Anal. Chem.,* 2010, 82, 1569.
125 J. S. McGrath, J. Quist, J. R. T. Seddon, S. C. S. Lai, S. G. Lemay and H. L. Bridle, *PLoS ONE,* 2016, 11.
126 C. Sakamoto, N. Yamaguchi, M. Yamada, H. Nagase, M. Seki and M. Nasu, *J. Microbiol. Methods,* 2007, 68, 643-647.
127 V. A. VanderNoot, R. F. Renzi, B. P. Mosier, J. L. Van de Vreugde, I. Shokair and B. L. Haroldsen, *Electrophoresis,* 2010, 31, 2632-2640.
128 C. Páez-Avilés, E. Juanola-Feliu, J. Punter-Villagrasa, B. Del Moral Zamora, A. Homs-Corbera, J. Colomer-Farrarons, P. L. Miribel-Català and J. Samitier, *Sensors (Switzerland),* 2016, 16.
129 A. K. Balasubramanian, K. A. Soni, A. Beskok and S. D. Pillai, *Lab Chip,* 2007, 7, 1315-1321.
130 M. Kim, T. Jung, Y. Kim, C. Lee, K. Woo, J. H. Seol and S. Yang, *Biosens. Bioelectron.,* 2015, 74, 1011-1015.
131 T. M. Curtis, M. W. Widder, L. M. Brennan, S. J. Schwager, W. H. Van Der Schalie, J. Fey and N. Salazar, *Lab Chip,* 2009, 9, 2176-2183.
132 E. Tyrrell, C. Gibson, B. D. MacCraith, D. Gray, P. Byrne, N. Kent, C. Burke and B. Paull, *Lab. Chip,* 2004, 4, 384-390.
133 X. Zhao and T. Dong, *Int. J. Environ. Res. Public Health,* 2013, 10, 6748-6763.
134 M. Sierra-Rodero, J. M. Fernández-Romero and A. Gómez-Hens, *Microchim. Acta,* 2012, 179, 185-192.
135 J. Chen, S. Xiao, X. Wu, K. Fang and W. Liu, *Talanta,* 2005, 67, 992-996.
136 M. J. Shiddiky, M. S. Won and Y. B. Shim, *Electrophoresis,* 2006, 27, 4545-4554.
137 A. Fonseca, I. M. Raimundo Jr, J. J. Rohwedder, R. S. Lima and M. C. Araujo, *Anal. Bioanal Chem.,* 2010, 396, 715-723.
138 R. Olivé-Monllau, C. S. Martínez-Cisneros, J. Bartrolí, M. Baeza and F. Céspedes, *Sens. Actuators B, Chem.,* 2011, 151, 416-422.
139 R. Li, L. Wang, X. Gao, G. Du, H. Zhai, X. Wang, G. Guo and Q. Pu, *J. Hazard. Mater.,* 2013, 248-249, 268-275.
140 T. Leelasattarathkul, S. Liawruangrath, M. Rayanakorn, B. Liawruangrath, W. Oungpipat and N. Youngvises, *Talanta,* 2007, 72, 126-131.
141 M. del Mar Baeza, N. Ibanez-Garcia, J. Baucells, J. Bartroli and J. Alonso, *Analyst,* 2006, 131, 1109-1115.
142 A. Calvo-Lopez, E. Arasa-Puig, M. Puyol, J. M. Casalta and J. Alonso-Chamarro, *Anal. Chim. Acta,* 2013, 804, 190-196.
143 L. N. N. Nóbrega, L. D. O. Magalhães and A. Fonseca, *Microchem. J.,* 2013, 110, 553-557.
144 S. Fujii, T. Tokuyama, M. Abo and A. Okubo, *Anal. Sci.,* 2004, 20, 209-212.
145 J. Wang, M. P. Chatrathi, A. Mulchandani and W. Chen, *Anal. Chem.,* 2001, 73, 1804-1808.
146 B. M. Jayawardane, I. D. McKelvie and S. D. Kolev, *Talanta,* 2012, 100, 454-460.
147 N. A. Martinez, R. J. Schneider, G. A. Messina and J. Raba, *Biosens. Bioelectron.,* 2010, 25, 1376-1381.
148 J. Yakovleva, R. Davidsson, M. Bengtsson, T. Laurell and J. Emneus, *Biosens. Bioelectron.,* 2003, 19, 21-34.
149 S. Xue, K. Uchiyama and H. F. Li, *J. Environ. Sci. (China),* 2012, 24, 564-570.
150 L. Marle and G. M. Greenway, *Anal. Chim. Acta,* 2005, 548, 20-25.
151 Nuriman, B. Kuswandi and W. Verboom, *Sens. Actuators B, Chem.,* 2011, 157, 438-443.
152 J. Wang, H. Chen, P. Zhang, Z. Zhang, S. Zhang and J. Kong, *Talanta,* 2013, 114, 204-210.
153 W. Jung, A. Jang, P. L. Bishop and C. H. Ahn, *Sens. Actuators B, Chem.,* 2011, 155, 145-153.
154 M. Bowden, M. Sequiera, J. P. Krog, P. Gravesen and D. Diamond, *J. Environ. Monit.,* 2002, 4, 767-771.
155 C. Slater, J. Cleary, K. T. Lau, D. Snakenborg, B. Corcoran, J. P. Kutter and D. Diamond, *Water Sci. Technol.,* 2010, 61, 1811-1818.
156 M. Bowden and D. Diamond, *Sens. Actuators, B Chem.,* 2003, 90, 170-174.
157 I. M. Perez De Vargas Sansalvador, C. D. Fay, J. Cleary, A. M. Nightingale, M. C. Mowlem and D. Diamond, *Sens Actuators, B Chem.,* 2016, 225, 369-376.

158 Z. Zou, E. MacKnight, A. Jang, P. Wu, J. Do, P. L. Bishop and C. H. Ahn, *International Conference Miniaturized Systems for Chemistry and Life Sciences - Proc. MicroTAS Conf.,* 2008, 1251-1253.
159 H. Hwang, Y. Kim, J. Cho, J. Y. Lee, M. S. Choi and Y. K. Cho, *Anal. Chem.,* 2013, 85, 2954-2960.
160 F. E. Legiret, V. J. Sieben, E. M. Woodward, S. K. Abi Kaed Bey, M. C. Mowlem, D. P. Connelly and E. P. Achterberg, *Talanta,* 2013, 116, 382-387.
161 V. M. Rerolle, C. F. Floquet, A. J. Harris, M. C. Mowlem, R. R. Bellerby and E. P. Achterberg, *Anal. Chim. Acta,* 2013, 786, 124-131.
162 A. D. Beaton, V. J. Sieben, C. F. A. Floquet, E. M. Waugh, S. Abi Kaed Bey, I. R. G. Ogilvie, M. C. Mowlem and H. Morgan, *Sens. Actuators B, Chem.,* 2011, 156, 1009-1014.
163 A. D. Beaton, C. L. Cardwell, R. S. Thomas, V. J. Sieben, F. Legiret, E. M. Waugh, P. J. Statham, M. C. Mowlem and H. Morgan, *Environ. Sci. Technol.,* 2012, 46, 9548-9556.
164 M. Kim, W. Choi, H. Lim and S. Yang, *Desalination,* 2013, 317, 166-174.
165 Perez de Vargas Sansalvador,Isabel M., C. D. Fay, J. Cleary, A. M. Nightingale, M. C. Mowlem and D. Diamond, *Sens. Actuators B, Chem.,* 2016, 225, 369-376.
166 X. Cao, S. W. Zhang, D. Z. Chu, N. Wu, H. K. Ma and Y. Liu, *IOP Conference Series: Earth and Environmental Science,* 2017, 82.

3

Fabrication of 3D Structures by the *Origami* Technique*

3D microfluidic devices fabrication methods are normally quite expensive and tedious. This chapter presents an easy and cheap alternative for the fabrication of cyclic olefin copolymer and pressure sensitive adhesive hybrid 3D microfluidic structures by the *Origami* technique. This fast fabrication method was applied, as a proof of concept, for the generation of a micromixer with a 3D stepped serpentine design.

*****Parts of this Chapter have been published in: J. Saez; L. Basabe-Desmonts; F. Benito-Lopez, Low-cost *Origami* fabrication of 3D self-aligned hybrid microfluidic structures, *Microfluid. Nanofluid*., 2016, 20:216.

3.1 Introduction

Originally, developmental advances on microfluidic devices came from the microelectronics manufacturing sector. Traditionally, silicon was used as the base material for fabricating microfluidic devices for several applications[1]. The extensive study of silicon properties and its use in processing contributed to the rapid evolution of microfluidic technology. However, one of the main drawbacks of the use of silicon as fabrication material is that it is quite expensive, needs though microfluidic fabrication methods and that it is optically opaque to certain wavelengths, limiting its optical applications. To overcome these limitations, glass and polymeric materials gained more significance in recent years for the fabrication of microfluidic devices. Compared to silicon, glass and polymeric materials have the advantage of being cheap and optically transparent, although glass still needs expensive and tedious fabrication protocols, such as photolithography and etching procedures, for the fabrication of microfluidic devices. Polymers are materials that provide advantageous properties, less price and easy and cheap fabrication protocols. Some commonly used polymer materials include polymethylmethacrylate (PMMA), polydimethylsiloxane (PDMS), polystyrene (PS), polycarbonate (PC) or cyclic olefin polymer (COP)[2] as was explained widely in Chapter 2. Specifically, COP is being increasingly used for the fabrication of microfluidic systems due to its advantageous properties[3] that were also explained in Chapter 2.

The common microfluidic devices fabrication methods for COP such as injection moulding, hot embossing, X-ray lithography and micromilling are not accessible by most researchers. The common limiting factor for all these traditional methods is the expensiveness of the techniques and that the fabrication is usually tedious, involving costly equipment, long protocols and being time-consuming and needy of specially trained personnel as reviewed in Chapter 2 (see Table 2.2). However, the increasing microfluidic community, and in particular in the field of environmental monitoring, is demanding accessible, low-cost, on-demand and efficient methods for fast prototyping and fabrication of microfluidic devices. Fabrication methods for microfluidic devices using xurography[4] followed by thermo-compression or chemical bonding have gained interest due to their relatively rapid way of fabrication. Xurography, which uses a cutting plotter (a plotter that holds a knife), traditionally used in the design industry for cutting graphics in adhesive vinyl films, is able to produce very precise structures in the micrometer range, usually ≥ 200 µm.

Other rapid prototyping methods have been implemented for the fabrication of microfluidic devices as 3D printing[5, 6], computer numerical control (CNC) micromachining[7, 8] and CO_2 laser[9]. One common limiting factor for these techniques is that their resolution is quite low, more than 100 µm, except for micromachining. However, micromachining usually makes the surface of the channel rough and sometimes causes imperfect bonding. Moreover, the main drawback is that all these techniques require of costly equipment stations for fabrication. As an example, 3D printing, having lower resolution than xurography, is approximately 30 times more expensive.

In the literature, different bonding methods can be found for the fabrication of COP microfluidic devices both monolithic or hybrid[10-12]. Among these, direct bonding methods such as solvent bonding and thermal fusion bonding are the most commonly used[13]. Extensively, solvent bonding has emerged as an important method for sealing cyclic olefin copolymer (COC) microchannels[14].

PSA has appeared as an excelled alternative material for bonding or sealing microfluidic devices[15]. PSA has a high degree of tack with the ability to quickly wet the surface to which it is applied, providing instant bonding at low to moderate pressures. On the other hand, PSAs possess sufficient cohesion and elasticity so that despite their aggressive tackiness they can be handled with the fingers and removed from smooth surfaces without leaving any residue[16]. The type of PSA to be used in a microfluidic application depends on its chemical composition and should be chosen according to the use it is going to be given (biocompatible, transparent, opaque, conductive, insulator, *etc.*). Medical grade PSAs are selected for bio-medical applications due to their biocompatibility[17]. For instance, Yuen *et al.*[18] described a low-cost rapid prototyping method using a desktop digital craft cutter. They applied rapid prototyping and *xyz* alignment for the fabrication of hybrid laser printed transparency and PSA films 3D microfluidic devices within minutes. However, laser printer transparency films have poor wettability and a surface treatment with oxygen plasma was needed.

It is indisputable the synergy between COP and PSA materials for the fabrication of microfluidic devices. On this regards, a large number of papers can be found in the literature explaining the fabrication of COP microfluidic devices where PSA was used for bonding or sealing the device in applications such as the development of a device for monitoring anticoagulants at the point of care (POC)[19] or in the fabrication of optofluidic valves[20]. Nevertheless, in all their fabrication protocols, the different layers of COP and PSA were xurographied individually and manually staked together or through a mould before bonding.

In this way, the *Origami* technique, developed by Elizalde *et al.*[21] for COP and then applied by

Benito-Lopez *et al.*[22] for the fabrication of modular microvalve structures is of great interest. It consists of two steps: (1) folding a layer of a previously xurographied COP containing all the microfluidic structures and (2) a thermocompression step for the generation of the monolithic structures[23]. For instance, Benito-Lopez *et al.*[22], after the *Origami* fabrication of the 3D monolithic COP microfluidic device, used a PSA layer to seal the device (microvalve). With this method, a thermocompression step, using high pressure and high-temperature equipment, is necessary for the fabrication of the 3D COP structure.

In this Chapter, an easy, cheap, fast and universal way for the on-demand fabrication of COP-PSA hybrid 3D microfluidic structures by the *Origami* technique without the use of a thermocompression step is proposed. The COP and PSA layers were cut using a portable, low-cost cutting plotter (< €200). The layers were then assembled using the *Origami* technique combining COP and PSA and the final 3D hybrid microfluidic structure was bonded using just mild pressure with a roller. This enables the fabrication of hybrid COP-PSA microfluidic devices at any type of laboratories by just acquiring a low price plotter and the COP and PSA sheets. This technique is accessible in most cases, for example, in low resource areas or in educational institutions, making the fabrication protocol multidisciplinary. This fabrication technique was applied for the construction of an elaborated micromixer that consists of a 3D stepped serpentine design as a proof of concept.

3.2 Experimental

3.2.1 Experimental Set-up and Materials

Zeonor COP sheets of 100 µm thickness were purchased by Zeonex (Düsseldorf, Germany). ArCare® 8939 PSA of 127 µm double side roll was generously provided by Adhesive Research (Limerick, Ireland).

A Silhouette Portrait® (Lehi, UT, USA) was used as a cutting plotter for the cutting of the COP and PSA layers.

A Harvard Apparatus 11 elite syringe pump (Holliston, MA, USA) was used for the injection of the two liquids into the mixer. 1 mL syringes from Novica Medica (Barcelona, Spain) with precision tips from Nordson EFD (Bedfordshire, UK) connected to 1/16” ID Tygon tubing from Colme-Palmer (Vernon Hills, IL, USA) and male luers that were coupled to female luers with a base from ChipShop (Jena, Germany). A rubber roller was purchased from Rotulatienda (Jerez, Spain).

The failure pressure of the microfluidic device was measured and controlled with an MSFC® from Fluigent (Villejuif, France).

For the visual monitoring of the mixing, yellow and red food dyes from McCormick (Sabadell, Spain) were used.

3.2.2 Channel Dimensions and Device Fabrication

The channel width is defined by the cutting process of the plotter. Therefore, channels of different widths were cut: 1000, 500, 250, 100, 50 and 25 µm. It was observed that the fabrication of channels smaller than 250 µm was not possible since all those generated channels were obtained with dimensions of 250 ± 20 µm. This is a limitation of the current fabrication technology.

During the assembly of the device, using the *Origami* technique, it was found out that the minimal channel dimensions that generated an operative microfluidic device were 500 µm. Channels of 250 µm did not get properly aligned during the *Origami* process so the devices were inoperative.

3.2.3 Micromixer Performance

In order to prove the fabrication method, the microfluidic device design was envisioned as a micromixer. The performance of the micromixer was tested using yellow and red solutions injected into the microfluidic device by a syringe pump. The solutions were prepared by mixing 5 mL of water with 20 µL of the corresponding food dye (yellow or red). The solutions were injected at a constant flow (5 µL min^{-1}) for 5 min and the visualisation of the mixing process of both dyes through the stepped serpentine was achieved by eye.

3.3 Results and Discussion

3.3.1 Fabrication of the Micromixer

Generally, POC systems integrate microscale mixers to enhance biochemical interactions[24] or speed up chemical reactions[25]. It is occasionally convenient to have these micromixers as independent entities that can be coupled to the main microfluidic device on-demand following a modular approach. Therefore, as a proof of concept, a simple 3D fabrication technique was developed for the on-demand fabrication of COP/PSA microfluidic structures to be used as passive micromixers.

After AutoCAD design of the 3D structures, both the COP and the PSA designs were cut in a single step with the Silhouette Portrait®. The benefits of using this type of equipment are its portability (less than 1.6 kg and 20 x 40 cm dimensions) and its extremely low-cost < €200. Moreover, the plotter allows the fast design, fabrication and subsequent tests of microfluidic devices for a huge variety of applications to laboratories without access to clean room facilities or with low resources. Although customised designs with feature resolution of 100 µm can be designed with the cutter software, it was found out that it is very difficult to achieve a clean good quality cut for 100 µm widths. The plotter is able to generate structures, microfluidic channels, down to 200 µm in width in both COP and PSA of different thicknesses.

Micromixers are generally designed with channel geometries that decrease the mixing path and increase the contact surface area[26]. The micromixer design was visualised as a 3D stepped serpentine. The 3D design was sliced into five 2D layers of COP and another five 2D layers of PSA, separating the different sections by a dotted line. This dotted line ensures the precise bending of the layers. The 3D serpentine was envisioned with four steps connected by channels. Each of the channels has the dimensions of 1 mm width and 8 mm length. Moreover, the two inlets form a T-shape as illustrated in Figure 3.1.

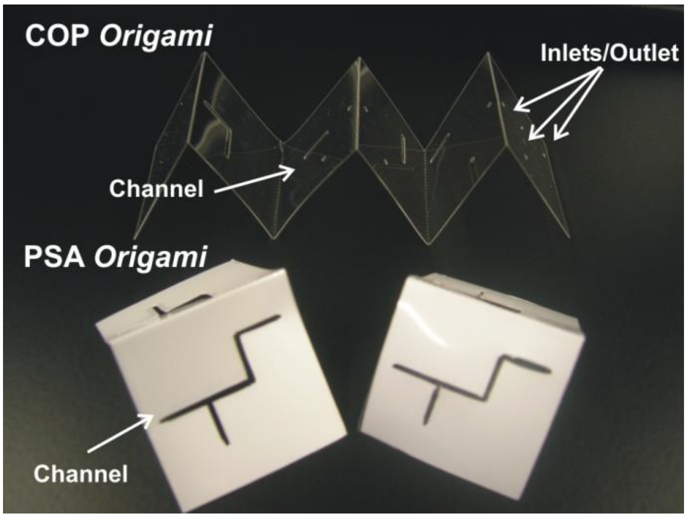

Figure 3.1: COP and PSA layers after xurography and bending (following the dotted lines) showing the inlets/outlet and channels in detail.

In short, COP or PSA sheets were set on the plotter carrier-sheet and slightly pressurised with the roller to ensure that the sheets remind fixed to the carrier during all the cutting process, Figure 3.2. The COP or PSA sheets were cut and the excised material was removed by scratching with a precision tip.

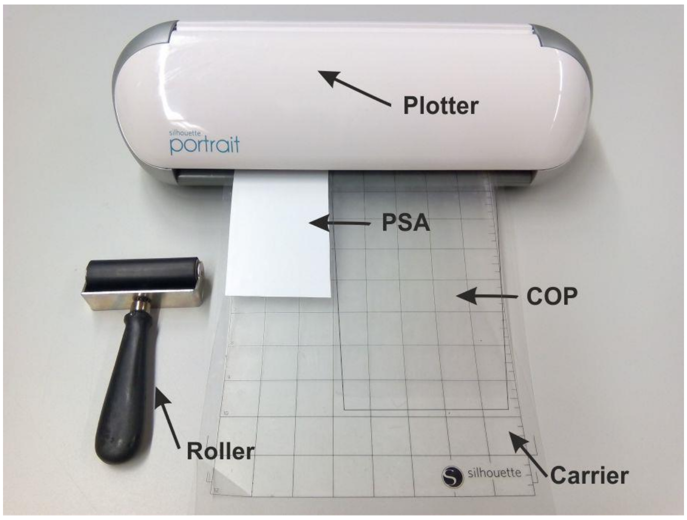

Figure 3.2: Silhouette Portrait plotter set-up for rapid prototyping and roller.

Once the COP and PSA sheets were cleaned with air and folded along the dots lines as shown in Figure 3.1, folded double side PSA layers were used as bonding agents of the COP sections, as represented in Figure 3.3, following this protocol:

1) One of the PSA layers is able to bond three sections of the COP layer. It has to be carefully checked that no air bubbles or wrinkles in the COP or in the double side PSA get trapped during folding.
2) The other PSA layer bonds other three sections of the COP layer, on the opposite side of the COP layer.
3) Then the last available section of the PSA layer (from two) bonds together the two sides of the COP layer.
4) After the device was totally assembled, the device alignment was achieved by using two crystals to sandwich the layers and a microscope.

The manual assembly of the different sections of the channels causes a small misalignment in the final channel of the device. The width of the channel was calculated to be in the *Y-axis* 944 ± 2 µm (n = 3) and in the *X-axis* 938 ± 2 µm (n = 3), which is in the same range of the misalignments generated during the fabrication of the monolithic 3D COP devices proposed by Elizalde *et al*.[21]

The final micromixer is composed of six layers of COP, 100 µm thickness each, and five layers of PSA, 127 µm thickness each, with a section of 2.5 cm^2 and 1.135 mm in total thickness as illustrated in Figure 3.4.

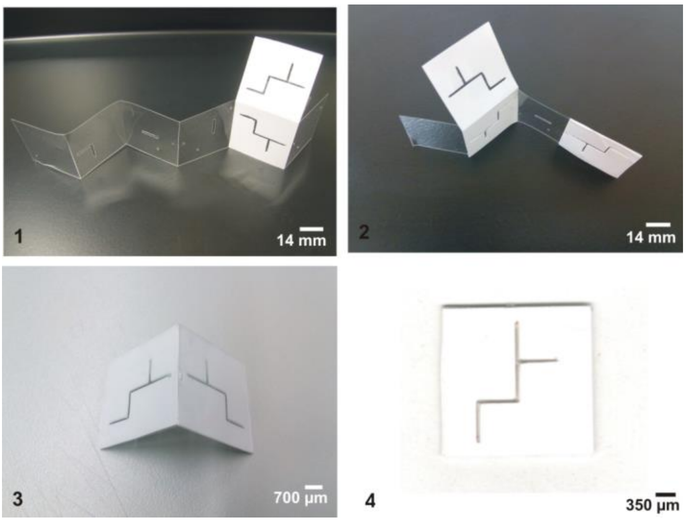

Figure 3.3: Set of pictures showing 1) PSA bonds to one COP section. 2) PSA folds and bonds to the other side of the COP section. 3) Both sides bonded by PSA. 4) Micromixer assembled.

Although the micromixer was fabricated as a modular entity that can be used independently, the same fabrication protocol could be applied for the fabrication of fully functional microfluidic devices. Moreover, since the fabrication protocol uses biocompatible materials, this makes it very interesting for fast prototyping of microfluidic devices for POC applications in laboratories that do not have access to microfabrication facilities.

The advantages of the different bonding techniques found in the literature for COP xurography, compared with this new *Origami* technique, are summarised in Table 3.1.

Table 3.1: Advantages of the different bonding techniques for COP xurography.

	Bonding Method		
Advantage	**Solvent**[21, 27-29] *****	**Thermocompression**[13, 21, 29] *****	**COP/PSA O*rigami***
Low cost	X	X	√
Low power	√	X	√
Portable	X	X	√
Fast fabrication times	X	X	√
Clean room free	X	X	√
Bonding steps	4	3	2
Equipment needed	Heater/Pressure	Heater	None

**Sometimes complemented with a surface treatment step*[13].

3.3.2 Characterisation of the Micromixer

To determine the mixing performance, two colored liquids, yellow and red, were mixed. A standard double syringe pump with two 1 mL syringes was used to introduce the liquids at 1, 3, 5, 7, 15 and 20 µL min^{-1}, respectively, in the micromixer. The results showed that for any of the flows applied, a uniform mixing along the channel was achieved as deduced by the observation of a homogeneous orange colour at the outlet. The mixing was achieved even at high flows (20 µL min^{-1}), see Figure 3.4 (right).

At the beginning of the injection, the first step of the micromixer, the laminar flow of the two solutions was appreciable at high flow rates. Nevertheless, this phenomenon rapidly disappears at the beginning of the second step (after the 8 mm channel), when both solutions get in contact and mix when jumping to the second step of the micromixer. During the third and the fourth step, the colour of the solution is completely mixed and homogeneous (orange).

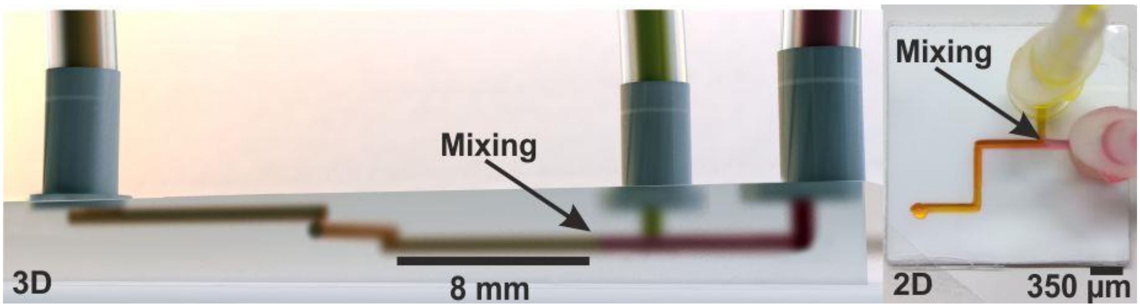

Figure 3.4: Scheme of the micromixer in 3D view (left) and a 2D view of the micromixer performance when introducing the red and yellow dye solutions at 20 µL min^{-1} (right).

In order to evaluate the strength of the bonding process during *Origami* bending, pressure robustness tests were carried out with the micromixers. To do that, two reservoirs of 1 mL volume were filled with deonised water and 50, 100, 500 and 1000 mbar of pressure were applied with the MSFC®, see Figure 3.5. This protocol was applied several times to each of the devices to ensure their reusability at those pressures. It was found out that all the micromixers could hold up to 1000 mbar (n = 5; 5 different devices) of pressure without any damage. None of the devices tested suffered any damage during the pressure tests. Moreover, all the devices were reused many times (> 8 times) at atmospheric pressure without losing their functionality.

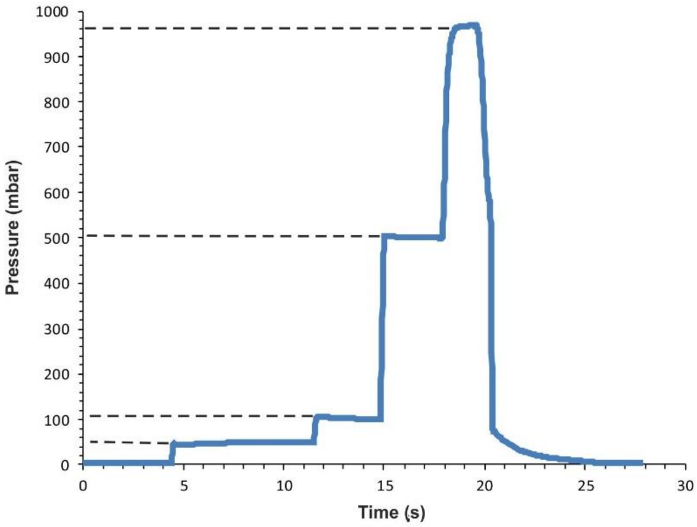

Figure 3.5: Pressures that the micromixer can hold: steps at 50, 100, 500 and 1000 mbar, respectively. The drop of the signal at time 20 s is due to the emptying of the 1 mL reservoir.

3.4 Conclusions

An easy and fast fabrication method of hybrid 3D COP-PSA microfluidic structures by the *Origami* technique was shown in this Chapter. A Silhouette Portrait plotter, a very cheap equipment alternative, which is portable and allows fast fabrication of microfluidic structures for different applications at any setting, was used to cut the devices. The assembly of the devices was carried out using the *Origami* technique combining layers of COP and PSA that bent and bonded to each other as an *Origami*. No thermocompression was required, and just a soft compression with a hand roller was necessary. This fabrication protocol was used for the generation of a 3D stepped serpentine micromixer. The micromixers were found to be efficient even at high flows (20 µL min^{-1}) and able to stand pressures up to 1000 mbar.

This new fabrication protocol has implications on the easy and low-cost production of microfluidic structures, such as micromixers, which are of high relevance for many microfluidic applications in environmental and water quality analysis at the point of need.

3.5 References

1 K. F. Lei, *RSC Detect. Sci.,* 2015, 7, 1-28.
2 M. F. Maitz, *Biosurf. Biotrib.,* 2015, 1, 161-176.
3 R. P. Gandhiraman, C. Volcke, V. Gubala, C. Doyle, L. Basabe-Desmonts, C. Dotzler, M. F. Toney, M. Iacono, R. I. Nooney, S. Daniels, B. James and D. E. Williams, *J. Mater. Chem.,* 2010, 20, 4116-4127.
4 D. Bartholomeusz A., R. Boutté W. and J. Andrade D., *IEEE/ASME J. Microelectromech. Syst.,* 2005, 14, 1364-1374.
5 A. K. Au, N. Bhattacharjee, L. F. Horowitz, T. C. Chang and A. Folch, *Lab Chip,* 2015, 15, 1934-1941.
6 C. M. B. Ho, S. H. Ng, K. H. H. Li and Y. Yoon, *Lab Chip,* 2015, 15, 3627-3637.
7 K. Sugioka, J. Xu, D. Wu, Y. Hanada, Z. Wang, Y. Cheng and K. Midorikawa, *Lab Chip,* 2014, 14, 3447-3458.
8 B. Ziaie, A. Baldi, M. Lei, Y. Gu and R. A. Siegel, *Adv. Drug Deliv. Rev.,* 2004, 56, 145-172.
9 B. L. Thompson, Y. Ouyang, G. R. Duarte, E. Carrilho, S. T. Krauss and J. P. Landers, *Nat. Protoc.,* 2015, 10, 875-886.
10 K. Liu, P. Gu, K. Hamaker and Z. H. Fan, *J. Colloid Interface Sci.,* 2012, 365, 289-295.
11 S. T. Sanjay, G. Fu, M. Dou, F. Xu, R. Liu, H. Qi and X. Li, *Analyst,* 140, 7062-7081.
12 S. T. Sanjay, G. Fu, M. Dou, F. Xu, R. Liu, H. Qi and X. Li, *Analyst,* 2015, 140, 7062-7081.
13 C. W. Tsao, L. Hromada, J. Liu, P. Kumar and D. L. DeVoe, *Lab Chip,* 2007, 7, 499-505.
14 T. I. Wallow, A. M. Morales, B. A. Simmons, M. C. Hunter, K. L. Krafcik, L. A. Domeier, S. M. Sickafoose, K. D. Patel and A. Gardea, *Lab Chip,* 2007, 7, 1825-1831.
15 F. A. Keimel, *Handbook of Adhesive Technology,* ed. A. Pizzi and K. L. Mittal, 2003, pp.1-12.
16 I. Benedek, *Pressure sensitive adhesives and applications.*, Marcel Dekker, Inc., New York, 2004.
18 P. K. Yuen and V. N. Goral, *Lab Chip,* 2010, 10, 384-387.
19 L. F. Harris, P. Rainey, V. Castro-Lopez, J. S. O'Donnell and A. J. Killard, *Analyst,* 2013, 138, 4769-4776.
20 J. L. Garcia-Cordero, D. Kurzbuch, F. Benito-Lopez, D. Diamond, L. P. Lee and A. J. Ricco, *Lab Chip,* 2010, 10, 2680-2687.
21 J. Elizalde, M. Antoñana, L. Matthys, F. Laouenan and J. M. Ruano-López, In *International Conference on Miniaturized Systems for Chemistry and Life Sciences , MicroTAS,* 2013, 2, 790-792.
22 F. Benito-Lopez, M. Antoñana-Díez, V. F. Curto, D. Diamond and V. Castro-López, *Lab Chip,* 2014, 14, 3530-3538.
23 K. Kuribayashi-Shigetomi, H. Onoe and S. Takeuchi, *PLoS ONE,* 2012, 7, 51085-51092.
24 A. Cosentino, H. Madadi, P. Vergara, R. Vecchione, F. Causa and P. A. Netti, *Sci. Rep.,* 2015, 5, 1-10.
25 P. Chen, Y. Chen and C. Tsai, *Microelectron Eng.,* 2016, 150, 57-63.
26 L. Capretto, W. Cheng, M. Hill and X. Zhang, *Top. Curr. Chem.,* 2011, 304, 27-68.
27 I. R. G. Ogilvie, V. J. Sieben, C. F. A. Floquet, R. Zmijan, M. C. Mowlem and H. Morgan, *J Micromech Microeng.,* 2010, 20, 065016-065024.
28 D. A. Mair, M. Rolandi, M. Snauko, R. Noroski, F. Svec and J. M. J. Fréchet, *Anal. Chem.,* 2007, 79, 5097-5102.
29 P. S. Nunes, P. D. Ohlsson, O. Ordeig and J. P. Kutter, *Microfluid. Nanofluid.,* 2010, 9, 145-161.

4

In-situ Generation of Biocompatible Alginate Microvalves in a Microfluidic Device*

This Chapter describes the use of alginate hydrogels as miniaturised microvalves within microfluidic devices. These biocompatible and biodegradable microvalves were generated *in-situ* and on demand, allowing for microfluidic flow control. The microfluidic devices were fabricated using an *Origami* technique of folding several layers of cyclic olefin polymer (see Chapter 3) followed by thermal compression bonding. The hydrogels could be dehydrated at mild temperatures or chemically erased using ethylenediaminetetraacetic acid disodium salt solution to completely open the channel, ensuring the reusability of the whole device.

*****Parts of this Chapter have been published in: J. Saez; J. Etxebarria; M. Antoñana-Diez; F. Benito-Lopez, On-demand generation and removal of alginate biocompatible microvalves for flow control in microfluidics, *Sens. Actuators B: Chem.,* 2016, 234, 1-7.

4.1 Introduction

Lab on a Chip (LOC) is a multidisciplinary area of science that covers chemistry, physics, engineering, and biotechnology, aiming at the miniaturisation of devices for fluidic handling and detection. The driving force behind miniaturisation is to enhance performance by down-scaling analytical systems and to integrate multiple components into a single device[1]. LOC devices offer many advantages[2] as was explained in Chapter 2.

The current state-of-the-art for microfluidic devices is based on flow systems that employ traditional pumping, valving and mixing components. These systems are generally expensive, difficult to integrate into a microfluidic device and, most of the times, can only be controlled from external sources, as for example solenoid valves[3, 4]. Nevertheless, scientists are making efforts on improving these microfluidic components, as demonstrated in the previous chapter with a micromixer component. In particular, valve components are of great importance, where novel valves such as "Quake" PDMS micro-valves[5], "Doormat" valves[6] and check valves[7] among others, have recently appeared. These valves have been proved effective and less costly but still need to be designed within the microfluidic device and/or integrated after the device is ready. The *in-situ* generation of them on desire, and subsequent removal after use, has not been reported yet. Therefore, the trend is to develop novel flow systems, cheaper and easier to fabricate with these types of microvalves.

A very interesting alternative for microvalve integration in microfluidic devices is the use of smart materials for fluid handling and control[8]. In particular, hydrogels are network polymer chains that are highly water absorbent and that possess a substantial degree of flexibility. The ability of hydrogels to absorb water arises from hydrophilic functional groups attached to the polymeric backbone, while their resistance to being dissolved comes from the cross-links between the network chains of the hydrogel[9]. They can be identified as stimuli-responsive materials able to undergo volumetric changes in response to physical and chemical changes in their local environment[10]. Is their ability to change these properties, in a controllable manner, what has made hydrogels polyvalent materials in many application fields. The chemistry used to synthesise hydrogels, within their corresponding activating stimuli, is as diverse as their potential applications.

In particular, calcium alginate is a water-insoluble hydrogel formed from linear copolymers of anionic polysaccharide (water-soluble) and calcium cations that make crosslinks between chains. The gelling properties of alginate depend strongly upon its monomeric composition, block structure, molecular size and concentration of the polymer and calcium ions[11]. This polymer is one of the most used biomaterials in science due to its biocompatibility and biodegradability[12].

Alginates are extremely versatile biopolymers, which have been used in a variety of technical biomedical[13] and pharmaceutical[14] applications. They have been also extendedly used in the food industry because they are powerful thickening, stabilising, and gel-forming agents. Surprisingly, in microfluidic applications, alginates have been rarely used, primordially for reagent storage in chips and for the fabrication of microcapsules in drug delivery systems[15].

The recent advances in microtechnology for biomedical applications, with products getting into the market[16], have increased the necessity to integrate stimuli-responsive materials with biocompatible capabilities within microfluidic devices; therefore, gels obtained from natural polymers are good alternatives[17]. In particular, the use of smart materials as actuators, with innocuous chemical characteristics, will open the door to the generation of novel microfluidic devices for biological applications.

This chapter describes the use of calcium alginate hydrogels as miniaturised valves in microfluidic devices as good alternatives to conventional hydrogel microvalves. These biocompatible and biodegradable microvalves are *in-situ* generated on demand, allowing for microfluidic flow control. As calcium alginate is dehydrated at room temperature (syneresis process), it can be thermally actuated at mild temperatures, slightly unblocking the channel and, in turn, restoring the flow rate, allowing to chemically erase the microvalve from the main channel simply using an ethylenediaminetetraacetic acid disodium salt (EDTA) solution, and so ensuring the reusability of the whole device.

4.2 Experimental

4.2.1 Materials

Sodium alginate was purchased from Sigma-Aldrich (St Louis, MO, USA). Calcium chloride dehydrated from Sigma-Aldrich (Madrid, Spain) was used to prepare the–calcium alginate hydrogel. EDTA was purchased from Merck (Darmstadt, Germany) and was used to chemically erase the calcium alginate hydrogel. All the solutions were prepared using deonised (DI) water from a Milli-Q water purification system from Merck Millipore (Milford, MA, USA).

Isopropyl alcohol (IPA) was purchased from Panreac Química S.L.U. (Barcelona, Spain). Rolls of 100 µm thick of Cyclo Olefin Polymer (COP) films (ZeonorFilm®) were obtained from Zeon Chemicals (Düsseldorf, Germany). This material was chosen because of its good properties such as biocompatibility, acid and base attack resistance and transparency.

Accura Amethyst was purchased from 3D Systems (Valencia, CA, USA) for the fabrication of the luers by the stereolithography technique and were coupled to the device with screws.

The flow in the microfluidic device was controlled using a WPI SP120PZ syringe pump that was purchased from World Precision Instruments (Shangai, China). Alternatively, solutions were injected with a Harvard Apparatus model 11 elite syringe pump (Holliston, MA, USA). An MFCS^{TM}-EZ pressure driven flow controller from Fluigent (Villejuif, France) was used for the injection of solutions. An SLG-0075 flow sensor from Sensirion CMOSens© (Staefa, Switzerland) was connected for the monitoring of solutions inside the microfluidic device.

4.2.2 Microfluidic Device Fabrication

Microfluidic devices were designed and fabricated by the *Origami* technique[18] by rapid prototyping using the FC-8000-60 cutting plotter from Graphtec (Irvine, CA) using a similar process than the one described in Chapter 3. The 3D design was sliced into several 2D layers, which were cut with the cutting plotter, assembled and then bonded by thermocompression[19]. This fabrication protocol differs from the one in the previous chapter by the use of COP sheets for the fabrication of the microfluidic device and by the need of a final thermocompression step. This protocol was chosen here, and not the one presented in Chapter 3, in order to generate monolithic COP microfluidic devices to avoid non-uniform alginate valves. Stereolithography 3D-printed interconnections for fluidic handling were in-house fabricated and coupled to the device with screws. These interconnections are coupled to 1mL ICO+3 type syringes from Novico Medica (Barcelona, Spain) and/or to male PMMA luers from Chipshop (Jena, Germany) and Tygon 0.8 x 2.4 mm tubes from Cole-Palmer (Vernon Hills, IL, USA).

4.2.3 Hydrogel Preparation

For the hydrogel preparation, typically, water solutions of 4 % of calcium chloride and 1 % of sodium alginate were prepared[20]. When the sodium alginate is added to a calcium chloride solution, the calcium ions replace the sodium ions in the polymer and it jellifies. The “egg-box model” for the formation of alginate polymers in the presence of alkaline metals was first described by Rees *et al.*[21], as depicted in Figure 4.1. The model describes that divalent cations, such as Ca^{2+}, are coordinated within the cavities of alginate chains[22]. A second alginate strand can also connect at the calcium ion, forming a link in which the calcium ion attaches two alginate strands together. The result is a chain of calcium-linked alginate strands that form a solid polymer.

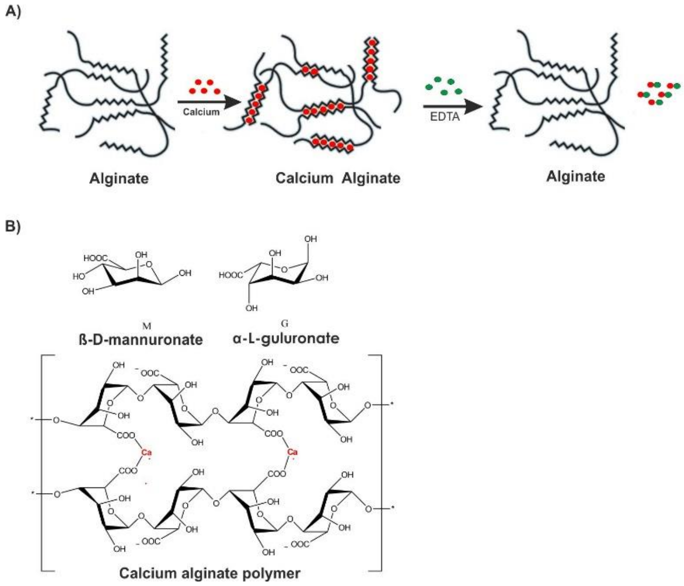

Figure 4.1: Schematic representation of A) the calcium alginate polymer formation and B) chemical structure of the calcium alginate polymer.

In order to perform this reaction in the microfluidic device and generate a functional microvalve in a controlled manner, calcium alginate beads were first synthesised in the bench. For this, a syringe was filled with the sodium alginate solution and 500 µL of the liquid were added to a calcium chloride solution bath, allowing polymerisation. Then, the reaction was stopped by putting the beads into a water bath.

4.3 Results and Discussion

4.3.1 Microfluidic Device Fabrication

In order to prove the concept, the microfluidic device was envisioned first with a simple T-shape configuration containing seven 100 µm thick COP layers, with a main channel stream of 1 mm width and with a perpendicular channel of 500 µm for the microvalve generation (Prototype 1). COP was used in order to guarantee the biocompatibility of the whole device. Nevertheless, a more sophisticated microfluidic design was later fabricated in order to independently control de

$CaCl_2$, EDTA and alginate solutions from the main channel stream (Prototype 2). This second generation was fabricated including an additional set of COP layers, where the EDTA microchannel is placed with a V-shape (1 mm width, 200 µm height) above the generated microvalve, in order to independently control its removal.

Figure 4.2 (A and D) shows the schemes of both prototypes. Figure 4.2 (B) shows an unfolded *Origami* prototype 1 sliced in seven layers of COP and Figure 4.2 (E) shows prototype 2 sliced in nine layers of COP. The microfluidic devices contain the inlets/outlet, the main channel and the perpendicular channel in prototype 1 and an additional V-shape channel in prototype 2. Figure 4.2 (C and F) presents the prototypes 1 and 2, respectively, after thermocompression with the stereolithography interconnections coupled with screws. This type of interconnector guarantees no leakage during the experiment up to 1 bar of pressure and has the possibility of being connected directly to a syringe or to commercially available fittings coupled to a tubing and then to the syringe.

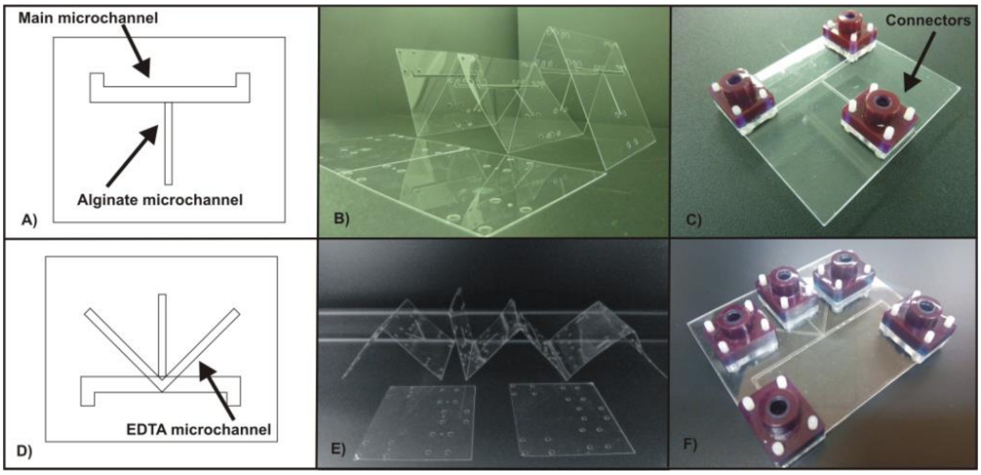

Figure 4.2: Prototype 1 schematic design (A), unfolded *Origami* (B) and after thermocompression (C). Prototype 2 schematic design (D), unfolded *Origami* (E) and after thermocompression (F), respectively.

4.3.2 Hydrogel Characterisation

Two approaches were followed to find the best conditions for the calcium alginate microvalves generation and removal in the microfluidic device. Firstly, the percent weight/volume % (w/v) for each sodium alginate/water and calcium chloride solutions was, on the bench, optimised. Secondly, the flow rate of each solution into their corresponding channels was investigated.

For the characterisation of the optimum w/v percentage per solution, several proportions of sodium alginate were tested. 0.6 %, 1 %, 2 % and 4 % of sodium alginate solution were tried in order to select the most adequate solution to be employed in the microfluidic device. It was found that 1 % (w/v) sodium alginate ensures homogeneous polymerisation, fast polymerisation times and low viscosity to facilitate the flow of alginate solution into the microfluidic device. The calcium chloride concentration was optimised selecting a concentration which showed the best performance respecting to the structural resistance of the formed calcium alginate (η). This result was obtained for a 4 % w/v calcium chloride solution, obtaining the same results than the work previously described by Blandino *et al.*[11]. With this percentage, the structural resistance of calcium alginate polymers, that is, their robustness, is uniform. It was observed that η tends to decrease when more concentrated solutions were used. This reduction in the η value is known to be due to the increase in diffusional resistance that Ca^{2+} ions suffer in their flux through a thicker membrane (η decreases with increasing diffusional resistance). A similar behaviour was reported as well by Yajima *et al.*[15].

In order to chemically erase the microvalve a 0.5 M water solution of EDTA was found to be enough for that purpose.

4.3.3 Alginate Microvalve *in-situ* Generation

The prototype 1 was connected to the pressure driven flow controller that controls the pressure and flow of calcium chloride solution independently from the sodium alginate solution into the microfluidic device. As highlighted in the experimental section, the microvalves were *in-situ* fabricated using 1 % (w/v) sodium alginate and 4 % (w/v) $CaCl_2$ solution.

For the fabrication of the microvalve, the $CaCl_2$ solution was flowed (Figure 4.3 A) through the main microchannel using the pressure driven flow controlled at 60 µL min^{-1}. In the meantime, the alginate solution coming from the perpendicular channel reaches the T-intersection section of the microchannel (~ 1500 µm length, Volume: 1.05 µL) after a small air plug (~ 200 µm length) as a manually controlled fast flow pulse using a syringe, as depicted in Figures 4.3 B and 4.3 C. Figure 4.3 C presents an *in-situ* generated microvalve in the main microchannel and in the top right an alginate bead fabricated outside the microfluidic device for comparison. It is appreciated in Figure 4.3 C that both generated alginate polymers (on-chip and on the bench) present similar physical configurations with no appreciable fabrication damages or cracks. In the intersection, the calcium cations of the calcium chloride solution penetrate by diffusion into the sodium alginate solution plug and start polymerising the alginate, resulting in hydrogel formation. By introducing the alginate into the calcium solution, anisotropic polymerised particles with broad size distributions were formed at first due to differences in the diffusion rate of calcium throughout the alginate[23]. The amount of sodium alginate solution and the shape of the generated microvalve in the microfluidic device were controlled by the speed of the alginate plug. It should be mentioned here that it is quite difficult to control the shape of the microvalve since the hydrophobicity of the COP microchannel is not enough to prevent the alginate solution to expand throughout the main microchannel (see the shape of the microvalve in Figure 4.3 C). Nevertheless, the generated alginate plug is sufficient to ensure a physical barrier to close the main microchannel and so to act as a microvalve. A well-defined microvalve could be generated by mechanically controlling the sodium alginate solution plug.

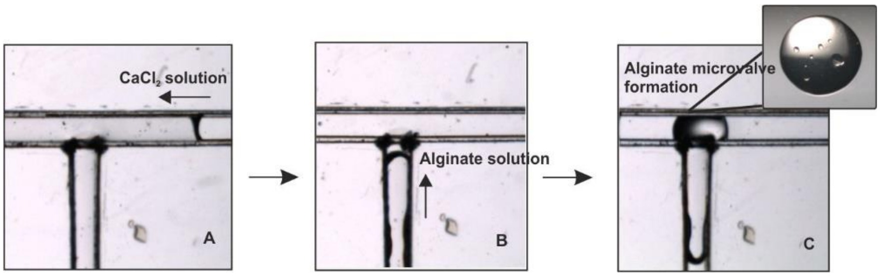

Figure 4.3: Set of pictures over time showing the alginate microvalve formation. The inset in Figure 4.3 C is a photo of a calcium alginate bead generated outside the microfluidic device for comparison.

4.3.4 Alginate Microvalve Characterisation

Figure 4.4 A, shows the flow profile within the microfluidic channel during *in-situ* microvalve formation using a commercial flow sensor. The flow sensor was placed after the microfluidic device. In this case, the $CaCl_2$ solution that flows through the main channel (ON configuration) was set to just 3 µL min^{-1}, a small flow, in order to be able to observe the formation of the microvalve. The flow in the main channel decreased to almost 0 µL min^{-1} when the microvalve is fully formed and the channel is blocked (OFF configuration). The microvalve formation time is 40 ± 7 s (n = 4) for this particular microfluidic configuration.

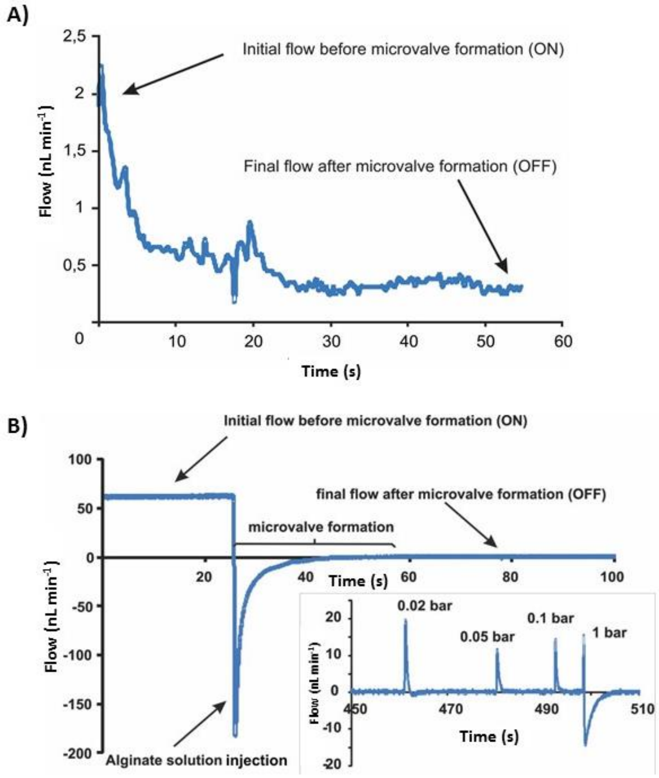

Figure 4.4: (A) Flow profile in the main channel of the microfluidic device during alginate microvalve fabrication (flow sensor placed at the outlet of the microfluidic device). (B) Flow profile in the main channel during alginate microvalve fabrication (flow sensor placed at the inlet of the microfluidic device). Inside: microvalve pressure failure experiments, carried out with the same microvalve.

Although the experimental conditions on the bench and microfluidic devices are not entirely comparable, the formation time in the microfluidic devices correlates well with the formation of calcium alginate beads on the bench. On the bench, the calcium alginate starts polymerising instantly, first at the surface of the sodium alginate bead, maintaining the shape of the bead. Later, alginate drops get harder with time while in contact with the calcium chloride solution. The core of the sodium alginate bead/microvalve is at the beginning “unreactive” but with time the ion exchange moves towards the centre from the surface and forms a complete calcium alginate structure, as described by Kim *et al.*[24].

The fluctuations in the signal, with a maximum in the range of 0.20 µL min^{-1}, could be attributed to fluctuations in the flow due to the reorganisation of the alginate polymer during formation or accommodation of the generated polymer to the channel configurations. The reason why the flow signal does not reach 0 µL min^{-1} can be attributed to:

(1) *the alginate polymer porosity*; this can be reduced by increasing the immersion time of alginate in the calcium solution and/or decreasing the ratio between mannuronic units and guannuronic units (M/G) in the sodium alginate. Calcium alginate films with higher concentration of G were proven to have significantly lower water vapour permeabilities (WVP) compared to films with higher concentration of M. It was reported that the immersion time and the M/G ratio of sodium alginate are therefore the key steps for producing calcium alginate films with low WVP and so less porosity[25].

(2*) inadequate assembly of the alginate microvalve with the microchannel walls.* In order to minimise this effect, other T-junction configurations with a more circular or oval shape could be fabricated to better accommodate the generated microvalve.

In order to characterise the pressure resistance of the microvalve, microvalve failure pressure experiments were carried out. The flow sensor was located before the prototype 1 and a 60 µL min^{-1} flow of $CaCl_2$ was set into the main microchannel meanwhile a controlled pulse flow of sodium alginate was applied into the vertical microchannel (see the experimental section). At the T-junction, the polymerisation of the calcium alginate took place and so the formation of the microvalve. Once the $CaCl_2$ flow decreased to virtually 0 µL min^{-1} the microchannel is blocked (OFF). In this particular experiment, the microvalve formation appears negative due to the big fluctuation generated in the flow sensor signal when the alginate solution is injected into the main channel. Failure pressure experiments were carried out then by applying incremental pressures to the microvalve from the main channel when the microvalve is OFF. The failure pressure value of the microvalve was tested for 0.02, 0.05, 0.1, and 1 bar and it was observed that some of the microvalves could hold up to 1 bar of pressure. Nevertheless, the fluctuations in the flow signal after applying 1 bar of pressure evidence that the microvalve is not stable at such a pressure for a long time.

4.3.5 Alginate Microvalve Actuation

As calcium alginate exhibits the phenomenon of syneresis the polymer can, therefore, be actuated by temperature. Syneresis is the spontaneous release of bound water with contraction of the hydrogel volume. Therefore, the blocking generated by the microvalve in the microchannel can be partially reverted at mild temperatures, for instance, 37 °C, as presented in Figure 4.5 with a bead on the bench and on the microfluidic device. Although this actuation is not reversible, the microvalve is able to shrink up to 20 % of its initial volume, allowing the liquid to flow again.

This syneresis effect of the microvalve facilitates non-contact operation and therefore independent manipulation of liquids in multiple microfluidic channels within an integrated microfluidic manifold simply by positioning heaters below the microchannels. It is clear that such dehydration of the hydrogel microvalves has the potential to greatly improve fabrication processes. Moreover, this thermal process could be used to allow the injection, through the main microchannel, of the EDTA solution and so completely erase the alginate microvalve when the microvalve completely blocks the microchannel when using very simple microfluidic configurations as the one represented by prototype 1.

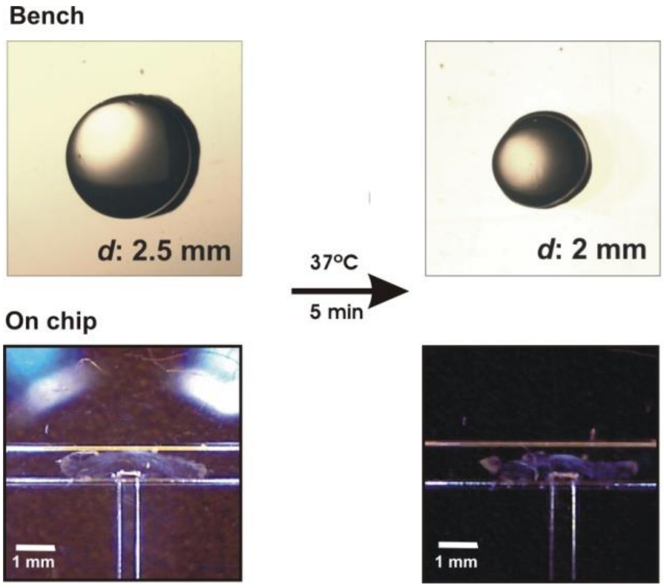

Figure 4.5: Dehydration of an alginate bead on the bench and on-chip, respectively.

4.3.6 Removal of the Alginate Microvalve

The stability of the calcium alginate hydrogel depends on the stability of calcium complexes within the hydrogel[26]. Thus, chelating agents that strongly bind calcium can quickly solubilise the polymer. Compounds capable of such quick calcium removal include sodium citrate and EDTA.

Figure 4.6 presents the flow profile in the main microchannel when the microvalve was generated and when it was erased with EDTA. A $CaCl_2$ solution was inserted into the prototype 2 at 500 nL min^{-1}. Meanwhile, the alginate was inserted as a fast pulse perpendicularly. At the T-junction polymerisation of the microvalve takes place, blocking the channel and producing a decrease in the flow to virtually 0 µL min^{-1} (Figure 4.6 C). After this, the addition of EDTA (500 nL min^{-1}), coming from the channel set on top of the main channel (V-shape) removes the calcium ions from the alginate polymer erasing the microvalve from the main microchannel and increasing the flow rate (Figure 4.6 D). It is worth to mention here that for this microfluidic configuration (prototype 2) it is not necessary to heat the microfluidic microvalve since the EDTA channel sits on top of the main channel. Both channels are connected through a small orifice that gets blocked when the microvalve forms.

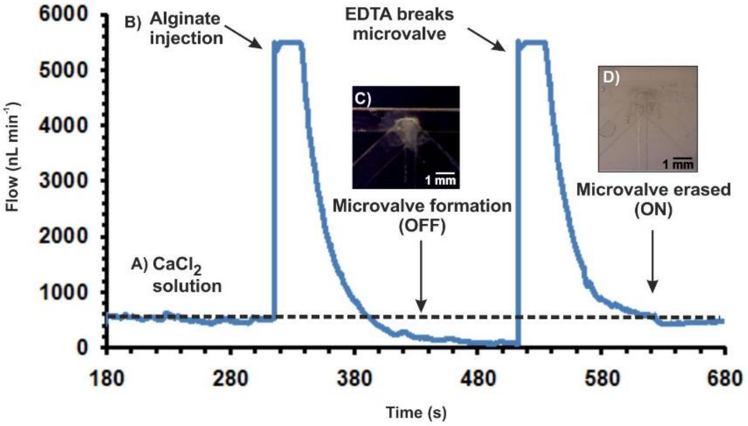

Figure 4.6: Flow profile in the main microchannel of the microfluidic device during alginate microvalve generation and removal by EDTA (flow sensor placed at the outlet of the microfluidic device). A) $CaCl_2$ solution injection at 500 nL min^{-1}. B) Sodium alginate solution pulse injection. C) Generated calcium alginate microvalve (OFF). D) EDTA solution injection and removal of the microvalve from the main microchannel (ON).

It was found out that 60 ± 5 µL (n = 3) of EDTA are sufficient to erase completely the calcium alginate microvalve from the channel and regenerate the main microfluidic microchannel for subsequent operations. The time needed to remove the valve was approx. 120 s (depending on the size of the generated microvalve), being a fast process that could be comparable to the actuation mechanism observed by others when using conventional hydrogel microvalves in microfluidic devices, *e.g.* photoswitchable (60 s)[27] or thermoresponsive (120 s)[23], to open.

A way of controlling the dimensions of the calcium alginate microvalves will be desired in order to obtain a more robust and functional device, which could be employed for the fabrication of microfluidic systems for environmental analysis at the point of need. It is believed that the results presented in this Chapter open the use of calcium alginate material as microvalves for many applications, such as POC devices, which need biocompatible and biodegradable components.

4.4 Conclusions

This Chapter demonstrates the potential of alginate polymers to be used as building block materials for the *in-situ* fabrication of microvalves in microfluidic devices with an ON/OFF actuation capability. Alginate has efficiently proven to act as actionable microvalve at mild temperatures allowing for flow control due to its syneresis effect. Moreover, by carefully adjusting the microfluidic channel configuration, alginate microvalves can be easily erased with an EDTA solution, ensuring the reusability of the whole device.

Alginate is biodegradable; therefore, it is attractive for microfluidic applications related to environmental, health and food industry. Moreover, these calcium alginate microvalves are low cost to produce in terms of materials, and the *in-situ* fabrication and removal open the possibility of creating large arrays of microvalves in complex microfluidic structures.

4.5 References

1 S. Haeberle and R. Zengerle, *Lab Chip,* 2007, 7, 1094-1110.
2 C. A. Baker, C. T. Duong, A. Grimley and M. G. Roper, *Bioanalysis,* 2009, 1, 967-975.
3 A. Fonseca, I. M. Raimundo Jr, J. J. Rohwedder, R. S. Lima and M. C. Araujo, *Anal. Bioanal. Chem.,* 2010, 396, 715-723.
4 A. Milani, P. J. Statham, M. C. Mowlem and D. P. Connelly, *Talanta,* 2015, 136, 15-22.
5 G. Pasirayi, S. M. Scott, M. Islam, L. O'Hare, S. Bateson and Z. Ali, *Talanta,* 2014, 129, 491-498.
6 M. Rothbauer, D. Wartmann, V. Charwat and P. Ertl, *Biotechnol. Adv.,* 2015, 33, 948-961.
7 W. Al-Faqheri, F. Ibrahim, T. H. G. Thio, M. M. Aeinehvand, H. Arof and M. Madou, *Sens. Actuators A, Phys.,* 2015, 222, 245-254.
8 S. Argentiere, G. Gigli, M. Mortato and Irini Gerges and Blasi, L., in *Advances in Microfluidics, Ed.* R. T. Kelly, InTech, 2012, pp.127-154.
9 E. M. Ahmed, *J. Adv. Res.,* 2015, 6, 105-121.
10 D. T. Eddington and D. J. Beebe, *Adv. Drug Deliv. Rev.,* 2004, 56, 199-210.
11 A. Blandino, M. Macías and D. Cantero, *J. Biosci. Bioeng.,* 1999, 88, 686-689.
12 J. Sun and H. Tan, *Materials,* 2013, 6, 1285-1309.
13 K. Y. Lee and D. J. Mooney, *Prog. Polym. Sci.,* 2012, 37, 106-126.
14 A. Dalmoro, A. A. Barba, G. Lamberti, M. Grassi and M. d'Amore, *Adv. Polym. Technol.,* 2012, 31, 219-230.
15 Y. Yajima, M. Yamada, E. Yamada, M. Iwase and M. Seki, *Biomicrofluid.,* 2014, 8, 024115.
16 E. Ghafar-Zadeh, *Sensors,* 2015, 15, 3236-3261.
17 V. Zamora-Mora, D. Velasco, R. Hernández, C. Mijangos and E. Kumacheva, *Carbohydr. Polym.,* 2014, 111, 348-355.
18 F. Benito-Lopez, M. Antoñana-Díez, V. F. Curto, D. Diamond and V. Castro-López, *Lab Chip,* 2014, 14, 3530-3538.
19 C. L. Cassano, A. J. Simon, W. Liu, C. Fredrickson and Z. H. Fan, *Lab Chip,* 2015, 15, 62-66.
20 S. K. Bajpai and S. Sharma, *React. Funct. Polym.,* 2004, 59, 129-140.
21 C. W. McCleary, D. A. Rees, J. W. B. Samuel and I. W. Steele, *Carbohydr. Res.,* 1967, 5, 492-495.
22 Y. Fang, S. Al-Assaf, G. O. Phillips, K. Nishinari, T. Funami, P. A. Williams and A. Li, *J. Phys. Chem. B,* 2007, 111, 2456-2462.
23 I. Fernández Farrés and I. T. Norton, *Food Hydrocoll.,* 2014, 40, 76-84.
24 H. Kim, *Kor. J. Chem. Engin.,* 1990, 7, 1-6.
25 G. I. Olivas and G. V. Barbosa-Cánovas, *LWT - Food Sci. Tech.,* 2008, 41, 359-366.
26 M. Kobaslija and D. T. McQuade, *Biomacromolecules,* 2006, 7, 2357-2361.
27 M. Czugala, D. Maher, F. Collins, R. Burger, F. Hopfgartner, Y. Yang, J. Zhaou, J. Ducrée, A. Smeaton, K. J. Fraser, F. Benito-Lopez and D. Diamond, *RSC Adv.,* 2013, 3, 15928-15938.

5

Photo-responsive Actuators into Lab-on-a-Disc Devices*

This Chapter describes the design, fabrication and the performance of a reusable ionogel-based photo-actuator *in-situ* photopolymerised into a lab-on-a-disc microfluidic device, for flow control. The ionogel provides an effective barrier to liquids during storage of reagents and spinning of the disc. A simple LED (white light) triggers actuation of the ionogel for selective and precise channel opening at a desired location and time. The mechanism of actuation is reversible, and regeneration of the actuator is possible with an acid chloride solution. In order to achieve regeneration, the Lab-on-a-Disc device was designed with a microchannel connected perpendicularly to the bottom of the ionogel actuator (regeneration channel). This configuration allows the acid solution to reach the actuator, independently from the main channel, which initiates ionogel swelling and main channel closure and thereby enables reusability of the whole device.

*****Parts of this Chapter have been published in J. Saez; T. Glennon; M. Czuagala; A. Tudor; J. Ducree; D. Diamond; L. Florea; F. Benito-Lopez, Reusable ionogel-based photo-actuators in a lab-on-a-disc, *Sens. Actuators B: Chem.*, 2017. DOI:10.1016/j.snb.2017.11.016.

5.1 Introduction

Centrifugal microfluidics or 'Lab-on-a-Disc' (LoaD) has many advantages over other microfluidic approaches as described in Chapter 2. Briefly, these include (i) minimal amount of fluidic manipulation components since liquids are moved by centrifugal forces, (ii) the absence of bubbles after efficient spinning, (iii) minimal dead volume and (iv) the possibility of performing complex assays with no external energy input, facilitating their use in resource-limited[1, 2] situations.

The use of LoaD technology enables the fabrication of simple, stand-alone instrumentation with a simple spindle motor, without the need of complicated and expensive peripherals such as tubing connections and pumps. Moreover, reagents can be pre-stored and used on demand[3].

Among all the microfluidic operations that can be implemented in a disc, valving is one of the most important, as described in Chapter 4 for conventional microfluidic devices, since it allows flow control in the microchannel. In LoaDs[3-8] closed passive valves are the most extensively investigated since they are easily actuated by controlling the spinning speed of the disc. The inherent geometry, position and physical properties of the valve in the microfluidic channel govern their open or closed state. In general, passive valves are easily fabricated, following conventional microfabrication methods; however, to accurately control their actuation remains difficult, especially when attempting to control individual valves in devices that have multiple valves. Moreover, any microfabrication inaccuracy adversely affects the flow during spinning and so the performance of the valve.

In order to achieve simple and robust flow control, many kinds of active valves in LoaDs have been recently investigated[1]. These include valves based on wax[9, 10], dissolvable films[11, 12] and photoswitchable polymer actuators. Active valves are triggered by external sources and can be switched between an open and closed state during the spinning process[1]. However, these valves are difficult to implement into a centrifugal microfluidic device, since they are often manually integrated, generating elevated fabrication costs and high actuation inaccuracy.

Stimuli-responsive materials can present switchable chemical properties if an external stimulus (light, temperature, chemical, magnetic field, etc.) is applied. The stimuli responsiveness of these materials is based on the existence of two metastable energy states associated with two structural forms that possess distinctly different energy minima[13]. It is described that the mechanisms of switching of these materials are achieved when a relatively large number of molecules populating these energy states can be externally perturbed with a stimulus (*e.g.* light) and so switched from one dominant state to the other. It is clear that the functional groups present in the gel network are the responsible for the type of actuation of the gel, *eg.* magnetic, thermal, optical, mechanical, or chemical (which is the case of the valves presented in Chapter 4).

Stimuli-responsive gels such as the poly(*N*-isopropylacrylamide), p(NIPAAm), have been deeply investigated as thermoactuators[14-17] as was described in Chapter 2. The swelling degree of p(NIPAAm) is very high at low temperatures due to high water uptake and this state changes abruptly upon crossing its lower critical solution temperature (LCST), leading to contraction to a compact globular form due to the release of water[18]. A similar behaviour can be achieved using light as a non-contact and non-invasive stimulus. Light irradiation represents one of the most attractive actuation mechanisms which is exhibited when p(NIPAAm) gels are functionalised with spirobenzopyran moieties (SP)[19]. Spirobenzopyrans can be switched upon light irradiation between two states which are thermodynamically stable[20]. These hybrid materials, referred as p(SPNIPAAm) from now on, have two stimuli-responsive functions: first, thermoresponsive p(NIPAAm) gels are swollen below the LCST and, secondly, the photoresponsive SP molecule, when open to the charged merocyanine ($MC-H^+$) isomer under UV-irradiation, is able to convert to the uncharged SP isomer under light irradiation. The switching mechanism, from $MC-H^+$ to SP isomer is reversible and triggers conformational rearrangements in the bulk p(NIPAAm) gel, changing it from a more hydrophilic to a hydrophobic nature, which in turn induces water loss and contraction of the gel[21].

Traditionally, organic solvents have been employed for the synthesis of p(SPNIPAAm) gels. However, more recently, the incorporation of ionic liquids (ILs) as solvents within the gel polymer matrix is generating a lot of attention, as this new class of materials, known as ionogels, can exhibit very attractive characteristics, as they can retain the physical properties of both the polymer gel and the physically entrapped IL. Recent reviews have examined the interaction and mobility of the IL within the polymer network as well as the application of ionogels as functional materials as sensors and actuators[22]. Recently, ionogels were reported to exhibit improved water uptake/release behaviours and better mechanical and viscoelastic properties compared to their equivalent hydrogels[23]. Photo-actuating actuators based on an IL incorporated within the p(SPNIPAAm) polymer matrix have been successfully developed. It was demonstrated that, by using different IL within the gels, the kinetics of the actuation could be controlled through IL mediation (rate of protonation/deprotonation), and through the movement of counter ions and solvent (water) in the ionogel matrix. As a consequence, ionogels containing different ILs were found to respond at different times when exposed to a common light source in microfluidic devices[24].

Therefore, photo-switchable actuators are able to achieve non-contact, spatially independent and parallel fluid manipulation together with low cost and easy implementation, which are requirements for the improvement of functionalities such as valving in LoaD microfluidic devices. In conventional microfluidic devices, these actuators have been investigated previously. For example, Coleman *et al.*[25] developed a photo-valve that can be operated in microfluidic devices as a flow controller. Czugala *et al.*[26] developed a photo-switchable actuator that is capable of storing reagents when in the closed state. After actuation with white light, it opens itself allowing the reagent to flow into the main channel and react with the analyte of interest. However, to our knowledge, this type of actuating mechanism has so far not been investigated in centrifugal platforms.

This Chapter describes the design, fabrication, and performance of a reusable ionogel-based actuator *in-situ* photopolymerised into a LoaD device to provide flow control functions. The ionogel provides a barrier to liquids during storage and spinning of the disc up to 600 rpm. A white light LED, as a source of irradiation, allows the selective opening of the ionogel photo-actuator at the desired time. The regeneration of the actuator, *i.e.,* closing, is possible with an acid chloride solution, which contacts the actuator via a microchannel connected to the bottom of the ionogel actuator, fabricated perpendicularly to the main channel to prevent ingress by the acid into the main fluidic channel.

5.2 Experimental

5.2.1 Materials and Equipment

For the synthesis of the ionogels *N*-isopropylacrylamide, (*N*,*N*´-methylene-bis(acrylamide) (MBIS), the photo-initiator 2,2-dimethoxy-2-phenylacetophenone (DMPA) and the ionic liquid trihexyltetradecylphosphonium dicyanamide [$P_{6,6,6,14}$][dca], were purchased from Sigma Aldrich (St Louis, MO, USA). 1´,3´,3´-trimethyl-6-acrylate(2H-1-benzopyran2,2´-indoline) was synthesised by us following the previously reported protocol from Szilagyi [27]. 1 N HCl was purchased from Merck Millipore (Darmstadt, Germany).

The purification of the IL was carried out as follows: 10 mL of the IL decolourised by re-dissolution in 30 mL of acetone was followed by treatment with activated charcoal (Darco-G60, Aldrich®) at 40 °C overnight. The carbon was removed by filtration through alumina (acidic, Brockmann I, Aldrich®) and the solvent removed under vacuum at 60 °C for 24 h at 0.1 Torr[28].

The UV light source used for photo-polymerisation was a BONDwand UV-365 nm obtained from NEI Corporation (Somerset, NJ, USA).

The fabrication of the microfluidic devices was carried out using a laser ablation system Epilog Zing 16 (Golden, CO, USA). 1 mm thickness poly(methyl)methacrylate (PMMA) slides were purchased from Goodfellow (Huntingdon, UK). ArCare® pressure sensitive adhesive (PSA) of 86 µm double side roll was generously provided by Adhesive Research (Limerick, Ireland) and cut using a Graphtec© CE5000-40 Craft Robo Pro (Tokyo, Japan) cutter. A thermal laminator roller ChemInstruments HL-101 (Fairfield, OH, USA) was used for PMMA and PSA layers bonding.

A homemade centrifugal instrument that incorporates a LED was used for studying the performance of the photo-actuators, as shown in Figure 5.1. A Dolan-Jenner LMI-6000 fiber optic illuminator from Edmund Optics (York, UK) was used for the actuation of the ionogels. For the visual monitoring of the liquid flow, a red food dye from McCormick (Sabadell, Spain) was used.

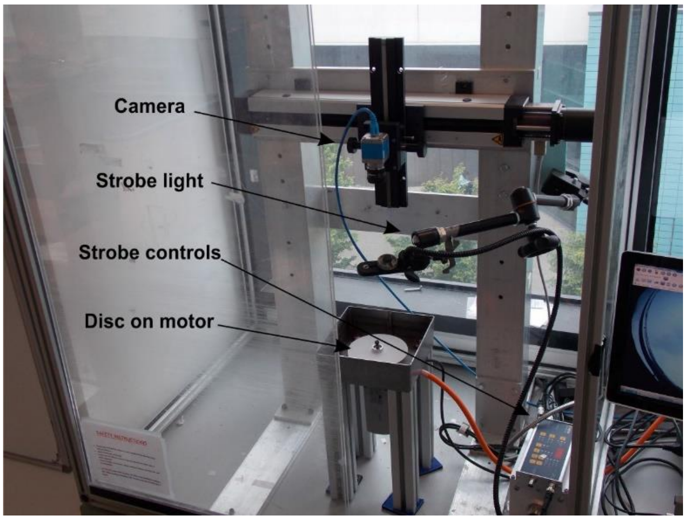

Figure 5.1: Picture of the spin stand platform showing its different parts: camera, strobe light, strobe controls and disc on the motor.

Pictures were taken with an Aigo Nexus GE5 (Chippenham, UK) digital camera and analysed using its software. 3D microscope pictures were taken by using a VHX-2000 3D Keyence 3D microscope (El Segundo, CA, USA) and analysed using the 3D microscope´s software.

5.2.2 p(SPNIPAAm) Preparation and Integration as Actuator into the LoaD

The ionogel actuator (Figure 5.2 A) was synthesised using the protocol described by Czugala *et al.*[28] Briefly, 85 mg of NIPAAm, 6.1 mg of MBIS and 4.12 mg of 1´, 3´,3´-trimethyl-6-acrylate(2H-1-benzopyran2,2´-indoline), together with 2.68 mg of the photo-initiator DMPA were dissolved in 285.95 mg of [$P_{6,6,6,14}$][dca]. The solution (3 µL) was photopolymerised in the actuator disc, filling the entire volume of the reservoir, through a mask using a UV-365 nm LED placed at 8 cm from the solution (UV intensity 10 mW cm^{-2}) for 25 min. Upon completion of polymerisation, the resulting ionogel actuators were rinsed with deionised water to remove any un-polymerised monomers and excess of the ionic liquid. The ionogel actuators were dried at room temperature for 24 h. After assembly of the different layers of the LoaD, a 10^{-3} M HCl aqueous solution was used to initially swell the actuators using the perpendicular channel, as depicted in Figure 5.2 B. The actuators were exposed to the acidic solution for 2 h at room temperature to ensure they were swollen and the main channel closed. Furthermore, the ionogel actuator continuously blocked the perpendicular side channel, preventing fluidic transfer between the main channel and the perpendicular channel. After 2 h, the ionogel was irradiated with white light, which caused contraction of the gel, releasing H^+ and water molecules, thus, opening the main channel to fluid movement (but maintaining the closed status of the perpendicular channel).

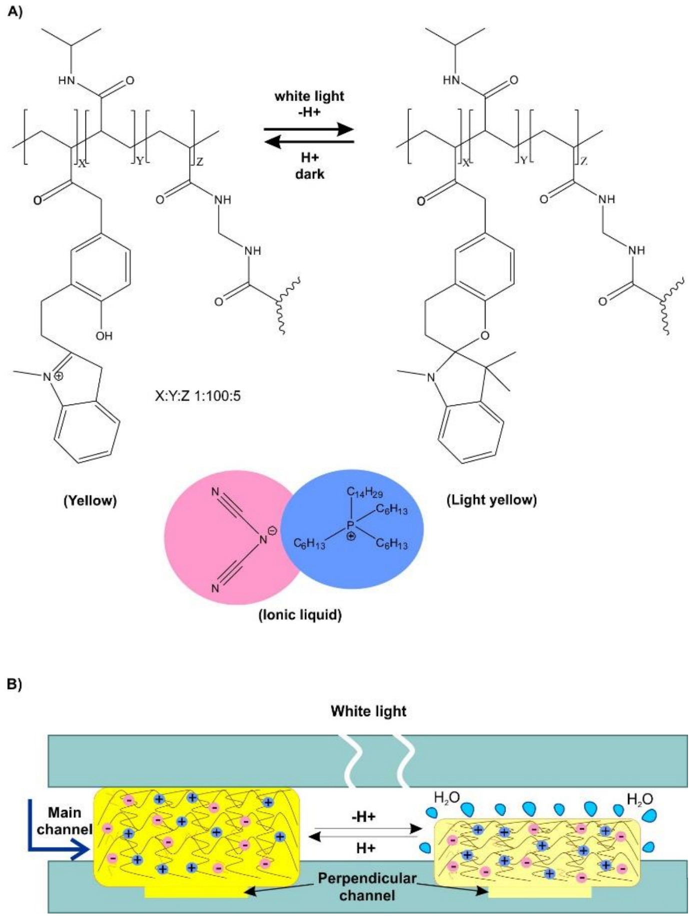

Figure 5.2: (A-top) Chemical structure of the crosslinked p(NIPAAm) gel functionalised with the SP, protonated (left) and deprotonated (right), and (A-bottom) chemical structure of the trihexyltetradecylphosphonium dicyanamide ionic liquid; both components form the ionogel. (B) Schematic illustration of the reversible swollen (channel closed)/contracted (channel open) polymer network due to movement of protons (H^+) and water from the ionogel (not in scale)[28].

5.2.3 LoaD Fabrication and Assembly

The device was created in a disc format, consisting of a multi-layer structure made of PMMA and PSA sheets aligned and bonded together in a laminator under controlled temperature. PMMA sheets were cut using a CO_2 laser while PSA sheets were cut by using xurography[29], both of which are rapid prototyping techniques. Figure 5.3 shows the structure of the LoaD device in terms of the following layers:

1) The bottom PMMA layer that seals the disc and contains the perpendicular channel and the reservoir in which the actuator is placed.

2) This lower PSA layer contains the channels (500 µm width) that connect the chambers (sample loading, actuation, and bottom chamber) and bonds the bottom and middle PMMA layers.
3) A middle PMMA layer, which contains all chambers (including a chamber for actuator visualisation).
4) An upper PSA layer that allows visual observation of the channels in the layers below and bonds top and middle PMMA layers.
5) A PMMA top layer, which contains the vents and loading holes.

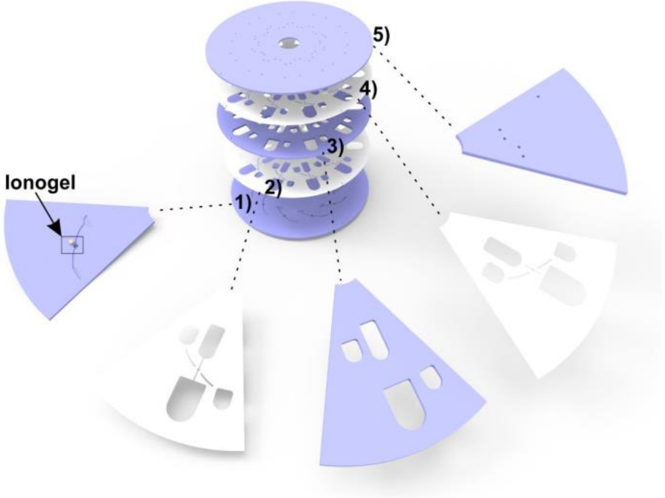

Figure 5.3: Assembly of the multi-layer LoaD device. 1) PMMA layer that seals the disc and contains the perpendicular channel and the reservoir in which the actuator is photopolymerised. 2) PSA layer containing the channels. 3) PMMA layer containing the chambers. 4) PSA layer that seals layers 5 and 3 and ensures channels visualisation. 5) PMMA layer containing the loading holes.

5.2.4 Characterisation of the Actuator inside the LoaD

Studies of the swelling and shrinking kinetics of the actuator in the LoaD device were carried out as follows. A cross-section of the actuator and reservoir were cut with a CO_2 laser and pictures of swelling (with deionised water) and shrinking (by actuation with the white light LED, placed 1 cm from the actuator) behaviour were taken for a period of 25 min. The pictures were analysed via the camera software of the Aigo Nexus GE5 digital microscope and the swelling and the shrinking were measured with a ruler. In addition, the channel dimensions for efficient actuator function were optimised during laser cutting by changing the power and the speed between 20-60 % and 50-90 %, respectively. In general, higher powers and lower speeds generate deeper channels. Following this, they were filled with the p(SPNIPAAm) solution and the actuator gel structure photopolymerised as described above.

5.2.5 Actuator Swelling and Shrinking Kinetics

The percentage variation in actuator height; *%H*, is defined as:

$$\%H = \frac{H_t - H_0}{H_0} \times 100 \tag{5.1}$$

where H_t is the height of the ionogel-based actuator inside the microfluidic device at time *t* and H_0 is the height before immersion in the 10^{-3} M HCl solution. The swelling kinetics was investigated by placing the ionogel-based actuator samples in a dark environment in 10^{-3} M HCl aqueous solution and taking digital images every 20 min for 140 min. A single exponentially decaying growth model (Equation 5.2)[30] was used to estimate the swelling rate constants, following the same protocol described by Czugala *et al.*[20]:

$$\%H = a \cdot (1 - e^{-k_{sw} \cdot t}) + b \tag{5.2}$$

where *%H* is the percentage swelling, *a* is scaling factor, k_{sw} is the first order rate constant (s^{-1}), *b* is the baseline offset and *t* is time (s).

The shrinking kinetics of the ionogel-based actuator were evaluated by irradiating with white light for 25 min. Pictures were taken with the microscope after 1, 3, 5, 10, 15 20 and 25 min of exposure. The shrinking rate constants were estimated using the following exponential decay model (Equation 5.3):

$$\%H = a \cdot e^{-k_{sh} \cdot t} + b \tag{5.3}$$

where *%H* is the percentage of swelling, calculated in the same manner described by Equation 5.1, *a* is scaling factor, k_{sh} is the first order rate constant (s^{-1}), *b* is the baseline offset and *t* is time (s).

All experiments were performed at 23 °C. The PMMA with the ionogel-based actuators was positioned perpendicularly to the microscope to enable the height of the actuators to be accurately measured. The PMMA was cut with a CO_2 laser ablation system as close as possible to the ionogel-based actuator to provide a sharp focus for precise measurements.

5.3 Results and Discussion

5.3.1 Optimisation of LoaD Fabrication

In order to achieve effective fluid control, the photo-induced contraction of the ionogel must create an open channel after white light actuation. To investigate this, 1 mm diameter cylindrical reservoirs with depths between 200 µm and 500 µm were fabricated in the bottom layer of the LoaD device by applying different speeds and powers with the CO_2 laser, respectively, and then filled with the ionogel solution as detailed in Table 5.1 (see also Figure 5.4). The actuator was then photopolymerised with UV light as described in the experimental section and 3D microscope pictures were taken. After several fabrication iterations, a speed of 60 % and a power of 60 % were selected as the fabrication parameters for the CO_2 laser. Those parameters produced an appropriate channel depth (~ 514 µm) and actuator reservoir in the fluidic disc that showed good fluidic behaviour (*i.e*. effective channel opening and closing).

Table 5.1: Channel depths (µm) for different speeds and power (%).

Channel No.	Speed (%)	Power (%)	Channel depth (µm)
1	50	20	226.6
2	50	30	302.4
3	50	40	384.3
4	50	60	424.1
5	60	60	514.3
6	70	60	389.8
7	80	60	328.4
8	90	60	352.9

Figure 5.4: Evaluation of different depths and speeds (%) using the CO_2 ablation laser system. The ionogels were polymerised in the reservoirs.

5.3.2 Characterisation of the Actuators Swelling and Shrinking Kinetics

During storage, the swollen photoswitchable actuators provide effective liquid barriers as demonstrated previously by Czugala *et al.*[28] Therefore, the volume of the actuators in the different reservoirs was optimised for the LoaD device. Different volumes of the ionogel solution were photopolymerised *in-situ* within the microchannel. 3 µL of ionogel solution inside the reservoir area were found to produce structures that gave efficient actuator behaviour. After polymerisation, the ionogel actuators reached a height of 254 ± 46 µm (n = 4) after swelling for 80 min in an HCl 10^{-3} M solution, exhibiting an increase of 24 % in height calculated with Equation 5.1 (see Figure 5.5 A). Moreover, analysis of the height during swelling showed a linear increase occurring during the first 15 min (Figure 5.5 A, inset). This means that during the swelling process water diffusion is very fast until the external ionogel boundary layer in contact with the external solution is saturated/fully swollen). Thereafter, a much slower swelling process occurs from the boundary region towards the bulk, which is continuous over a much longer period of time[31].

The swollen p(SPNIPAAm) ionogel actuators are yellow colour due to the presence of the protonated spirobenzopyran moiety (MC-H^+). After irradiation with white light, isomerisation to the closed-ring form (SP) was induced and the ionogel becomes colourless. This is accompanied by a rapid water loss and contraction of the p(SPNIPAAm) ionogel actuator. It was found that the ionogel typically contracts by 40 ± 1 % (n = 3) of its initial swollen state after white light irradiation for about 5 min (Figure 5.5 B). A stronger white light is required for shrinking of the ionogel-based actuator compared to those used by Czugala *et al*.[21] (Aigo Digital Microscope GE-5) and Benito-Lopez *et al*.[32] (LEDs), and despite this, the dehydration of the actuator and subsequent shrinkage is relatively slow, requiring 15 min to reach 50 ± 3 % (n = 3) shrinkage from its initial swollen state. However, when the material is incorporated within microfluidic devices as an actuator, a smaller shrinkage percentage of ~ 30 ± 3 % (n = 3) in 3 min is enough to open the actuator and, thus, the channel (Figure 5.5 B).

First-order kinetic models were fitted using the Origin software (OriginLab, Northampton, MA, USA) to the experimental data and the rate constants of the swelling process (k_{sw}) were estimated (Table 5.2) using Equation.5.2. The swelling rate constant k_{sw} value obtained was 5.7 ± 0.7 10^{-4} s^{-1} (n = 3). The kinetics of the shrinking behaviour of the ionogel-based actuators was followed for 25 min using white light irradiation. The rate constants of the shrinking process k_{sh} were estimated (Table 5.3) in a similar way using Equation 5.3 yielding a value of 3.4 ± 0.4 10^{-3} s^{-1} (n = 3). Czugala *et al.*[21] reported the swelling and shrinking kinetics of 400 µm discs made of the same p(SPNIPAAm) ionogels obtaining higher values for the swelling and shrinking constants of k_{sw} = 4.5 ± 0.3 10^{-2} s^{-1} and k_{sh} = 8.3 ± 0.9 10^{-2} s^{-1}, respectively. The swelling kinetics of this type of materials are normally dominated by diffusion-limited transport of water through the ionogel matrix and is generally related to the energy driving the process and to the surface area to volume ratio (SA/V)[21]. Therefore, smaller ionogels should improve the swelling process since the rate of diffusion is inversely proportional to the first power dimension of the ionogel. The swelling behaviour of the ionogel in the LoaD device is, as demonstrated by others before[31], determined by the balance between the expanding force induced by the osmotic pressure of polymer solvation and the restoring force of the chain segments between crosslinks. Moreover, the PMMA reservoir restricts the movement of the actuator, and therefore the swelling occurs anisotropically from the bottom surface of the LoaD towards the main channel in the *z-axis* direction. In the LoaD platform, the ionogels dimensions are bigger, 1 mm *versus* 0.4 mm from Czugala's findings, and the surface area to volume ratio is smaller, due to the ionogel constriction inside the microfluidic reservoir and, therefore, it is not surprising that the actuation kinetics are slower for the LoaD actuators.

Table 5.3: Experimental swelling rate constants obtained by curve fit adjustment to Equation 5.2 provided by the Origin software.

Swelling Parameters

A		K_{sw}		B	
Value	Standard Error	Value (10^{-4} s^{-1})	Standard Error (10^{-5} s^{-1})	Value	Standard Error
14.8	1.1	5.7	6.6	9.6	1.0
11.9	1.1	5.7	6.6	11.3	0.9
15.2	1.1	5.7	6.6	10.6	1.0
14.7	1.1	5.7	6.6	8.9	0.9

Table 5.4: Experimental shrinking rate constants obtained by curve fit adjustment to Equation 5.3 provided by the Origin software.

Shrinking Parameters

A		K_{sh}		B	
Value	Standard Error	Value (10^{-3} s^{-1})	Standard Error (10^{-4} s^{-1})	Value	Standard Error
48.5	3.0	3.4	0.4	6.9	2.8
35.5	2.9	3.4	0.4	14.9	2.5
37.8	2.9	3.4	0.4	17.6	2.6

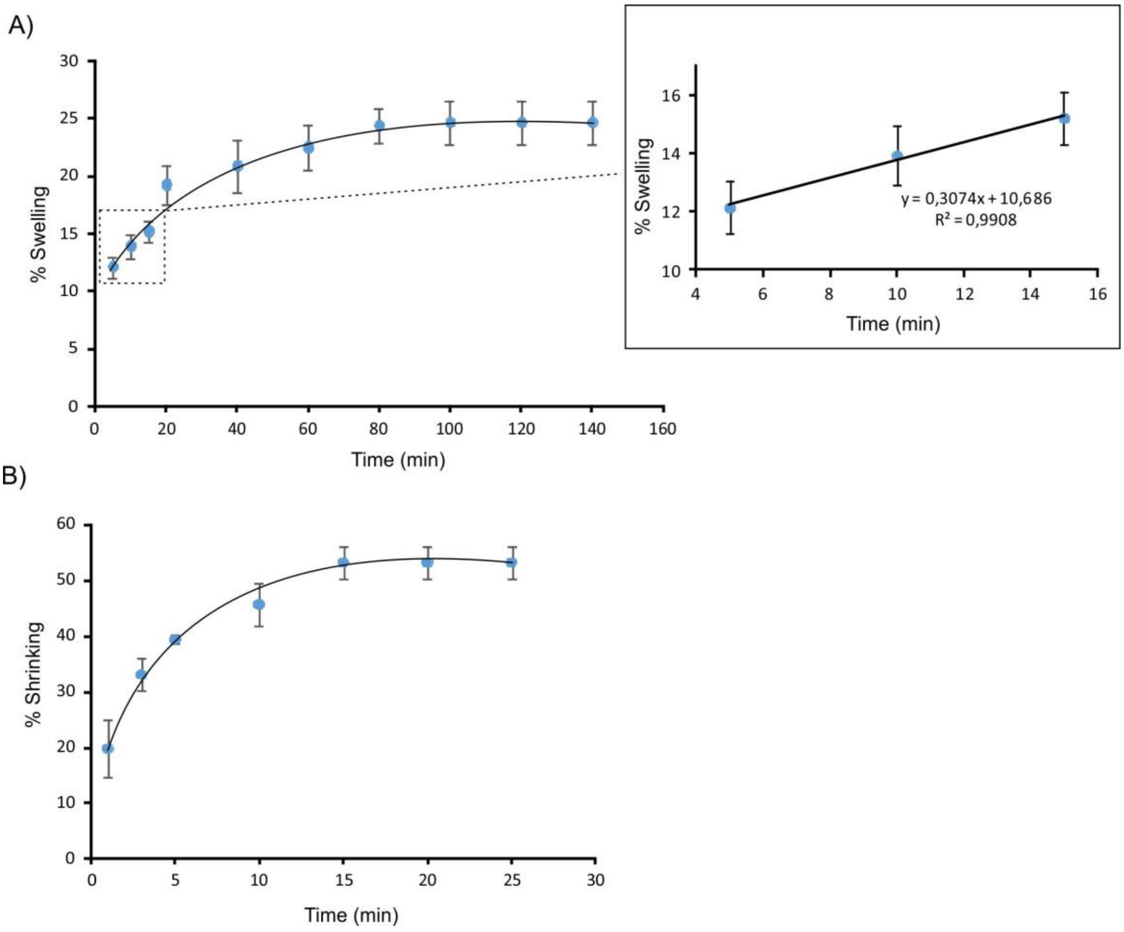

Figure 5.5: Kinetic models (continuous lines) obtained using the Origin software and adjusting the kinetic constants to be the same in all the experimental data series. A) Increment of the % swelling (n = 4) of the ionogel actuators inside the LoaD device *versus* time. The inside picture shows the linear tendency of the % swelling *versus* time at the beginning of the swelling process. B) Increment of the % shrinkage (n = 3) of the ionogel actuators inside LoaD device *versus* time. The actuator behaviour was investigated in layer 4 of the LoaD device.

Figure 5.6 A shows the volume phase transition of the actuators induced by water intake and subsequent white light irradiation over time. It can be clearly observed that the ionogel actuators expanded enough to block the main channel and contracted enough under white light irradiation to open it. Figure 5.6 B shows 3D microscope pictures of the same dehydrated, expanded and contracted actuator represented in Figure 5.6 A. In the initial dehydrated state, the maximum heights of the ionogel actuator and the PMMA sheet are the same, ~ 230 µm. When hydrated, the observed maximum height is ~ 266 µm (in strong red; channel closed), decreasing to ~ 190 µm when contracted (inside Figure 5.6 B, yellow colour; channel open).

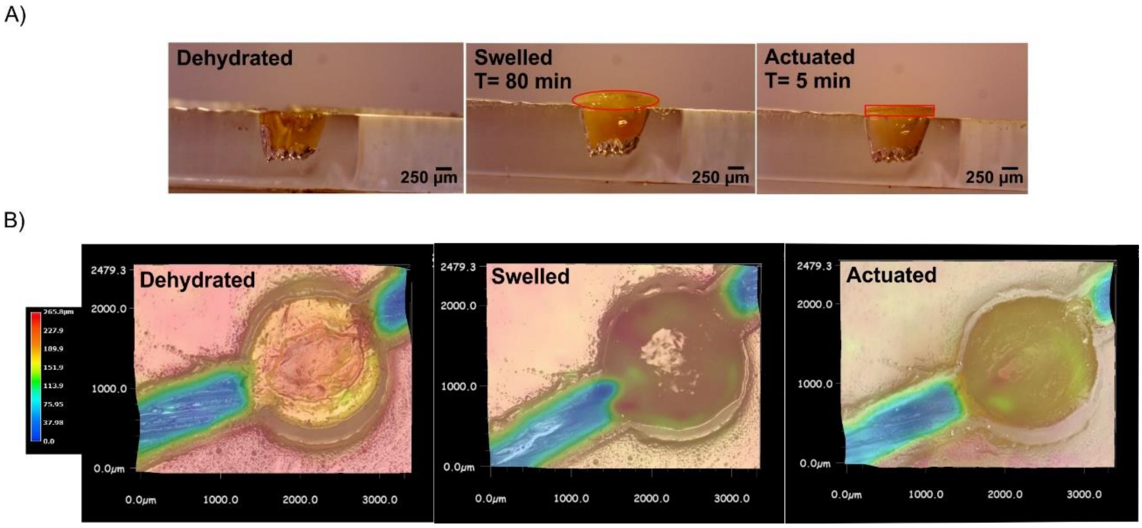

Figure 5.6: A) Set of pictures showing the initial dehydrated (left), hydrated (centre, closed) and contracted (right, open) states of the ionogel actuator inside the LoaD device (a red highlight has been added to the pictures to show the degree of swelling and shrinking of the ionogel). B) Set of 3D microscope pictures showing the initial dehydrated state followed by the hydrated (closed) and contracted (open) states with colour-matched heights of the ionogel actuator inside the LoaD device over time.

5.3.3 Regeneration of the Actuator inside the LoaD

The p(SPNIPAAm) ionogel based actuators require exposure to an acidic solution (pH = 3) in order to induce swelling, whereas the shrinking mechanism results in the release of protons into the external solution from the ionogel[13]. The actuator is first soaked in an HCl 10^{-3} M aqueous solution in order to induce spontaneous isomerisation of the protonated merocyanine ($MC-H^+$) form. Then, the ionogel swells and adopts a more hydrophilic conformation to the extent that the actuator blocks the main channel. Upon irradiation with white light, the $MC-H^+$ isomer reverts to the uncharged, colourless SP form, which triggers dehydration and shrinkage of the actuators (unblocking of the main channel). In order to evaluate the reusability of the actuator and, thus, its regeneration in the LoaD device, several cycles of re-swelling of the actuator with HCl solution and subsequent actuation with white light were carried out (see Figure 5.7). It was found that the actuator function was maintained for up to 3 cycles of regeneration/actuation after which degradation of the ionogel actuator was observed (see cycle 4 in Figure 5.7). In order to evaluate the percentage deviation of the performance of the actuator after several regeneration/actuation cycles, the hysteresis of the ionogel-based actuator in cycles 2, 3 and 4 was calculated. It was found that, after cycle 3, a hysteresis of 80 % for regeneration (swelling) and 77 % for photo-induced contraction occurred, which was insufficient for fluidic control (actuator failure). A smaller degree of hysteresis was found for cycles from 1 to 3 (30 % higher). In this regard, Delaney *et al.*[33] recently suggested that the first few cycles of actuation could be anomalous, due to the settling of the system, as this appears to be followed by a longer period of reproducibility over multiple cycles. In our case, the hysteresis caused failure because the gel is too swollen, leading to permanent blockage of the channel. This effect can be reduced by creating the ionogel microactuator structure using photopolymerisation through a mask instead of actual drop casting protocol used in this study[33].

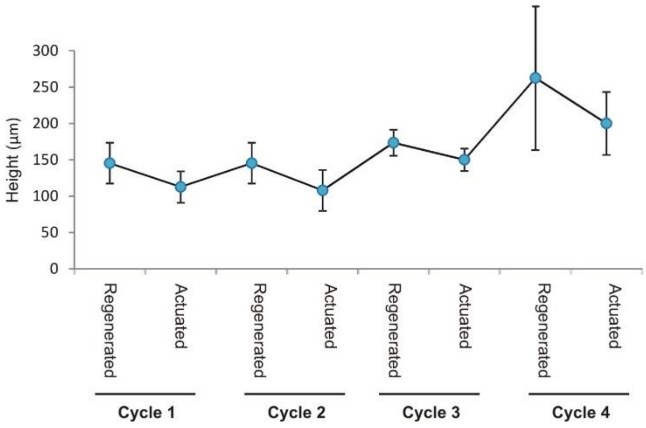

Figure 5.7: Regeneration cycles using an HCl 10^{-3} M (pH = 3) solution followed by actuation with white light of the ionogel actuators (n = 3).

5.3.4 Performance of the LoaD Actuator

A study of the performance of the ionogel-based actuator in the LoaD device was investigated. The microfluidic structure consisted of two chambers connected by a channel in which the ionogel-based actuator was placed. Another perpendicular channel passed to the actuator, from the reverse side of the main fluidic channel, to provide a source of acid to the ionogel for the re-swelling of the actuator after contraction under white light irradiation. The upper chamber was filled with a coloured dye solution for visualisation of the process (Figure 5.8 A). Disc rotation at 600 rpm moved the coloured solution towards the bottom of the chamber. The actuator at this stage blocks the main channel, preventing the sample from moving along the channel that connects both chambers. After this, white light irradiation was applied for 3 min in order to contract the ionogel and open the channel. The fluid now moves to the bottom chamber, emptying the upper chamber (Fig. 5.8 B). This mechanism can be repeated at least three times due to the perpendicular channel, which exposes the ionogel actuator to the acidic solution, by rotating the disc at 400 rpm (see Figure 5.8 C and D). This solution induces the re-swelling of the actuators after about 20 min to the extent that the channel is once more closed.

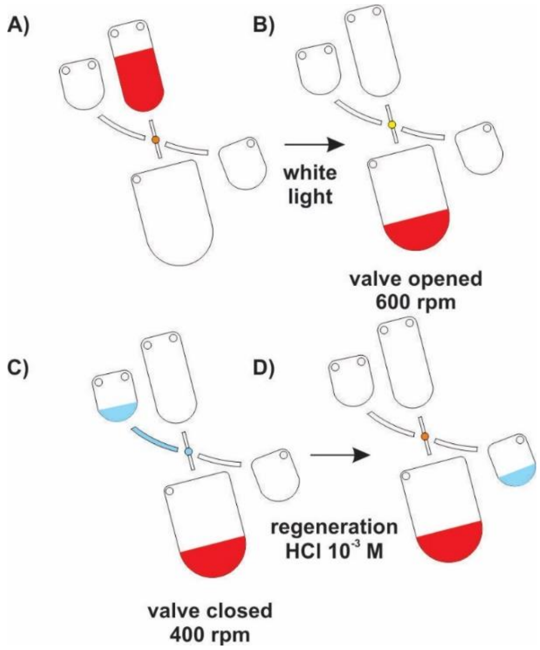

Figure 5.8: Scheme of actuator performance into one of the units. A) 40 µL of red dye are loaded. The disc is rotated at 600 rpm and the red dye solution moves to the bottom side of the upper chamber but cannot pass further due to the swollen (closed) actuator (orange dot in the channel). B) The ionogel-based actuator is exposed to white light for 3 min. The actuator opens (yellow dot) and the red dye solution passes from the upper to the lower chamber through the now open connecting channel. C) Spinning is stopped and 40 µL of HCl 10^{-3} M (blue) is loaded in the upper regeneration chamber. The LoaD is rotated at 400 rpm and the blue acidic solution passes from the upper to the lower regeneration chamber, causing re-swelling of the gel actuator (blue dot, 20 min for total re-swelling of the ionogel). The gel actuator is then ready for a repeat cycle (orange dot). Note that at all times, the gel prevents the transfer of the acid from the regeneration chambers into the main channel and chambers.

Figure 5.9 presents a set of pictures taken from the video 5.1 (http://www.sciencedirect.com/science/article/pii/S0925400517321378), which shows the performance of the ionogel actuator in the LoaD. The actuator was covered with an opaque tape to protect it from ambient light during device storage.

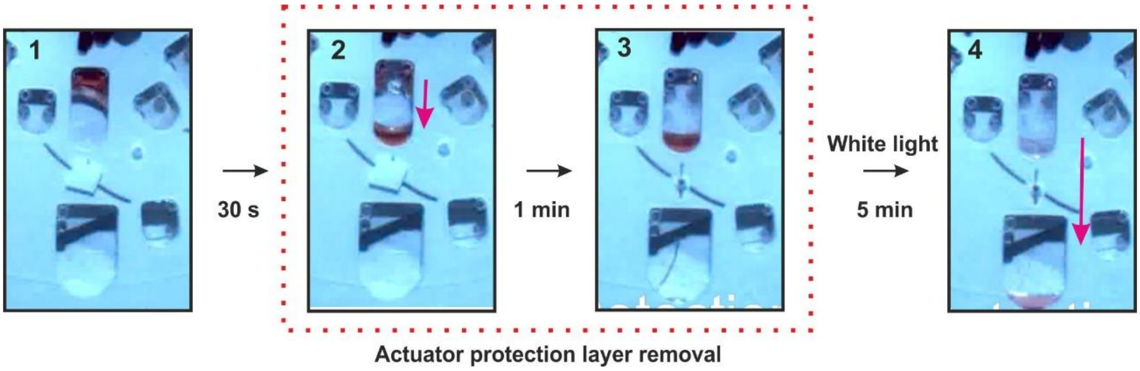

Figure 5.9: Set of pictures taken from a video (high-speed camera) during actuator performance at 600 rpm. 1) The coloured dye solution is loaded in the upper chamber and the actuator is hidden from the light with a PSA layer. 2) The disc spins at 600 rpm and the sample is placed in the bottom part of the upper chamber due to centrifugal forces. 3) The PSA layer is removed and 4) upon white light irradiation, the actuator shrinks and the sample passes from the upper to the bottom chamber.

The design and position of the perpendicular channel and chambers ensure that no acid solution accesses the main channel during the actuator regeneration-spinning step as the ionogel-based actuator acts as a physical barrier between the regeneration channel and the main channel at all times. However, the design of the regeneration channel ensures effective exposure to the acidic solution when required, leading to the re-swelling of the actuator, which can be initiated by applying a disc rotation speed of 400 rpm.

Finally, the burst threshold of the actuator was found to be between 750-800 rpm. Therefore, speeds below these values are able to provide a stable physical barrier for the LoaD device. Stronger sealing can be achieved by changing the chemistry of the ionogel using more hydrophobic ionic liquids and/or higher cross-linked gels. However, this will also affect the actuation response and swelling/shrinking kinetics of the gel, which needs to be considered during the fabrication of the LoaD device.

5.4 Conclusions

Through this chapter, a reusable ionogel-based photo-actuator has been presented. This actuator can be operated successfully within a microfluidic channel without complex actuator designs or reverting to single-use dissolvable/wax actuators. It was found out that the p(SPNIPAAm) ionogel-based actuator swelling and contraction rate constants inside the microfluidic device were $5.7 \pm 0.7\ 10^{-4}\ s^{-1}$ and $3.4 \pm 0.4\ 10^{-3}\ s^{-1}$, respectively. It has been shown that the ionogel-based actuator provides a reasonably well-defined degree of volume change (%*H*) and photoresponse time inside the microfluidic device. This could have important implications for the practical implementation of disc-based microfluidics, as it potentially opens the way towards the generation of lab-on-a-disc microfluidic systems in which the photonic actuation stimulus can be totally separated from the reagents, which is compatible with a freely spinning disc configuration. It also opens the possibility of multiple use valves, by re-swelling the p(SPNIPAAm) ionogel with an acidic solution in a perpendicular channel.

This configuration increases the toolbox of microfluidic components in LoaD devices and, therefore, the possibility of implementing ionogels in devices which are currently used in LoaD for environmental analysis such as the CMAS system developed by Czugala *et al.*[26] or the devices developed by Duffy *et al*.[34] and Nwankire *et al*.[12].

5.5 References

1 O. Strohmeier, M. Keller, F. Schwemmer, S. Zehnle, D. Mark, F. Von Stetten, R. Zengerle and N. Paust, *Chem. Soc. Rev.,* 2015, 44, 6187-6229.

2 M. Tang, G. Wang, S. Kong and H. Ho, *Micromachines,* 2016, 7, 1-29.

3 T. Kim, V. Sunkara, J. Park, C. Kim, H. Woo and Y. Cho, *Lab Chip,* 2016, 16, 3741-3749.

4 J. Xiang, Z. Cai, Y. Zhang and W. Wang, *Sens Actuators B, Chem.,* 2017, 243, 542-548.

5 R. Gorkin, C. E. Nwankire, J. Gaughran, X. Zhang, G. G. Donohoe, M. Rook, R. O'Kennedy and J. Ducrée, *Lab Chip,* 2012, 12, 2894-2902.

6 Z. Cai, J. Xiang, H. Chen and W. Wang, *Sens Actuators B, Chem.,* 2016, 228, 251-258.

7 S. Zehnle, F. Schwemmer, R. Bergmann, F. von Stetten, R. Zengerle and N. Paust, *Microfluid. Nanofluid.,* 2015, 19, 1259-1269.

8 O. Ymbern, P. Couceiro, M. Berenguel-Alonso, N. Sández and J. Alonso, *Int. Conf. Miniaturized Syst. Chem. Life Sci. , MicroTAS,* 2016, , 1055-1056.

9 M. Keller, A. Drzyzga, F. Schwemmer, R. Zengerle and F. Von Stetten, *International Conferenced for. Miniaturized Systems for Chemistry and Life Sciences,MICROTAS,* 2015, 1184-1186.

10 L. X. Kong, K. Parate, K. Abi-Samra and M. Madou, *Microfluid. Nanofluid.,* 2015, 18, 1031-1037.

11 D. J. Kinahan, S. M. Kearney, O. P. Faneuil, N. Dimov and J. Ducrée, *RSC Adv.,* 2015, 5, 1818-1826.

12 C. E. Nwankire, M. Czugala, R. Burger, K. J. Fraser, T. M. Connell, T. Glennon, B. E. Onwuliri, I. E. Nduaguibe, D. Diamond and J. Ducrée, *Biosens. Bioelectron.,* 2014, 56, 352-358.

13 R. Klajn, *Chem. Soc. Rev.,* 2014, 43, 148-184.

14 Y. Maeda, T. Higuchi and I. Ikeda, *Langmuir,* 2001, 17, 7535-7539.

15 H. G. Schild, *Prog Polym Sci (Oxford),* 1992, 17, 163-249.

16 C. Boutris, E. G. Chatzi and C. Kiparissides, *Polym.,* 1997, 38, 2567-2570.

17 X. Zhang, Y. Yang, T. Chung and K. Ma, *Langmuir,* 2001, 17, 6094-6099.

18 S. Sugiura, K. Sumaru, K. Ohi, K. Hiroki, T. Takagi and T. Kanamori, *Sens. Actuators A, Phys.,* 2007, 140, 176-184.

19 L. Florea, D. Diamond and F. Benito-Lopez, *Macromol. Mater. Engin.,* 2012, 297, 1148-1159.

20 S. Gallagher, L. Florea, K. J. Fraser and D. Diamond, *Int. J. Mol. Sci.,* 2014, 15, 5337-5349.

21 M. Czugala, C. O'Connell, C. Blin, P. Fischer, K. J. Fraser, F. Benito-Lopez and D. Diamond, *Sens. Actuators B, Chem.,* 2014, 194, 105-113.

22 A. Akyazi, J. Saez, A. Tudor, C. Delaney, W. Francis, D. Diamond, L. Basabe-Desmonts, L. Florea and F. Benito-Lopez, in *Ionic liquid devices,* ed. A. Eftekhari, Royal Society of Chemistry, 2018,

23 F. Benito-Lopez, M. Antoñana-Díez, V. F. Curto, D. Diamond and V. Castro-López, *Lab Chip,* 2014, 14, 3530-3538.

24 B. Ziólkowski, L. Florea, J. Theobald, F. Benito-Lopez and D. Diamond, *Soft Mat.,* 2013, 9, 8754-8760.

25 S. Coleman, J. ter Schiphorst, A. Azouz, S. Ben Bakker, A. P. H. J. Schenning and D. Diamond, *Sens. Actuators B, Chem.,* 2017, 245, 81-86.

26 M. Czugala, D. Maher, F. Collins, R. Burger, F. Hopfgartner, Y. Yang, J. Zhaou, J. Ducrée, A. Smeaton, K. J. Fraser, F. Benito-Lopez and D. Diamond, *RSC Adv.,* 2013, 3, 15928-15938.

27 A. Szilágyi, K. Sumaru, S. Sugiura, T. Takagi, T. Shinbo, M. Zrínyi and T. Kanamori, *Chem. Mater.,* 2007, 19, 2730-2732.

28 M. Czugala, C. Fay, N. E. O'Connor, B. Corcoran, F. Benito-Lopez and D. Diamond, *Talanta,* 2013, 116, 997-1004.

29 J. Saez, L. Basabe-Desmonts and F. Benito-Lopez, *Microfluid. Nanofluid.,* 2016, 20:116.

30 D. Diamond and V. C. A. Hanratty, *Spreadsheet applications in chemistry using Microsoft Excel*, Wiley, Dublin, 1997.

31 A. Mateescu, Y. Wang, J. Dostalek and U. Jonas, *Membranes,* 2012, 2, 49-69.

32 F. Benito-Lopez, R. Byrne, A. M. Radut^a, N. E. Vrana, G. McGuinness and D. Diamond, *Lab Chip,* 2010, 10, 195-201.

33 C. Delaney, P. McCluskey, S. Coleman, J. Whyte, N. Kent and D. Diamond, *Lab Chip,* 2013, 17, 2013-2021.

34 G. Duffy, I. Maguire, B. Heery, C. Nwankire, J. Ducrée and F. Regan, *Sens. Actuators B, Chem,* 2017, 246, 1085-1091.

6

Poly(ionic liquid) Thermo-responsive Actuators for Flow Control*

This Chapter describes the characterisation and performance of thermoresponsive crosslinked tributylhexyl phosphonium sulfopropyl acrylate (PSPA) poly(ionic liquid) hydrogels as temperature controlled valves in microfluidic devices.

*****Parts of this Chapter have been published in: A. Tudor; J. Saez; L. Florea; F. Benito-Lopez; D. Diamond, Poly(ionic liquid) thermo-responsive hydrogel microfluidic actuators, *Sens. Actuators B, Chem.*, 2017, 247, 749-755.

6.1 Introduction

Microfluidics is an interdisciplinary science capable of manipulating small volumes of fluids from picoliters to microliters[1, 2]. Microfluidics advantages[1-10] have been presented in Chapter 2. All these aims form the base of the development of the new generation of environmental analytical devices.

Many efforts have been made during these years in order to incorporate functioning devices that typically require highly specialised and bulky macroscopic equipment such as pumps, valves, and detectors to be located off-chip. One of the main challenges is the miniaturisation of macroscopic equipment to be integrated into microfluidic devices. In this sense, many approaches have been published in the literature about the use of soft materials for flow control,[11-17] as explained in previous Chapters 4 and 5. In particular, polymer-gel type materials are now becoming more reminiscent of biological units than conventional silicon components because of their biocapability. Among them, a variety of stimuli-responsive materials that respond to external changes in their local environment, such as chemicals (Chapter 4), light (Chapter 5), temperature (Chapter 6), or variations in pH, electrical and magnetic fields and pressure[18-32] have been recently described in the literature. In particular, poly(*N*-isopropylacrylamide) (pNIPAAm) is one of the most studied stimuli-responsive hydrogels, due to its lower critical solution temperature (LCST) behaviour in the presence of an aqueous medium[20, 33-35] as deeply explained in Chapter 2. For instance, this material was used in Chapter 5 for the generation of the ionogel photo-actuators in a Lab on a Disc (LoaD) device.

LCST indicates changes in the hydration attractive forces between the polymer chains themselves and with the aqueous medium. If the hydration temperature of the medium is below the LCST, the polymer chains are hydrated and swollen but when the temperature is above the LCST, the polymer chains expulse the water molecules, which leads to polymer chains to attract between them and therefore, polymer contracts[20, 33-35].

The contraction property has made pNiPAAm hydrogels interesting candidates for the fabrication of thermo-responsive microfluidic valves and for thermo-, photo-[36], magneto-responsive valving units when ionic liquids[37], photochromic molecules[14, 38], or magnetic nanoparticles[39, 40], respectively, are included in the polymer matrix (see previous chapters for more information). One of the main drawbacks in the use of hydrogels is that they disintegrate and dehydrate when they are stored for a long time in the dry state. Improvements in the physical robustness of hydrogels were reported when using ionogels instead, as explained in

Chapter 5. An ionogel is a hydrogel that contains an ionic liquid (IL) in its polymer matrix. Similar behaviours have been reported recently in a relatively new class of materials, namely poly(ionic liquid)s (PILs)[22, 29-31, 41-43]. These materials are polymers formed through the polymerisation of IL monomers, which feature a polymerisable group in the anion, the cation or both. Although generally the focus remains on linear PILs, there are several reports dealing with crosslinked PIL networks that are explored either as ion conductors[44, 45], templates for multilamellar structured nanoparticles[46] or as actuators[31, 47].

The aim of this Chapter is the integration, for the first time, of the phosphonium-based crosslinked PIL tributylhexylphosphonium sulfopropyl acrylate (PSPA) in a microfluidic structure to provide thermo-actuated flow control functionality. As described in previous chapters, these types of materials open the possibilities of generating novel analytical devices with implications in all research areas, including environmental science.

6.2 Experimental

6.2.1 Materials

Potassium 3-sulfopropyl acrylate (KSPA), 2-hydroxy-2-methylpropiophenone 97 % (HMPP), phenyl-bis(2,4,6-trimethyl benzoyl) phosphine oxide 97 % (PBPO), polypropylene glycol diacrylate (M_w ~ 800, 100 ppm MEHQ and 100 ppm BHT as inhibitors) (PPG800) and HPLC grade acetonitrile (ACN) were bought from Sigma Aldrich® (Arklow, Ireland) and used as received. Tributylhexyl phosphonium chloride was kindly donated by Cytec® Industries (Niagara Falls, Canada). Deionised water (DI water), with a resistivity of 18.2 MΩ cm^{-1}, was obtained using a Milli-Q Water Purification System from Merck Millipore (Darmstadt, Germany).

6.2.2 Synthesis of the PSPA Ionic liquid Monomer

For the PSPA synthesis, 15 g of tributylhexyl chloride (PCl) and 16 g of KSPA were dissolved in 25 mL DI water. The amount of KSPA used represents a 50 % molar excess compared to the stoichiometric value needed for this reaction. This was done to ensure that the reaction equilibrium is shifted towards the formation of PSPA. The reaction was maintained at room temperature and atmospheric pressure overnight (Figure 6.1). Purification was done by extracting the PSPA from the aqueous solution with dichloromethane. This process was repeated three times. The resulting mixture was dried over anhydrous magnesium sulfate and gravity filtered. Following this, the extraction solvent was removed by rotary evaporation and the resulting viscous mixture was dried overnight using a high vacuum pump. The obtained product was a clear, colorless viscous liquid. The yield of the synthesis was 85 %. The purity of the product was analysed using ^{1}H-NMR, δH (Bruker Advance Ultrashield, 400MHz, deuterated chloroform): 0.86–1 (*m*, 12H, CH_3), 1.28–1.33 (*m*, 4H, CH_2), 1.51–1.53 (*m*, 16H, CH_2), 2.18–2.37 (*m*, 10H, CH_2), 2.88–2.92 (*m*, 2H, CH_2), 4.25–4.29 (*t*, *J* = 6.46 Hz, 2H, CH_2), 5.77–5.80 (*dd*, 1H, *J* = 1.51, 10.42 Hz, CH), 6.04–6.11 (*m*, 1H, *J* = 10.44, 17.33 Hz, CH), 6.34–6.39 (*dd*, 1H, *J* = 1.51, 17.38 Hz, CH) ppm.

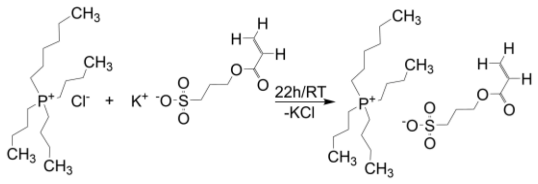

Figure 6.1: Reaction scheme for the synthesis of PSPA.

6.2.3 Crosslinked PSPA Hydrogel Disk Polymerisation

The crosslinked PILc hydrogel was synthesised by dissolving 0.1935 g (400 µmol) of PSPA in 0.1935 g of a 1:1 w/w mixture of ACN and DI water together with 0.0160 g (20 µmol) of PPG800 as the crosslinker and 0.0034 g (8 µmol) of PBPO as the photopolymerization initiator. The resulting mixture was mechanically stirred until all the components were completely dissolved. After that, the monomer solution was pipetted in poly(dimethylsiloxane) moulds 3 mm wide and 1 mm deep (Figure 6.2). To polymerise the monomer mixture, a Dolan-Jenner LMI-6000 Fiber-Lite (Boxborough, MA, USA) white-light was used at an illumination level of ~ 200 kLux for 30 min. The resulting PIL disks were swollen in DI water overnight (Figure 6.2). Based on previous studies [48], a polymerisation time of 30 min ensures that the monomer mixture is fully polymerised.

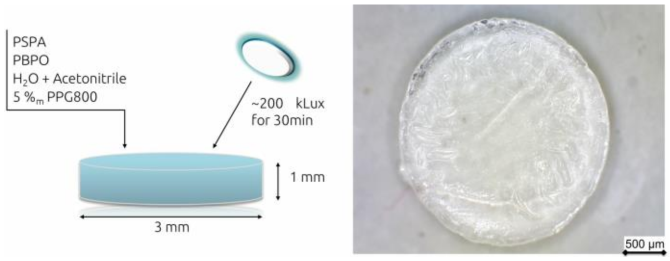

Figure 6.2: Schematic illustration of PSPA hydrogel disk; polymerisation protocol (left) and a photo of the PSPA hydrogel disk (right).

6.2.4 Characterisation of the Temperature-induced Shrinking/reswelling of the Hydrogel Disks

The resulting hydrogel disks, as seen in Figure 6.2, were transferred to an Anton Paar MCR301 rheometer (St Albans, UK) fitted with a Peltier temperature control holder with an aluminum plate. The hydrogel disks were covered with DI water and the holder was covered with a 5 mm glass plate, to ensure that the water will not evaporate when the temperature was raised. Two different experiments were performed: the first experiment focused on the study of the shrinking and swelling kinetics of the hydrogel disks, while the second experiment focused on the repeatability and the reproducibility of the shrinking and reswelling effect.

The first experiment was carried out by heating the hydrogels from 20 °C to 70 °C in 5 °C steps to analyse the shrinking effect, followed by cooling the gels at the same rate back to 20 °C to analyse the reswelling effect. The hydrogel disks were kept for 8 min at each step to ensure that the area of the hydrogel had reached a steady state. At each step, an image was taken using an Aigo GE-5 digital microscope (Chippenham, UK) having a 60x magnification objective. The hydrogels' % shrinking in area was studied using the ImageJ software[49]. Each image was analysed using the following formula:

$$\%\,Shrinking = 100 - (A_f/A_i \cdot 100) \tag{6.1}$$

Where A_f is the size of the shrunken hydrogel disk at a set temperature and A_i is the initial size of the swollen hydrogel disk.

To further illustrate this behaviour, a time-lapse video of the gel shrinking and reswelling was made by using images taken every 20 s for a total of 60 min for each shrinking and reswelling cycle, see section 6.3.1.

The second experiment was done by alternatively shrinking the hydrogel disks by applying a temperature of 50 °C and reswelling them by applying a temperature of 20 °C. This alternation was repeated six times to ensure that the temperature-induced shrinking behaviour is repeatable. The same Equation 6.1 was used in this case to calculate % shrinking in area when the hydrogels were heated to 50 °C.

6.2.5 Microfluidic Device Fabrication

The microfluidic device was fabricated from poly(methyl methacrylate) (PMMA) sheets with a thickness of 250 µm and pressure sensitive adhesive (PSA) sheets with a thickness of 60 µm. The bottom parts of the device, the well layer in which the hydrogel was polymerised and the top part of the device were cut using an Epilog Zing 16 30W CO_2 laser (Golden, CO, USA). These three PMMA layers were bound using two PSA layers, the first of which was used to connect the bottom part of the device to its polymer well layer, while the second PSA layer had the microfluidic channel cut into it and was used to connect the top part of the device to its polymer well layer (Figure 6.3). The PSA layers were cut using a Graphtec Craft Robo-Pro cutting plotter (Irvine, CA, USA). The total thickness of the device upon assembly (Figure 6.4) was 1 mm. This dimension was used to ensure the device fits in the microfluidic holder, which will be used to actuate the thermo-responsive hydrogel actuator.

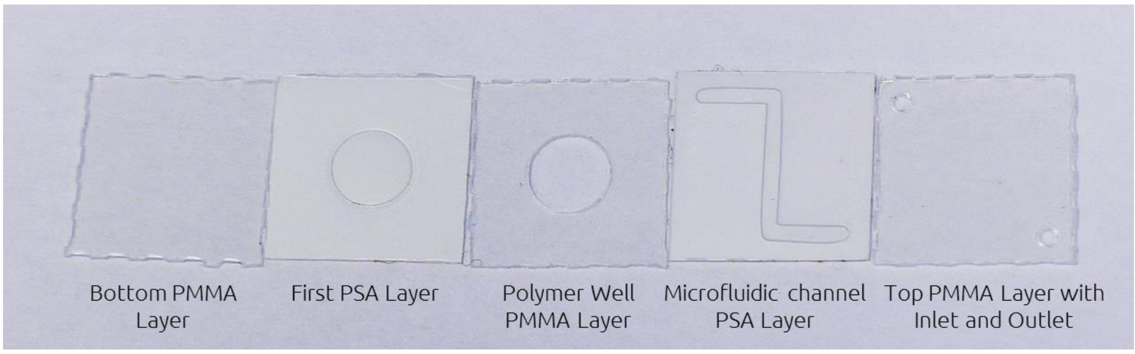

Figure 6.3: PMMA and PSA layers of the microfluidic device before assembly.

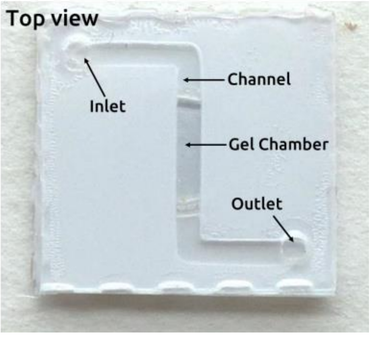

Figure 6.4: The assembled microfluidic device containing the thermo-responsive hydrogel actuator.

6.2.6 Thermo-responsive Hydrogel Actuator Characterisation

The hydrogel actuators were fabricated by photo-polymerising 3 µL of monomer mixture for 20 min using a 365nm UV lamp. In this case, the PBPO initiator was substituted, while respecting the same mol ratio, with HMPP to allow UV photopolymerisation. Based on a previously published study[50], the same polymerisation time was used in order to ensure a full monomer conversion. The thermo-response characterisation of the hydrogel actuator was carried out inserting the microfluidic device into a microfluidic holder, fitted with a heating element. This heating element sits at the bottom of the microfluidic device and is capable of homogenously increasing the temperature at a rate of 7.4 °C s^{-1} and decreasing the temperature at a rate of 2.4 °C s^{-1}. To induce shrinking in the thermo-responsive PIL hydrogel, a temperature of 50 °C was chosen, while to reswell the hydrogel the temperature was set to 20 °C. The microfluidic holder also contains the inlet and outlet connections at its sides. After the microfluidic device was placed in the holder, its inlet was connected to a WPI-Europe SP101IZ syringe pump (Berlin, Germany), while its outlet was connected to a Sensirion CMOSens (Staefa, Switzerland) flow microsensor. The flow rate was set at 500 nL min^{-1}. The scheme of the set-up can be seen in Figure 6.5.

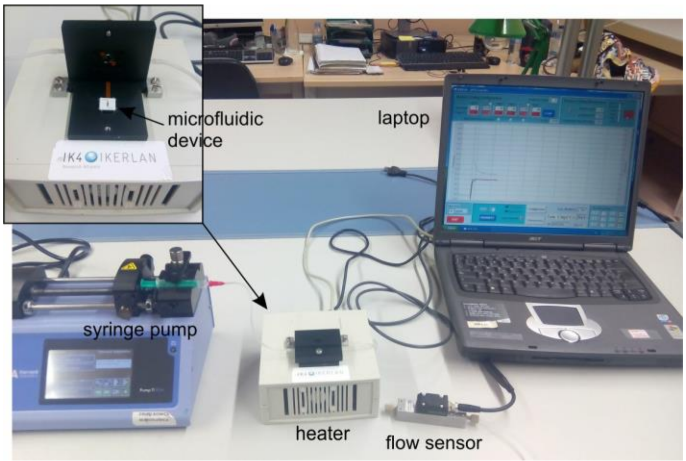

Figure 6.5: Set-up used for thermo-responsive valve actuation.

DI water was chosen as the flow medium to ensure that there are no other effects inhibiting the shrinking behaviour of the PIL hydrogels. The effect of foreign salts dissolved in the hydration medium on the temperature-induced shrinking of both linear and crosslinked PILs was investigated in several other studies[18, 28, 29, 48, 51]. For future applications envisioned to work with different kinds of solutions as flow mediums, a configuration in which the hydrogel flow control actuator is separated from the flow medium by a flexible membrane can be used, as demonstrated by Tanaka *et al.*[52] and Beebe *et al.*[11]. In both cases, they used a flexible membrane to separate an electroactive polymer and a pH-responsive hydrogel, respectively, from the analyte flow, which ensured that they operated in optimal conditions.

The results exhibited by the ionic liquid polymer flow control actuator usually follow a sigmoidal shape, as depicted in Equation 6.2.

$$Q = \frac{a}{1 + e^{k \cdot t + b}} + d \tag{6.2}$$

where *Q* is the flow rate, *t* is the time, a is the maximum *Q* value obtained when the hydrogel is fully open, *b* corresponds to the interception point value, *k* is the value of the rate constant, and *d* accounts for a baseline offset, minimum *Q*.

The fit of experimental (*Q, t*) data to this type of equation is commonly used in chemistry to obtain constant values such as pK_a (acid dissociation constant) and can be used to determine the rate constant of the ionic liquid polymer hydrogel actuator in this case.

Using the set-up from Figure 6.5 the flow rates through the device were analysed. Based on these results, further investigations were made to determine the shrinking and swelling kinetics by using the logistic curve equation (Equation 6.2) and the Origin software (see section 6.3).

6.3 Results and Discussion

6.3.1 Temperature Response of the Hydrogel Disks

In the case of conventional temperature-responsive linear polymers, such as poly(*N*-isopropylacrylamide), the LCST appears as a sharp transition at a specific temperature value (~ 32 °C for pNiPAAm)[34]. This remains valid also for linear PILs. In contrast, with crosslinked PILs the polymeric volume changes occur over a temperature interval, rather than at a sharp value, suggesting that more gradual changes are occurring in the polymer chains[31]. This phenomenon has been assigned to the decreased level of freedom of the bulky IL in the polymer network and manifests itself as an gradual decrease in size of the PIL hydrogels with an increase in temperature and *vice versa*. This behaviour also appears to occur in the PSPA hydrogels presented in this study.

Figure 6.6 shows that when the temperature was increased from 20 °C to 70 °C the hydrogels shrink by ~ 39 % at 50 °C and ~ 56 % at 70 °C. When the temperature was lowered back from 70 °C to 20 °C, the hydrogels start absorbing water until they return to their original size. The slight difference in area between the heating and the cooling cycle arose from a hysteresis process due to the fact that the heating rate is ~ 10 °C min^{-1}, while the cooling rate is ~ 13 °C min^{-1}. A video of the PSPA hydrogel thermal actuation can be visualised in the following link:

http://www.sciencedirect.com/science/article/pii/S092540051730463X#upi0010

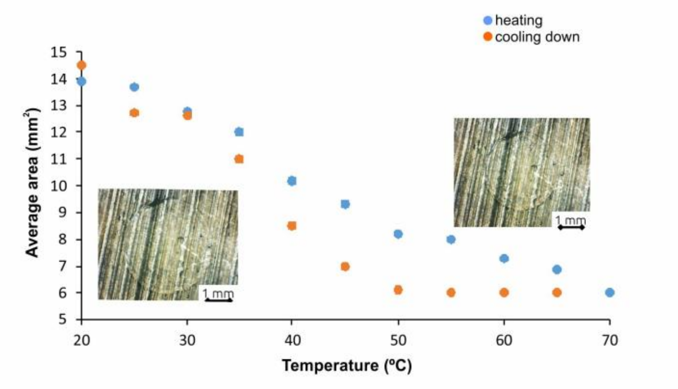

Figure 6.6: Shrinking and reswelling behaviour of the PSPA hydrogels when the temperature is increased from 20 °C to 70 °C, followed by decreasing it back to 20 °C, in 5 °C steps.

Figure 6.7 presents the results of the reproducibility and repeatability of this behaviour. In these experiments, a set of three gels were analysed by heating their hydration medium to a temperature of 50 °C to make the hydrogels shrink, followed by cooling them to 20 °C to allow for reswelling to their original size. As in the previous test, the hydrogels were kept for 8 min at each temperature, to ensure a steady-state volume was reached. The heating and cooling cycle was repeated six times. In all cases, the hydrogels shrank by ~ 44 ± 3 % (n = 6) at 50 °C and reverted back to ~ 97 ± 2 % (n = 6) of their original size when the temperature was lowered to 20 °C.

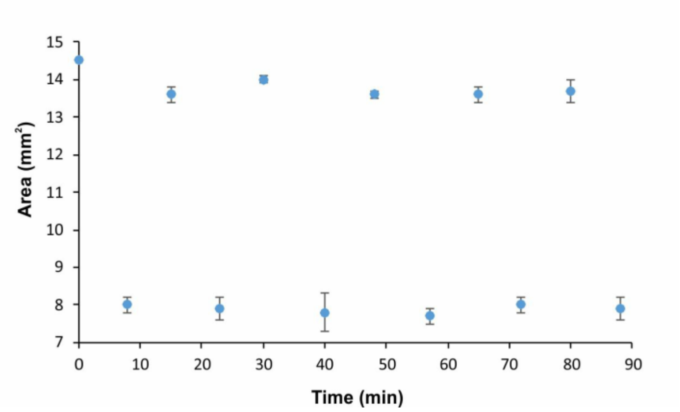

Figure 6.7: Temperature-induced shrinking by area of the PSPA hydrogels at 20 °C (top) and at 50 °C (bottom).

6.3.2 Flow Characterisation Study

Microfluidic devices were fabricated as described in the experimental section with the necessary configuration for a hydrogel to be photopolymerised and used as a temperature-controlled actuator. The hydrogel actuator was opened and closed six times (Figure 6.8), thus confirming the reproducibility and repeatability of the PIL hydrogel thermo-actuation.

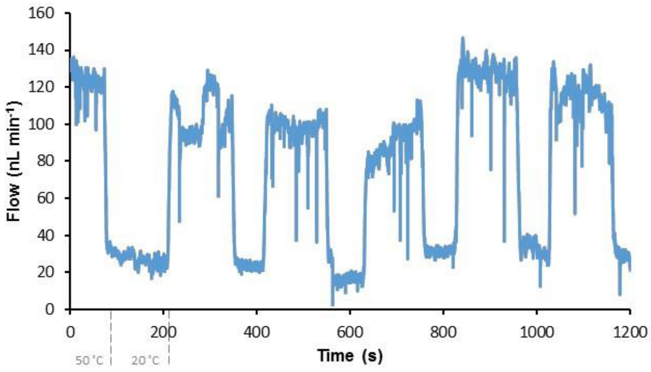

Figure 6.8: PSPA hydrogel actuator at 50 °C allowing a flow rate of ~ 140 nL min^{-1} to pass through the microfluidic channel, and at 20 °C, restricting the flow rate to ~ 20 nL min^{-1}. Fluctuations in the signal (10 ± 5 nL min^{-1}) were observed due to ambient conditions (*e.g.* vibration of the pumping system) and the ionic liquid polymer network internal reorganisation before and after temperature actuation, which is extended after the stimulus is removed due to the hydration or dehydration processes that continue to happen in the polymer.

In the “open” form, when the actuator is fully contracted, a flow of ~ 120 nL min^{-1} occurs rather than the 500 nL min^{-1} flow rate obtained with a fully open channel. This means that the PIL actuator is partially occluding the microchannel, impeding the normal flow through the microchannel. In the actuator’s “closed” form, the flow sensor still detects a residual flow of 20 nL min^{-1} rather than 0. The reason why the flow signal does not reach 0 nL min^{-1} can be attributed to small residual pathways through which the fluid still can pass:

(1) either bypassing the swollen gel (*e.g.* where the gel meets the channel top surface); or

(2) through the valve structure (due to pores or inherent liquid transport arising from the open polymeric structure of the hydrated gel).

Both of these effects can be corrected by changing the geometry of the hydrogel actuator, together with design optimisations of the microfluidic device. Moreover, the PIL hydrogel can be placed behind a thin elastic membrane, to ensure that the hydrogel does not come into contact with the liquid flowing through the microfluidic device if the application deems it necessary. Furthermore, with additional optimisation, the PIL materials could be used either as valves in simple, low-cost, microfluidic platforms or as temperature-modulated flow regulators, due to their wide LCST interval. This property can be used to affect the measured flow through a microfluidic device in a repeatable and reproducible way, thus providing enough information for a pulse width modulation feedback loop platform to control the flow through a microfluidic device automatically. In addition, to better understand the ability of this hydrogel actuator to be used in a microfluidic device, its burst pressure was determined. This was done by applying incremental changes in pressure to the hydrogel actuator starting with 5 mbar up to 400 mbar, following a similar protocol to that described in Chapter 3 (Figure 6.9). When the pressure reached the value of 250 mbar, the hydrogel actuator started degrading, which resulted in an increase in flow rate (time: 1860 s). At 400 mbar, complete failure of the hydrogel actuator was observed. Consequently, based on the results obtained for this particular microfluidic device configuration, the burst pressure was acknowledged to be 250 mbar, while the complete failure pressure was found to be 400 mbar.

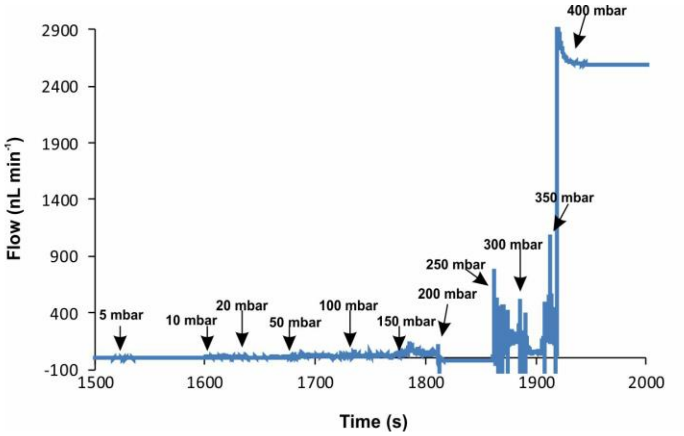

Figure 6.9: Determination of the burst-pressure of the integrated actuator via incremental increases in pressure. At pressures above 250 mbar failure in the actuator was induced, resulting in an increase in flow rate through the micro-channel. Complete failure of the actuator was achieved at an applied pressure of 400 mbar.

The shrinking and swelling rate constants of the hydrogel actuator (Table 6.1) were calculated using the logistic curve Equation 6.2 based on the flow rate measurements (Figures 6.10 and 6.10) and using the previously mentioned Origin software. The shrinking and swelling rate constants were obtained by using a common adjustment to all the data series.

The rate constants were found to be -0.66 ± 0.01 s^{-1} (n = 5) for the shrinking of the hydrogel and 0.65 ± 0.02 s^{-1} (n = 6) for the swelling of the hydrogel. The close values of the rate constants convey the fact that both effects take place at approximately the same speed, which indicates no perceptible hysteresis between the opening and the closing of the PIL hydrogel flow regulator when the temperature was cycled between 50 °C and 20 °C (Figures 6.10 and 6.10). This effect is confirmed by the fact that the closing and opening time of the hydrogel actuator varies between 5 and 8 s. The actuation time values compare favourably with actuation times given for other stimuli-responsive hydrogel actuators based on conventional thermo-responsive polymers[53], or for several phase-change mechanical actuators based on paraffin wax[6], while being similar to state of the art values found in hydrogel valves[37, 54]. Compared to other types of actuators, especially vacuum operated or electrically operated hard valves, the response times are slower. Regardless of this, there are several ways in which their response times could be improved. Among them, the following can be mentioned: (a) fitting a heating element capable of much faster heating and cooling rates; (b) changing the geometry of the hydrogel and the hydrogel positioning to ensure that there is a need for less hydrogel to open and close the microchannel; and (c) the addition of a pore-forming agent to the monomer mixture, such as high molecular weight poly(ethylene glycol), which would help the hydrogel absorb and expel its hydration medium faster[54].

Table 6.1: Experimental shrinking and swelling rate constants obtained by curve fit adjustment to Equation 6.2 provided by Origin software.

Shrinking Parameters

a		b		K_{sh}		d	
Value	**Standard Error**	**Value**	**Standard Error**	**Value (s^{-1})**	**Standard Error (s^{-1})**	**Value**	**Standard Error**
86.3	0.9	5.8	0.1	-0.66	0.01	23.3	0.6
73.7	0.9	6.1	0.1			25.1	0.6
64.4	0.9	6.8	0.1			14.0	0.5
106.5	1.5	6.2	0.1			31.0	0.6
111.0	1.2	5.7	0.1			20.6	0.7

Swelling Parameters

a		b		K_{sw}		d	
Value	**Standard Error**	**Value**	**Standard Error**	**Value (s^{-1})**	**Standard Error (s^{-1})**	**Value**	**Standard Error**
102.3	2.1	-3.3	0.1	0.65	0.02	29.1	0.9
86.1	1.8	-3.7	0.1			24.1	1.0
93.4	3.4	-2.2	0.1			24.6	1.0
69.9	2.8	-5.8	0.2			38.7	2.8
79.2	1.7	-4.6	0.1			51.1	1.4
71.2	1.6	-3.7	0.1			32.8	1.0

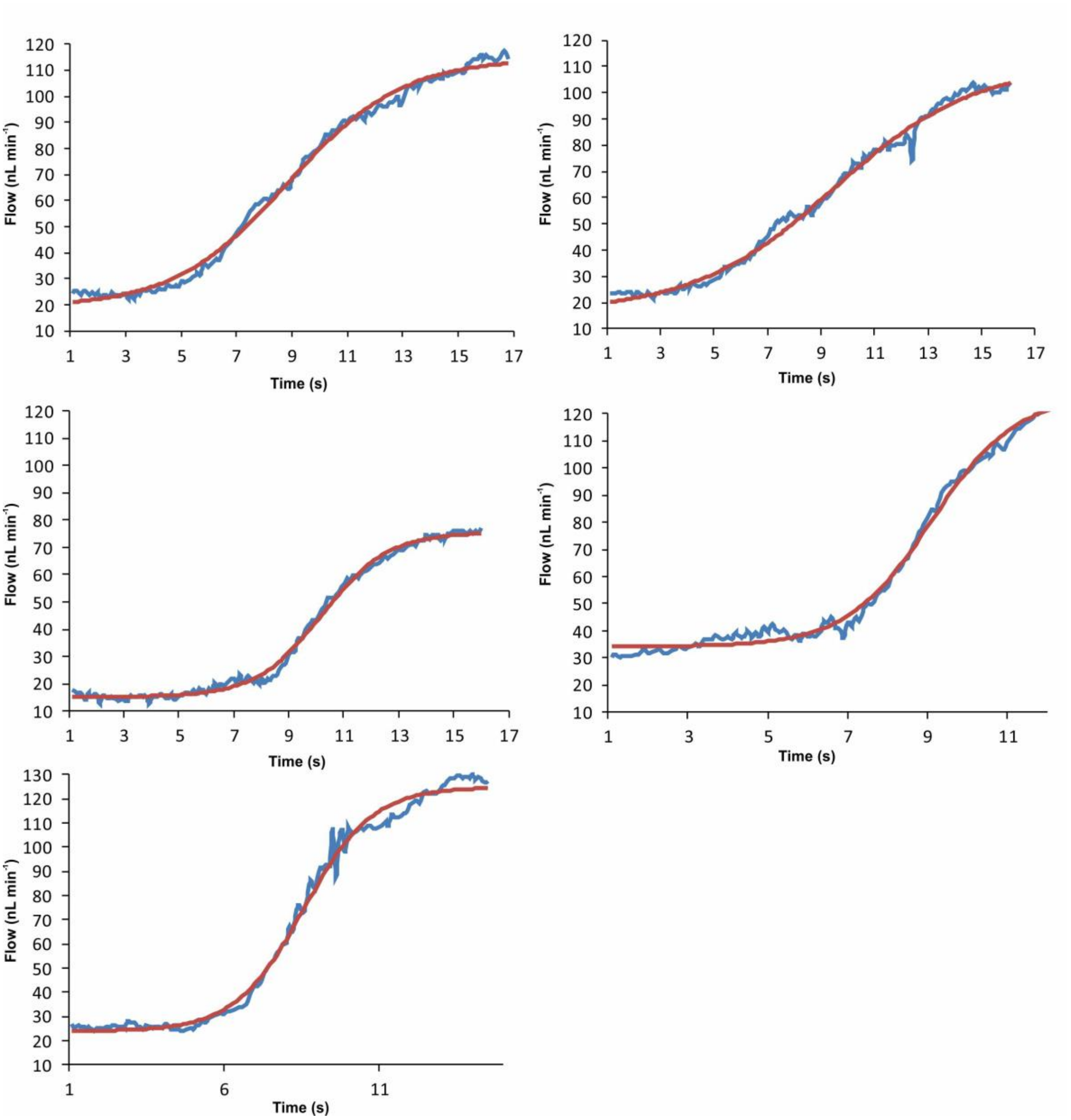

Figure 6.10: Shrinking kinetics of the PILc hydrogel valve when the temperature was raised from 20 °C to 50 °C. The blue line represents the experimental flow rate, while the red line represents the modeled flow rate according to Equation 6.2.

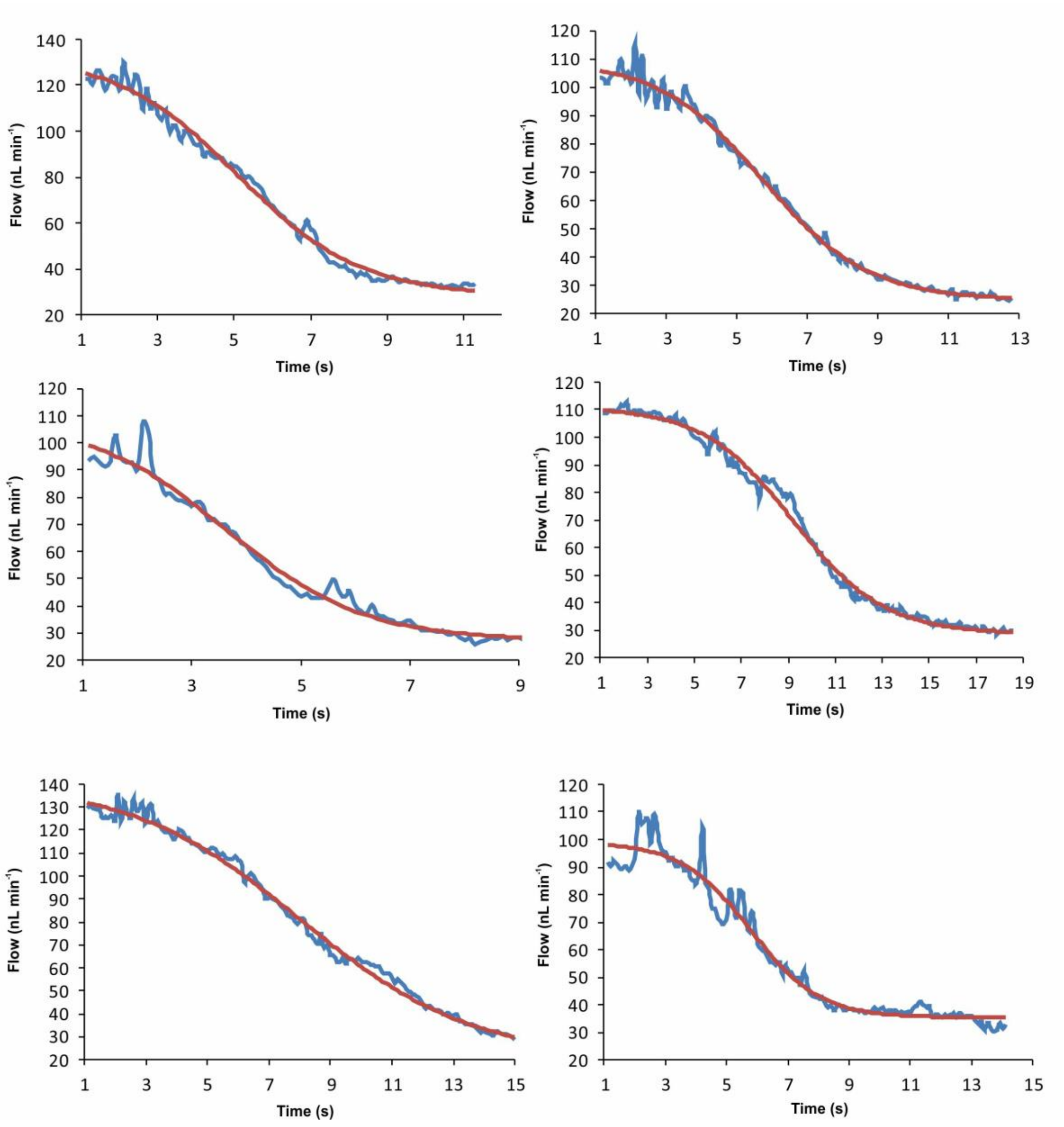

Figure 6.11: Swelling kinetics of the PILc hydrogel valve when the temperature was lowered from 50 °C to 20 °C. The blue line represents the experimental flow rate, while the red line represents the modeled flow rate according to Equation 6.2.

6.4 Conclusions

In conclusion, a tributylhexyl phosphonium sulfopropyl acrylate ionic liquid monomer was synthesised and photopolymerised to produce a poly(ionic liquid) hydrogel that features an interval LCST. In contrast with actuators and valves from Chapter 4 (alginate valves) and Chapter 5 (photo-switchable actuators), this hydrogel is able to shrink by increasing the temperature of its surrounding hydration medium. Based on this thermo-responsive behaviour, the hydrogel actuation behaviour was fully characterised and the hydrogel was incorporated into a microfluidic device with the purpose of being used as a temperature-controlled actuator. The characterisation of the hydrogel indicates that the hydrogel shrinks by ~ 58 % of its swollen area when the temperature is raised from 20 to 70 °C and ~ 39 % when the temperature is raised from 20 to 50 °C. Furthermore, the hydrogel is able to shrink and reswell repeatedly when subjected to temperature cycles between 20 °C and 50 °C. Moreover, by including the hydrogel in a microfluidic device as a temperature-controlled actuator, the microfluidic channel was modulated between ~ 110 ± 15 nL min^{-1} (n = 6) and ~ 27 ± 5 nL min^{-1} (n = 6) by varying the temperature between 50 °C and 20 °C. This process was repeated six times with no performance loss, thus suggesting the possibility of repeatable use for more than six times. Based on these results and taking into account the vast collection of ionic liquids available and their synthetic versatility, thermo-responsive poly(ionic liquid)s could constitute a new tool for the generation of simple and low-cost temperature responsive microfluidic actuators.

6.5 References

1 P. N. Nge, C. I. Rogers and A. T. Woolley, *Chem. Rev.*, 2013, 113, 2550-2583.
2 G. M. Whitesides, *Nature*, 2006, 442, 368-373.
3 L. Dong and H. Jiang, *Soft Mater*, 2007, 3, 1223.
4 I. Araci and P. Brisk, *Curr. Opin. Biotechnol*., 2014, 25, 60-68.
5 M. I. Mohammed, E. Abraham and M. P. Y. Desmulliez, *J. Micromech. Microeng*., 2013, 23, 35034.
6 S. Ogden, L. Klintberg, G. Thornell, K. Hjort and R. Bodén, *Microfluid. Nanofluid*., 2014, 17, 53-71.
7 K. W. Oh and C. H. Ahn, *J. Micromech. Microeng.,* 2006, 16-20.
8 P. Selvaganapathy, E. T. Carlen and C. H. Mastrangelo, *Sens. Actuators A, Phys*., 2003, 104, 275-282.
9 B. Yang and Q. Lin, *Sens. Actuators A, Phys.,* 2007, 134, 194-200.
10 C. Zhang, D. Xing and Y. Li, *Biotech. Adv*., 2007, 25, 483-514.
11 D. J. Beebe, J. S. Moore, J. M. Bauer, Q. Yu, R. H. Liu, C. Devadoss and B.-H. Jo, *Nature*, 2000, 404, 588-590.
12 A. K. Agarwal, L. Dong, D. J. Beebe and H. Jiang, *Lab Chip*, 2007, 7, 310-315.
13 L. Florea, D. Diamond and F. Benito-Lopez, *Research Perspectives in Functional Micro-and Nanoscale Coatings,* 2016, 265.
14. J. ter Schiphorst, S. Coleman, J. E. Stumpel, A. Ben Azouz, D. Diamond and A. P. Schenning, *Chem. Mat.,* 2015, 27, 5925-5931.
15 B. Ziółkowski, M. Czugala and D. Diamond, *J. Int. Mat. Syst. Struc*., 2012, 1045389-12459591.
16 M. Czugala, C. O'Connell, C. Blin, P. Fischer, K. J. Fraser, F. Benito-Lopez and D. Diamond, *Sens. Actuators B, Chem*., 2014, 194, 105-113.
17 J. Saez, J. Etxebarria, M. Antoñana-Diez and F. Benito-Lopez, *Sens. Actuators B, Chem.,* 2016, 234, 1-7.
18 Y. Men, X.-H. Li, M. Antonietti and J. Yuan, *Polym. Chem*., 2012, 3, 871.
19 R. Bogue, *Assembly Autom.,* 2012, 32, 37.
20 C. Boutris, E. G. Chatzi and C. Kiparissides, *Polymers*, 1997, 38, 2567-2570.
21 L. Florea, D. Diamond and F. Benito-Lopez, *Macromol. Mater. Eng.,* 2012, 297, 1148-1159.
22 S. Gallagher, L. Florea, K. J. Fraser and D. Diamond, *Int. J.Molec. Sci.,* 2014, 15, 5337-5349.
23 S. Gallagher, A. Kavanagh, B. Zíołkowski, L. Florea, D. R. MacFarlane, K. Fraser and D. Diamond, *Phys. Chem.,* 2013, 16, 3610-3616.
24 M. R. Guilherme, R. da Silva, A. F. Rubira, G. Geuskens and E. C. Muniz, *React. Funct. Polym*., 2004, 61, 233-243.
25 M. Hammarson, J. R. Nilsson, S. Li, T. Beke-Somfai and J. Andréasson, *J. Phys. Chem. B*, 2013, 117, 13561-13571.
26 L. Ionov, *Mater. Today*, 2014, 17, 494-503.
27 Y. Kohno, Y. Deguchi and H. Ohno, *Chem. Comm.,* 2012, 48, 11883-11885.
28 Y. Kohno and H. Ohno, *Aust. J. Chem.,* 2012, 65, 91-94.
29 Y. Kohno, S. Saita, Y. Men, J. Yuan and H. Ohno, *Polym. Chem.,* 2015, 2163-2178.
30 J. Yuan, D. Mecerreyes and M. Antonietti, *Progs Polym. Sci.,* 2013, 38, 1009-1036.
31 B. Ziółkowski and D. Diamond, *Chem. Comm.,* 2013, 49, 10308-10310.
32 B. Ziółkowski, L. Florea, J. Theobald, F. Benito-Lopez and D. Diamond, *Soft Matter,* 2013, 9, 8754-8760.
33 Y. Maeda, T. Higuchi and I. Ikeda, *Langmuir*, 2001, 17, 7535-7539.
34 H. G. Schild, *Prog. Polym. Sci.,* 1992, 17, 163-249.
35 X. Z. Zhang, Y. Y. Yang, T. S. Chung and K. X. Ma, *Langmuir*, 2001, 17, 6094-6099.
36 T. Glennon, J. Saez, M. Czugala, L. Florea, E. McNamara, K. J. Fraser, J. Ducree, D. Diamond and F. Benito-Lopez, In *International Conference on Solid-state Sensors, Actuators and Microsystems, Transducers*, 2015, 109-112.
37 F. Benito-Lopez, R. Byrne, A. M. Răduţă, N. E. Vrana, G. McGuinness and D. Diamond, *Lab Chip*, 2010, 10, 195-201.
38 S. Sugiura, K. Sumaru, K. Ohi, K. Hiroki, T. Takagi and T. Kanamori, *Sens. Actuators A, Phys.,* 2007, 140, 176-184.
39 N. S. Satarkar, W. Zhang, R. E. Eitel and J. Z. Hilt, *Lab Chip*, 2009, 9, 1773-1779.
40 S. Ghosh, C. Yang, T. Cai, Z. Hu and A. Neogi, *Appl. Phys.,* 2009, 42, 135501.
41 G. Vancoillie, D. Frank and R. Hoogenboom, *Progs. Polym. Sci.,* 2014, 39, 1074-1095.
42 D. Mecerreyes, Progs. *Polym. Sci.,* 2011, 36, 1629-1648.

43 F. Benito-Lopez, M. Antoñana-Díez, V. F. Curto, D. Diamond and V. Castro-López, *Lab Chip*, 2014, 14, 3530-3538.
44 M. Yoshizawa and H. Ohno, *Electrochim. Acta*, 2001, 46, 1723-1728.
45 A. S. Shaplov, E. I. Lozinskaya, D. O. Ponkratov, I. A. Malyshkina, F. Vidal, P.-H. Aubert, O. g. V. Okatova, G. M. Pavlov, L. I. Komarova, C. Wandrey and Y. S. Vygodskii, *Electrochim. Acta*, 2011, 57, 74-90.
46 M. Koebe, M. Drechsler, J. Weber and J. Yuan, *Macromolec. Rapid Comm*., 2012, 33, 646-651.
47 S. Gallagher, L. Florea, K. Fraser and D. Diamond, *Int. J. Molec. Sci.*, 2014, 15, 5337-5349.
48 A. Tudor, L. Florea, S. Gallagher, J. Burns and D. Diamond, *Sensors*, 2016, 16, 219.
49 C.A. Scheneider, W.S. Rasband and K.W. Eliceiri, *Nature Meth*., 2012, 9, 671-675.
50 B. Ziółkowski, Z. Ates, S. Gallagher, R. Byrne, A. Heise, K. J. Fraser and D. Diamond, Macromolec. *Chem. Phys*., 2013, 214, 787796.
51 Y. Men, H. Schlaad, A. Voelkel and J. Yuan, *Polym. Chem*., 2014, 5, 3719-3724.
52 Y. Tanaka, T. Fujikawa, Y. Kazoe and T. Kitamori, *Sens. Actuators B, Chem*., 2013, 184, 163-169.
53 C. H. Zhu, Y. Lu, J. Peng, J. F. Chen and S. H. Yu, *Adv. Funct. Mat.,* 2012, 22, 4017-4022.
54 E. Lee, H. Lee, S. I. Yoo and J. Yoon, *ACS Appl. Mater. Interfaces,* 2014, 6, 16949-16955.

7

Integration of Microporous Materials I: Phantom Membranes for Pollutants Detection in Water*

This Chapter describes the integration of perfluorinated membranes with refractive indexes similar to that of water in a novel multilayer cyclic-olefin polymer and pressure sensitive adhesive hybrid microfluidic device. The membrane enables combining filtration and label-free sensing of pollutants in environmental water samples. The sensing capabilities of the device were tested with real water samples containing a large number of particles, without showing clogging of the membrane and enabling the quantification of pollutants in a few minutes.

*****Parts of this Chapter have been published in: R. Lanfranco; J. Saez; E. Di Nicolò; F. Benito-López; M. Buscaglia, Phantom Membrane Microfluidic Cross-Flow Filtration Device for the Direct Optical Detection of Water Pollutants, *Sens. Actuators B Chem., 2017*. DOI: 10.1016/j.snb.2017.11.024.

7.1 Introduction

Contamination of water is a constant concern all over the world. The availability of uncontaminated water for drinking and for agricultural processes is a fundamental need for human life. Moreover, pollution of water basins has a strong impact on the overall environmental equilibrium. Every day, as a result of both domestic and industrial activities, substances threatening the survival of flora and fauna are poured in the aquatic ecosystems. Some of the most widespread contamination types include fecal pollutants[1], harmful organic and inorganic substances, and oils and emulsifiers[2], such as the compounds that are present in detergents and soaps[3]. Among these, hydrophobic and amphiphilic compounds tend to migrate to the air/water interfaces, preventing proper oxygen exchange, and to accumulate in many living organisms, hence threatening their life[4]. Therefore, it would be extremely important to develop analytical systems capable of continuous and extensive monitoring of the quality of water. In analytical laboratories, liquid chromatography and mass-spectroscopy are widely employed approaches to detect contaminants in liquid matrices and solubilised media[5,6,7]. However, they require several processing steps and highly specialised instrumentation and hence, they are not suitable for the implementation in autonomous platforms capable of on-site, real-time monitoring. Nowadays, the proper quantification of most contaminants still requires the highest analytical performance only obtained in the laboratory by highly trained personnel[8]. Consequently, the required sample collection and transportation necessarily prevents the possibility of a rapid intervention in case of contamination. In order to overcome these limits, different kinds of autonomous and deployable analytical platforms have been proposed[9,10,11]. However, their overall cost per analysis is typically high and, consequently, the sampling frequency and the number of sampled sites are largely affected by budget restrictions. Despite the constant innovation towards more sensitive and robust detection methods[12], the components of the analytical platform that often have a higher impact on the cost of production and maintenance are still those devoted to sampling and handling of the liquid, such as pumps, valves, and filters, as explained in Chapter 2.

In the quest for novel paradigms for environmental analysis enabling rapid detection and identification of compounds at the point of need, microfluidic devices are emerging as versatile tools offering many advantages, including the possibility of cost-effective automation, low reagent consumption, and multiplexing[13,14]. Microfluidics has been successfully applied to different aspects of environmental analysis, in particular for water samples, such as sample preparation and on-chip detection of analytes[15]. Different materials for the fabrication of microfluidic devices have been proposed since the beginning of the investigations in microfluidic technology. Silicon has been the base material for numerous applications, as reported in previous Chapters[16]. Compared to silicon, glass and polymeric materials have the advantage of being cheap and optically transparent. However, glass still needs expensive and tedious fabrication protocols, such as photolithography and etching procedures, for the fabrication of microfluidic devices. Therefore, polymeric materials are becoming the substrates more widely used since they combine low prices and easy fabrication protocols. Some commonly used polymer materials include polymethylmethacrylate (PMMA) (see Chapters 5, 6 and 9), polydimethylsiloxane (PDMS), polystyrene (PS), polycarbonate (PC) or cyclic olefin polymer (COP) (see Chapters 3, 4, 8[17]). In particular, COP is being increasingly used for the fabrication of microfluidic systems because it shows outstanding properties while being cheap and optically transparent, as demonstrated in Chapters 3 and 4. It has a high heat resistance with a glass transition temperature (*Tg*) of 136 °C. It also has the lowest water absorbency of all plastics, and because of this, it has a great dimensional stability under high humidity conditions. In addition to this, it is chemically resistant and malleable, and it can be functionalised to perform surface assays[18]. Moreover, this thermoplastic polymer has a low degree of impurities, becoming a biocompatible material for biological, medical or environmental applications[19].

The combination of microfluidics and innovative materials for liquid handling (Chapters 4, 5 and 6) and sensing (Chapter 7, 8 and 9) represents a particularly promising approach to design new concepts for deployable analytical systems for water monitoring with reduced complexity and cost[20,21]. Recently, different optical techniques based on novel sensing substrates, either planar or surface-structured, have been proposed for the fabrication of analytical systems with improved performance for the detection of polluting molecules, possibly to be used outside the laboratories[22,23]. Among these methods, the use of perfluorinated polymers with a refractive index similar to that of water represents a promising approach to fabricate cost-effective, autonomous and sensitive microfluidic analytical devices entirely made of polymeric material. In fact, the detection and characterisation of molecular targets in aqueous samples have been demonstrated with perfluorinated materials with different shapes, including planar surfaces, nanoparticles, and microporous membranes[24,25,26]. In particular, in the Reflective Phantom Interface (RPI) method, the intensity of light reflected by a planar interface between Hyflon AD® (Solvay Specialty Polymer, Italy) and an aqueous sample enables to monitor and quantify in real-time the binding of bio-molecules or the adsorption of compounds without the need of labelling agents such as fluorescent or colorimetric moieties, that is, following a “label-free” approach. Similarly, in the Scattering Phantom Interface (SPI) approach, the adhesion of molecules taking place on the surface of dispersed nanoparticles or in porous membranes fabricated with Hyflon AD leads to an increase in the intensity of the scattered light. The optical response of these different materials has been modeled in detail[26]. Although the highest theoretical sensitivities can be obtained using the dispersions of nanoparticles, their possible aggregation makes this system suitable only for molecular targets and sample solutions that do not destabilise the suspension. In contrast, this limitation does not apply to planar surfaces or to microporous membranes. Quite surprisingly, given a specific surface density of adhering molecules, the optical signal from these two systems is identical[26], although they provide a very different surface area for the adhesion of target molecules. For those applications in which a reduced volume of sample is not a requirement (*e.g.* water monitoring), a membrane sensor is preferable, especially if its filtering capability can be also exploited. Microfluidic devices embedding microporous membranes have been produced for different applications in order to implement automatic sample filtration[27] or, alternatively, as supports for cell culturing or scaffolds for tissue engineering[28]. In contrast, to our knowledge, a device integrating a membrane that also provides the function of label-free optical sensor represents a brand new concept.

In this Chapter, the fabrication and characterisation of a hybrid microfluidic device embedding a novel perfluorinated microporous membrane isorefractive to water, from now on phantom membrane, which enables the continuous monitoring of aqueous samples, is demonstrated. The performance of the device is tested with real river water samples collected from two different sites, upstream and downstream an urban area.

7.2 Experimental

7.2.1 Materials and Equipment

For the preparation of the membrane, Hyflon AD® was generously donated from Solvay Specialty Polymers (Bollate, Italy). Solvents HFE-7100 [$CH_3OCF_2CF(CF_3)_2$] and Cyclohexanone [$C_6H_{10}O$] were purchased from 3M-Novec and Sigma-Aldrich (Milan, Italy), respectively. Ethanol and acetone were purchased from Merck (Madrid, Spain). SBSAC was purchased from Sigma-Aldrich.

For the fabrication of the microfluidic device, Zeonor COP sheets from Zeonex (Düsselforf, Germany) and ArCare® 8939 Pressure Sensitive Adhesive (PSA) from Adhesive Research

(Limerick, Ireland) were used. A Graphtec FC8000-60 cutting plotter was used for cutting COP and PSA structures from Graphtec® (Armstrong, CA, USA).

Samples were moved inside the microfluidic device by using a syringe pump RS 232-Genie Touch from Kent Scientific Corporation (Torrington, CT, USA).

A custom optical apparatus to measure the intensity of light scattered by the membrane was designed and realised on an optical board, using optomechanical components purchased from Thorlabs (Newton, NJ, USA). The light of a LED with peak wavelength 592 nm was purchased from Lumileds (Suresnes, France) and a CCD camera to Stingray Allied Technology (Stadtroda, Germany).

7.2.2 Membrane Fabrication

A microporous perfluorinated membrane that provides a real-time, label-free SPI optical response upon adsorption of organic substances present in water was fabricated. The membrane was fabricated by the non-solvent induced phase separation (NIPS) technique[29], a method widely used in the production of commercial filters and hollow fibres. In this method, a thin film of a solution containing the polymer that forms the solid structure of the membrane is cast on a cooled glass plate and immersed into a coagulation bath to induce the phase separation. The solution was prepared to dissolve the polymer Hyflon AD40® in the solvents HFE-7100 [$CH_3OCF_2CF(CF_3)_2$], and Cyclohexanone [$C_6H_{10}O$] under stirring for 24 h at room temperature. Then, the solution was ultra-sonicated for 30 min to eliminate bubbles. The coagulation bath was composed by a mixture of ethanol/acetone 1:1 (v/v), non-solvents of the polymer, in which the solvent HFE-7100 is miscible. The casting plate was immersed in the coagulation bath for 15 min maintaining the temperature at 25 °C. Then, a second coagulation step of 10 min with ethanol enabled to extract the residual solvents. The membrane samples were stored in a 30 % - 70 % (v/v) mixture of ethanol-water at room temperature. In these conditions, the membranes were probed to be stable, when stored at room temperature and in the dark, for more than one year.

The membranes were characterised by different analytical methods. Their morphology was investigated by Scanning Electron Microscopy (SEM) and their thicknesses measured by a micrometer, yielding values of 90 ± 10 µm. The porosity obtained by weighing the membrane, when soaked with isopropanol and dried, is 0.73. The amount of residual solvent was estimated as 1.1 % by Thermal Gravimetric Analysis (TGA). A mean pore diameter of 9.1 µm was obtained by nitrogen flow measurements. The membrane refractive index, 1.3285, was measured from the dependence of the scattered light intensity on the refractive index of water-glycerol solutions. The hydrophobicity of Hyflon AD® is slightly smaller than that of fully fluorinated polymers such as PTFE, because of the presence of a partially hydrogenated co-monomer that prevents local crystallisation. The contact angle for water of a planar surface of Hyflon AD® is in the range 110 ° - 120 °. Therefore, efficient wetting of the microporous membrane with water is achieved by pre-wetting with a 30 %-70 % vol ethanol-water solution.

7.2.3 Microfluidic Device Design and Fabrication

Before testing the final microfluidic device, other two iterations of its design were previously developed. First, a hybrid microfluidic device consisting of seven xurographied 100 µm COP layers and two 150 µm PSA layers was fabricated. This first generation was envisioned as three blocks of COP bonded by thermocompression (136 °C, 4 bar for 1 h) and linked by the PSA layers. The membrane was placed in a reservoir (6 mm diameter) between the second and the third module. The main channel (1 mm width) crosses through the membrane and it is linked to a parallel channel (500 µm width). The first generation had a total thickness of 1 mm (see Figure 7.1 A and B).

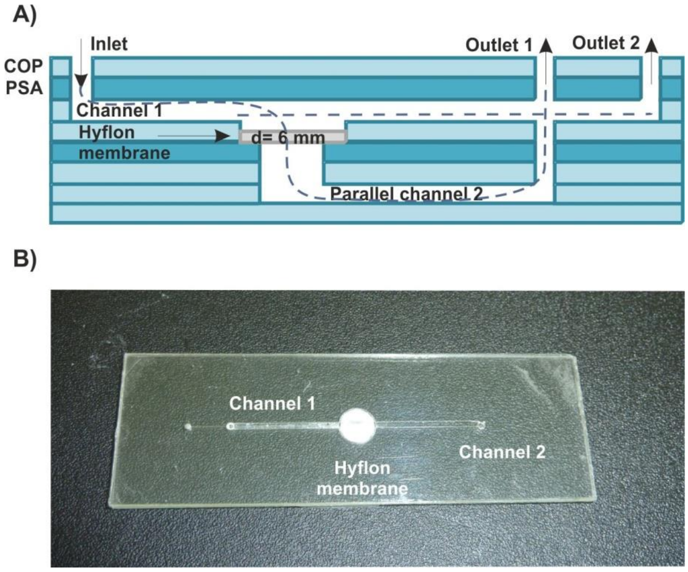

Figure 7.1: A) Cross section scheme of the first generation of the microfluidic device (not in scale) and B) picture of the microfluidic device with the integrated perfluorinated membrane.

The second generation of the microfluidic device consisted of twelve layers of COP bonded by thermocompression together with PSA layers, in a similar way than in the previous configuration. The device was designed with two channels; a straight channel 1 (250 µm height, 400 µm width) with a 10 mm diameter chamber (400 µm) where the membrane is integrated at the middle of the main channel, and a channel 2 (300 µm height, 1 mm width, 1 cm length) located diagonally to collect the sample after filtration through the membrane (see Figure 7.2 A and B).

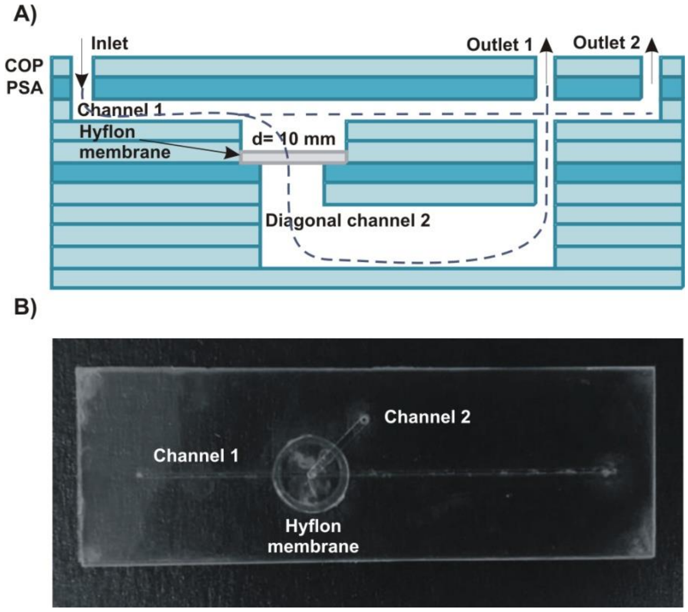

Figure 7.2: A) Cross section scheme of the second generation of the microfluidic device (not in scale) and B) picture of the microfluidic device with the integrated perfluorinated membrane.

In the third and final iteration of the design, the membrane is hosted in a hybrid microfluidic device in a cross-flow configuration to avoid the clogging in the presence of particulate material. Figure 7.3 A shows a SEM picture of the membrane. A schematic representation of the microfluidic design is shown in Figure 7.3 B and C. The device was fabricated with COP and PSA using a multilayer technique as explained before[19], and the membrane was positioned during its assembly. The microfluidic device has two inlet ports that merge in a single channel in the upper layer. This channel is tangential to the membrane and goes to the upper outlet port. Below the membrane, a bottom channel brings the filtered sample to another outlet that also was connected to the upper surface of the device. The perfluorinated membrane is suspended in a rectangular chamber with size 5 x 3 mm formed by the intersection of the two principal channels of the device, placed in the upper and bottom layers of the microfluidic device, respectively.

The microfluidic device was fabricated by rapid prototyping using the cutting plotter to precisely cut the COP and PSA layers. The COP layers of 100 µm thickness were xurographied and bonded by thermocompression. In order to deposit the membrane within the microfluidic channel in a robust way, the top and the bottom layers of the microfluidic device where bonded together with a PSA layer of 150 µm that acts as a substrate to hold the membrane (Figure 7.3 C). The final hybrid microfluidic devices are composed of 12 layers of COP with a total section of 7.5 x 2.5 mm, and 1.4 mm total thickness[30,31]. The upper channel, which passes above the membrane, has a height of 200 µm and a width 1 mm. The bottom channel, which is orthogonal to the upper channel and passes below the membrane, has a height of 300 µm and a width 3 mm (Figure 7.3).

The perfluorinated membrane was embedded into the microfluidic device during the assembly. Before assembly, the membrane was soaked for 24 h with MilliQ water at room temperature and then cut using a scalpel. The device was finally filled with water and degassed for 40 min at control temperature (30 °C) to eliminate trapped air bubbles. Female Luer connectors were glued to the input channels of the membrane using a double side PSA layer with the diameter of the Luer. Home-made male connectors that minimise dead-volumes were used directly connected to a syringe pump using a 200 mm long silicone tube with diameter 100 µm.

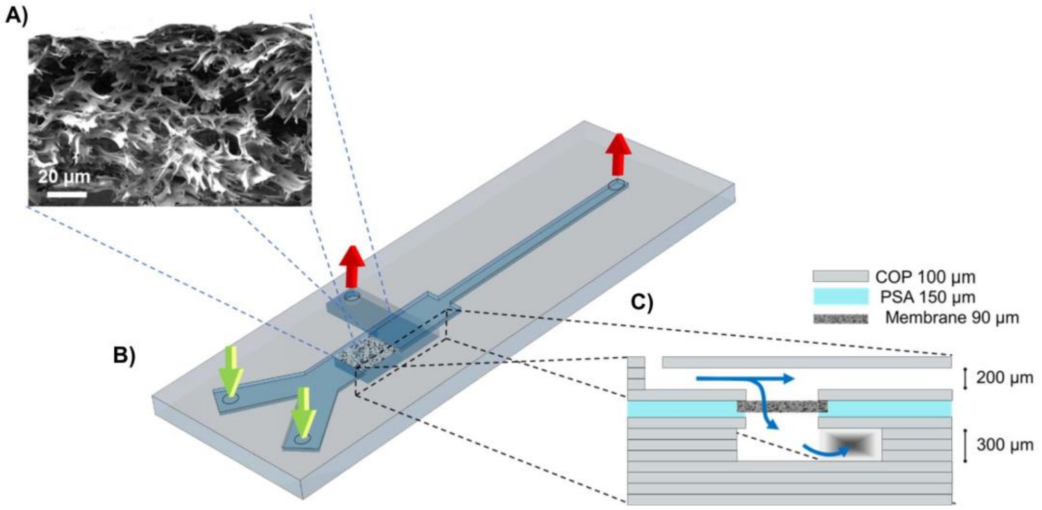

Figure 7.3: Scheme and picture of the final microfluidic device hosting the microporous membrane (not in scale). A) SEM image of the microporous membrane. B) 3D view of the cross-flow geometry that enables the simultaneous filtration process and optical detection. C) Scheme of the cross-section of the microfluidic device.

7.2.4 Optical Set-up and Measurement

A custom optical apparatus to measure the intensity of light scattered by the membrane was designed and assembled on an optical board, using optomechanical components (Figure 7.4). The light of a LED with a peak wavelength of 592 nm was collimated and shaped in order to reduce the stray light contribution possibly originated by reflections from the edges of the channels or of the membrane. A lens collects the back-scattered light at about 135° relative to the transmitted beam and forms an image of the membrane surface on a CCD camera to monitor the scattered light intensity. The microfluidic device and the optical system are placed in a black enclosure to prevent spurious signals due to ambient light. The measurements are performed at room temperature without any temperature control system. A LabView program registers the images captured by the CCD camera at a speed of 1 fps. The images are then analysed using ImageJ; the contrast is adjusted in the same way for all the data collected and a moving average is performed over 5 frames to reduce the noise. Then, the averaged intensity of the image acquired from the membrane area was computed as a function of time.

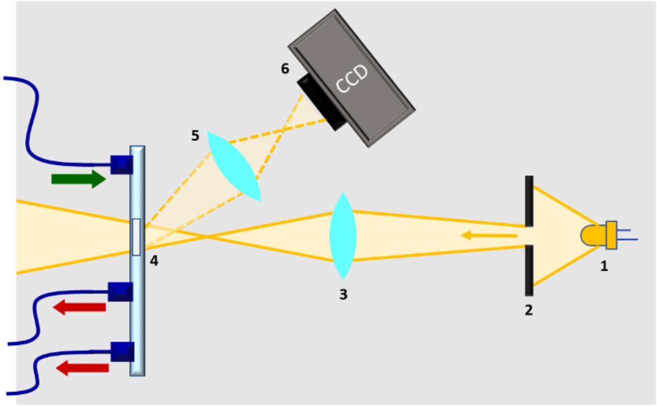

Figure 7.4: Optical instrument for the measurement of the intensity of light scattered by the microporous membrane embedded in the microfluidic device. The light emitted by a LED (1) is shaped by imaging the plane of an aperture (2) on the membrane plane (4) by a convex lens (3). The scattered light is collected by a second lens (5) that forms an image of the membrane plane on a CCD sensor (6).

The intensity of the light scattered by the membrane and acquired by this optical set-up provides a quantification of molecular adsorption on the inner surface of the membrane[26]. The surfactant was dissolved either in deionised water or in a sample of real water collected from Lambro river at Ponte Albiate (site 1) and Melegnano (site 2) in Italy (see Figure 7.5). Neither centrifugation nor filtration steps were performed before the measurement. All the experiments were performed at room temperature 25 °C. After each experiment, the tubes and connectors of the fluidic system were washed with fresh water and ethanol. The microfluidic device hosting the membrane was washed by flowing for at least an hour a 30 % - 70 % vol ethanol-water solution after each set of measurements. With this procedure, a single microfluidic device could be used for more than a dozen sets of measurements with no sign of degradation.

Figure 7.5: Sample collection points at Ponte Albiate and Melegnano at Milano city.

7.2.5 Optical Model

The peculiar optical properties of the microporous membrane of Hyflon AD® are due to the refractive index similar to that of water and to the amorphous structure of the material. When dried, the membrane appears white because of the refractive index mismatches with air and yields to a large fraction of scattered light. When soaked with an aqueous solution, the membrane becomes highly transparent because of the small difference in refractive index between the solid and the liquid phases and the absence of microcrystalline domains (Figure 7.6). In this condition, the adsorption of compounds with higher refractive index, as basically any carbon-based compound, on the inner surface of the membrane induces an increase of the scattered light by SPI that can be easily detected by a simple optical system[26]. An optical model that describes the increment of scattered light intensity due to molecular adsorption on a refractive index-matched porous material was previously derived by scattering models of spheres coated by a thin shell with different refractive index[32,33]. Remarkably, for pore radius bigger than about 100 nm, the model for the scattered light intensity is formally identical to that for the light reflected by a thin layer between two media with similar refractive indices derived by Fresnel equations[24,26]. The intensity *I* of light scattered (or reflected) by a thin layer of thickness *h* is given by:

$$\frac{I}{I_0} = 1 + \left(\frac{h}{h^*}\right)^2 \tag{7.1}$$

where I_0 is the scattered light intensity in the absence of the layer and h^* corresponds to the layer thickness yielding to $I = 2I_0$. Equation 7.1 enables to convert the measured intensity of scattered light into the dimensionless parameter h/h^*, which is related to the amount of molecules adsorbed on the inner surface of the membrane. An absolute quantification of h is obtained through an estimate of the value of h^*, which depends on the refractive indices of the membrane (n_m), of the solution (n_s) and of the adsorbed molecular layer (n_l) by[26]:

$$h^* = \left|\frac{n_m^2 - n_s^2}{n_l^2 - n_s^2}\right| \frac{1}{k} \tag{7.2}$$

where $k = 4\pi n_s \sin(\Theta_s/2)/\lambda$ is the scattering vector and Θ_s is the angle between the incident and the scattered rays. For the materials and the optical set-up used in this study $h^* \approx 1.45$ nm. In order to analyse the experimental data, a background contribution due to stray-light I_f is subtracted from the measured intensity to obtain I, which then is converted into h through Equation 7.1.

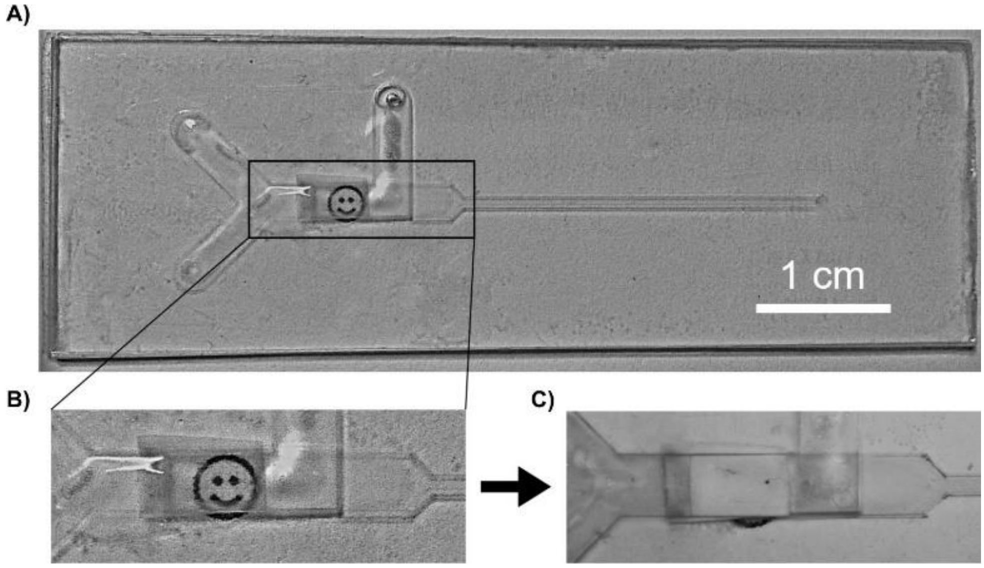

Figure 7.6: A) Image of the fabricated device. B) Enlarged view of the part hosting the membrane soaked with water and C) dried.

7.3 Results and Discussion

7.3.1 Membrane Configuration in the Microfluidic Device

To prevent the rapid clogging of the membrane, a cross-flow configuration was adopted. In fact, in this configuration just a portion of the water sample passes through the membrane, ensuring a longer lifetime of the membrane, which is one of the desirable characteristics of an autonomous and disposable sensor to be used for environmental analysis at the point of need. The first generation of the microfluidic device, although operative, was fast replaced by the second generation to have a bigger membrane surface for the detection of the scattered light. In the second generation, one of the channels was modified, as well, from a parallel to a diagonal configuration to facilitate the collection of the sample after passing through the membrane. The second generation of the microfluidic device was found to be suitable for testing samples containing a cationic surfactant (see Figure 7.7 A). After testing with increasing surfactant concentration two different areas of deposition were appreciated (Figure 7.7 B) onto the membrane. As the values obtained for the scared light were not homogeneous all over the membrane surface the second generation design was discarded as well. The third and final generation of the microfluidic device was developed in order to avoid all the limitations found in the previous designs.

The final microfluidic device configuration shown in Figure 7.6 exploits the membrane filtration capability in a cross-flow geometry, in which the inlet flow from the upper channel is split in part through the membrane towards the bottom channel and in part remains in the upper channel. In this way, the particles that are filtered out, such as solid particles or microorganisms, are pushed away by the tangential flow of the upper channel and do not clog the membrane pores. The lengths and cross sections of the outlet channels are designed to balance the hydrodynamic resistance of the membrane and obtain similar fluxes from the two outputs.

This microfluidic design provides a wide optical access to the area of the membrane, hence enabling to illuminate its surface and to collect the scattered light from a large angular range. Moreover, no edges are present in the optical path of the illumination light, limiting the background from stray light. In fact, this design enables an efficient acquisition of the light scattered by the membrane, providing, through Equation 7.1, a direct optical detection of compounds when retained in the membrane during the flow, such as surfactants, oils or organic molecules.

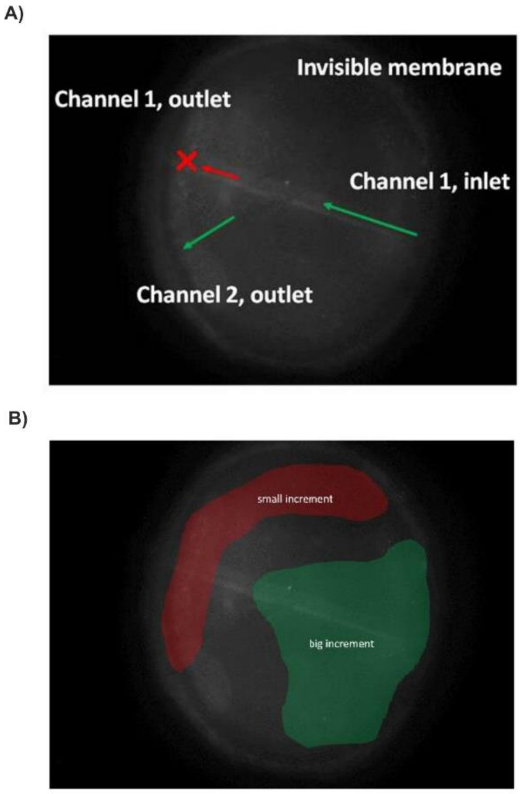

Figure 7.7: A) Picture of the increment of the scattered light of the membrane captured with a CCD camera in a continuous flow. B) Two differentiated surfactant deposition areas. Red: small-scattered light increment. Green: big-scattered light increment.

7.3.2 Optical Response to Surfactant Adsorption

The perfluorinated microporous membrane embedded in the microfluidic device yields a label-free SPI optical signal upon adsorption of molecules present in the sample solution. The membrane material combines the high optical transparency in water with the hydrophobicity typical of perfluoropolymers. Compounds with a hydrophobic moiety, such as surfactants, were retained on the inner surface of the membrane and the formation of a thin layer with a refractive index higher than the membrane material and the solution induces an increase of scattered light intensity according to Equation 7.1. The microfluidic design provides a wide optical access to the area of the membrane, hence enabling to illuminate its surface and to collect the scattered light from a large angular range using an imaging system. The subsequent washing with pure water enables desorption of the molecules from the membrane and induces a decrease of scattered light intensity until the initial condition was recovered. The signal obtained with clean water represents a reference and the quantification of surfactant concentration was achieved from the rate of increase of the scattered light intensity upon concentration to the sample flow. The effective thickness *h* of the adsorbed layer obtained by cycling sample and reference flows is reported in Figure 7.8. The flow rate through the membrane was maintained at 150 µL min^{-1} to enable a rapid response time upon the injection of the sample. Figure 7.8A shows that if the sample solution does not contain surfactants, the optical signal measured from the membrane does not change upon alternating the flows, as expected. In contrast, a concentration as small as 0.5 µM of cationic surfactant SBSAC induces a clear modulation of the light scattering signal (Figure 7.8B). The intensity of the scattered light increases almost linearly in correspondence to the sample flow and decreases with pure water, indicating that surfactants are desorbing from the inner surface of the membrane. An observation time of about 10 - 20 min is sufficient to clearly detect the signal associated with each switch of the sample solution. With a higher concentration of surfactant of about 4 µM, the measured signal increases more rapidly and tends to reach a larger asymptotic value of *h* (Figure 7.8C). Alternated flows of the sample solution and pure water yield to a cyclic oscillation of the optical signal, whose average amplitude and response time depend on the concentration of adsorbing molecules in the water sample. Therefore, the membrane embedded into the microfluidic device acts as optical label-free SPI sensor making directly visible both molecular adsorption and desorption. The relative standard deviation of the amplitude *h* for a single cycle is about 25 % but the accuracy can be increased through repeated cycles of adsorption and desorption.

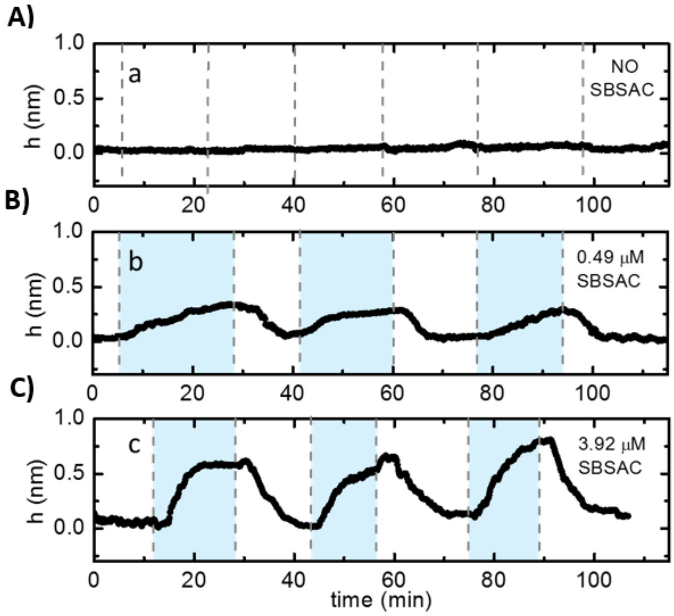

Figure 7.8: Surfactants detection and regeneration of the device. Subsequent injection of surfactant (light blue) and pure water (white) were performed at the flow rate of 150 µL min^{-1}.

A) Injections of pure water representing the baseline signal. B) Injection of 0.49 µM of SBSAC and C) 3.92 µM of SBSAC alternated to pure water. The highest concentration of surfactant yields a higher and faster increase of the adsorbed layer thickness.

The effective thickness *h* of the molecular layer represents a quantification of the amount of adsorbed molecules. A simple approach to interpreting the amplitude and kinetics of this quantity upon changes of the surfactant concentration, *c,* in solution can be derived by the Langmuir model for adsorption[34]. Accordingly, the adsorption curves display an exponential growth behaviour as a function of time t[24]:

$$h = h_{eq}\left(1 - e^{-\Gamma t}\right) \tag{7.3}$$

The asymptotic value h_{eq} depends on the concentration *c* and on the equilibrium constant for desorption K_d as

$$h_{eq} = \frac{h_0}{1 + \frac{K_d}{c}} \tag{7.4}$$

where h_0 is the plateau value of *h* at high concentrations. The rate Γ of the exponential growth depends on the observed kinetic rate constants for adsorption and desorption, k_{on} and k_{off}, respectively, as

$$\Gamma = k_{on}c + k_{off} \tag{7.5}$$

where $k_{off}/k_{on} = K_d$. The value of k_{on} and k_{off} depend on the intrinsic kinetic rates of the molecule-surface interaction as well as on the transport of molecules into the membrane[26]. Figure 7.9 shows that the adsorption and desorption curves expressed in terms of the effective thickness *h* of the adsorbed molecular layer correlate with the surfactant concentration *c* according to this model. For $c < K_d$ the exponential curves for adsorption and desorption have a similar rate given by $\Gamma \approx k_{off}$. For $c > K_d$ the rate of the adsorption curve increases with *c*, whereas the desorption rate of a rapid decrease of concentration from *c* to zero is always k_{off}. The measured rates are coherent with the extracted value of K_d that determines the asymptotic amplitude of the curve through Equation 7.4 from the fit of these data, the values of $h_0 = 1.2 \pm 0.3$ nm (n = 5), $K_d = 3 \pm 1$ µM (n = 5), $k_{on} = 900 \pm 190$ M^{-1} s^{-1} (n = 5) and $k_{off} = 0.0030 \pm 0.0006$ s^{-1} (n = 5) are obtained. These values can be compared to those obtained studying the adsorption interaction on a prism made of Hyflon AD® immersed in a cuvette[26]. In that case, the extracted desorption constant was about 0.16 µM, indicating a stronger interaction between the surfactant and the prism surface relative to the membrane surface, and h_0 was about two-fold higher, suggesting that a complete coverage of the inner surface was achieved[35]. In fact, the production process of the prism and the membrane are very different. The prism was made by moulding and its surface was mechanically polished, whereas the membrane is produced by non-solvent induced phase separation and its inner surface is only cleaned through repeated washing with ethanol. The higher affinity of the prism suggests a surface interface and porosity to the membrane due to the differences in the fabrication protocols. However, despite the higher value of K_d, the membrane investigated here provides a clear signal for surfactant concentrations as low as 0.5 µM. Accordingly, higher affinities and hence higher sensitivities are expected to be achievable also with the membrane through the optimisation of the production and cleaning processes.

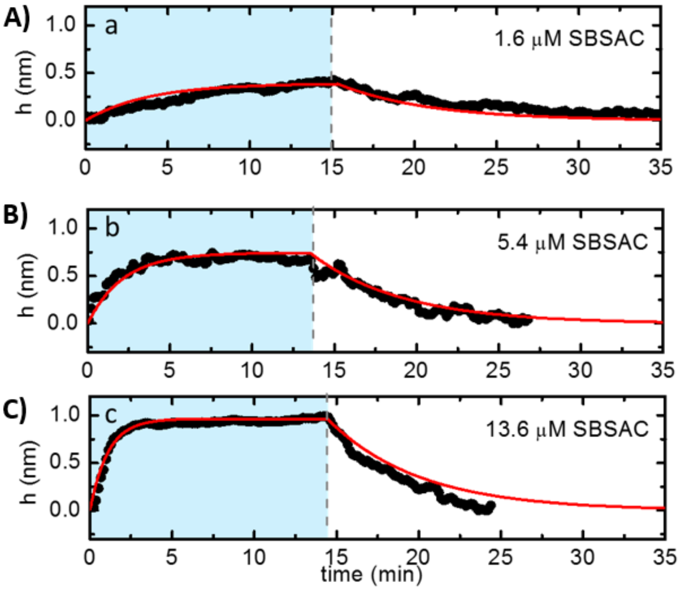

Figure 7.9: Characterisation of adsorption parameters. Adsorption and desorption of surfactant were studied using a pseudo-first-order kinetic model. Increasing concentrations of surfactant (light blue), 1.6 µm (A), 5.4 µm (B), 13.6 µm (C), were injected into the device and followed by a washing step with water (white). The red curves represent the fit with the exponential functions obtained by the model.

7.3.3 Performance of the Method with River Samples

The cross-flow design of the microfluidic device enables the analysis of samples even if they contain particles because the particles larger than the membrane pores are filtered out by the tangential flow directed to the upper channel outlet. To prove this concept, the device was tested with real river water collected from the Lambro river, nearby the city of Milano. Inspection by optical microscopy showed a high amount of particles with a size smaller than 10 µm, corresponding to about 10^7 particles mL^{-1} (Figure 7.10 A and B). Despite this, no clogging of the membrane was observed after about an hour of flow at 150 µL min^{-1}, and it was observed that the value of the flow in both outlets was constant during measurement.

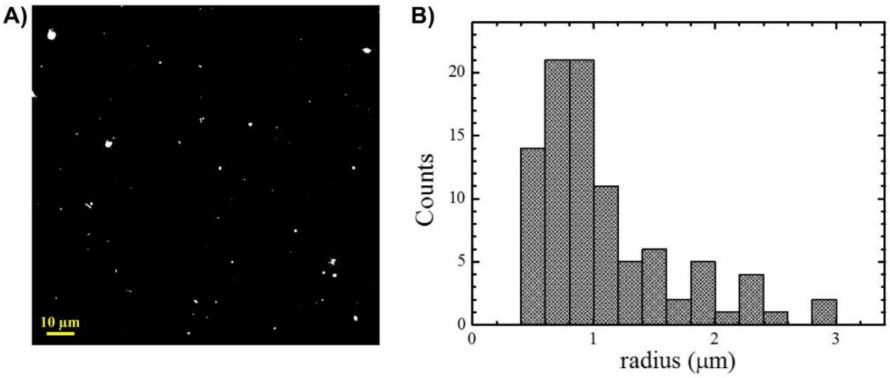

Figure 7.10: Particle characterization of river water samples. (A) Dark field image of a water sample collected at site 1 (Ponte Albiate, Italy) placed in a capillary tube. The contrast of the image is enhanced to improve the visualization. (B) Size distribution of the particles observed in the image of panel A.

Upon injection of the river water sample, an increase of the intensity of the light scattered by the membrane was observed, as shown in Figure 7.11 A. The increase of the optical signal indicates the formation of an adsorbed layer on the inner surface of the membrane. The effective thickness of this layer reached a plateau of about h = 0.2 nm after 5 min. This signal was compared with that induced by the SBSAC surfactant by injecting a reference sample with a concentration of 7 µM after the river water sample (Figure 7.11 A). In this case, the optical signal has higher amplitude, corresponding to a larger amount of adsorbed molecules. From the analysis of these curves through the adsorption model and parameters obtained above, the effective thickness of the adsorbed layer of compounds present in the river sample would correspond to a concentration of about 1 µM of the cationic surfactant SBSAC used as reference. After the injection of the reference sample of the surfactant, the flow of pure water induced desorption of the molecules and enabled the regeneration of the membrane sensor before another measurement cycle.

The analysis was repeated on river water collected from the same river in a different site. The first site was upstream the city (Ponte Albiate) and the second is downstream (Melegnano). The signals obtained for the two samples are reported in Figure 7.11 B. The sample collected downstream has larger amplitude and faster rate, hence indicating a larger number of adsorbing molecules, in agreement with the expected increase of pollution after passing the urban area. The analysis based on the reference surfactant yielded to an estimated concentration of about 4 µM for the second collection site, corresponding to a four-fold increase relative to the upstream site. These experiments demonstrate the feasibility of using the membrane sensor device to monitor the content of pollutants in real river water samples, without the need of preparation steps or reagents. Nevertheless, it needs to be considered that other substances present in the river, which are not pollutants, could be detected as well.

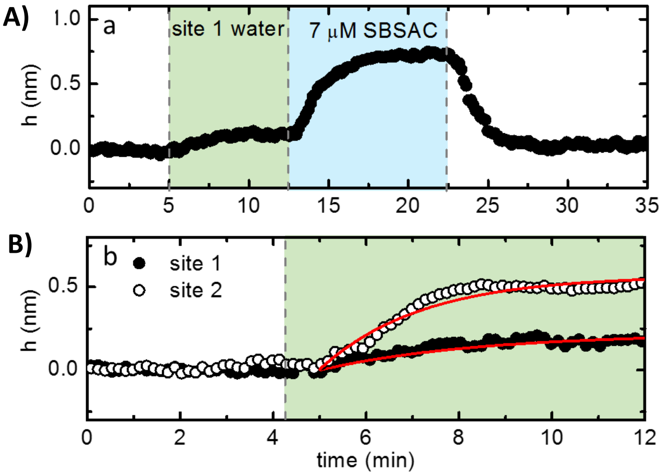

Figure 7.11: Surfactant detection in real river water samples. A) River water (light green) was injected into the device, and then a spike of a reference sample containing 7 µM of SBSAC was performed. Then, the microfluidic device was cleaned with pure water. B) The responses obtained from samples collected at two different locations are compared. The red curves represent the fit using the adsorption parameters extracted from the data of Figure 7.6 and with c = 1 µM (black dots) and c = 4 µM (white dots).

7.4 Conclusions

This chapter has described the fabrication and testing of a novel hybrid microfluidic device embedding a perfluorinated membrane with a refractive index similar to that of water. The membrane was placed across two channels in order to filter the sample solution in a cross-flow configuration. Additionally, the refractive index matching with the solution enables to achieve the SPI conditions and to effectively amplify the optical scattering signal measured upon adsorption of molecules on the inner surface of the membrane. The use of an extremely simple optical set-up, which allows for the real-time signal collection, enables a non-specific quantification of the concentration of adsorbing substances, mainly pollutants, in water samples. The device represents a new concept of microfluidic label-free SPI optical sensor with filtering capability. The repeated adsorption and desorption of a cationic surfactant at different concentrations, down to 0.5 μM was demonstrated as a proof of concept. This concept was applied to the analysis of real river water collected at two different sites. Despite the large amount of particulate matter, the analysis of the river water demonstrated the effectiveness of the adopted microfluidic cross-flow design to avoid the clogging of the membrane. Therefore, this system could enable the real-time continuous monitoring of water substances without the need of, for instance, pre-treatment of the sample and without the use of reagents. These features are extremely important to develop a new generation of low-cost autonomous platforms for large-scale environmental monitoring. Further developments of this device are expected to enhance the specificity of detection by functionalising the inner surface of the membrane or by adding a spectral analysis of the optical signal without affecting the main features of the system.

7.5 References

1 D.Y. Lee, H. Lee, J. T. Trevors, S. C. Weir, J. L. Thomas, and M. Habash, *Water Res.*, 2014, 53, 123–131.
2 S. D. Richardson and S. Y. Kimura, *Anal. Chem.*, 2016, 88, 546–582.
3 S. D. Richardson and T. A. Ternes, *Anal. Chem.*, 2014, 86, 2813–2848.
4 S. Rebello, A. K. Asok, S. Mundayoor, and M. S. Jisha, *Environ. Chem. Lett.*, 2014, 12, 275–287.
5 A. R. S. Ross and X. Liao, *Anal. Chim. Acta*, 2015, 889, 147–155.
6 E. Olkowska, Ż. Polkowska, and J. Namieśnik, *Talanta*, 2013, 116, 210–216.
7 F. Hernández, M. Ibáñez, T. Portolés, M. I. Cervera, J. V. Sancho, and F. J. López, *J. Hazard. Mater.*, 2015, 282, 86–95.
8 M. Marchetti and I. Durickovic, *IET Sci. Meas. Technol.*, 2014, 8, 122–128.
9 Y. Zhao and X. Li, *Sens. Actuators B, Chem.*, 2015, 209, 258–264.
10 C. Xing, L. Liu, S. Song, M. Feng, H. Kuang, and C. Xu, *Biosens. Bioelectron.*, 2015, 66, 445–453.
11 C. Sicard, C. Glen, B. Aubie, D. Wallace, S. Jahanshahi-Anbuhi, K. Pennings, G. T. Daigger, R. Pelton, J. D. Brennan, and C. D. M. Filipe, *Water Res.*, 2015, 70, 360–369.
12 T. G. Aw and J. B. Rose, *Curr. Opin. Biotechnol.*, 2012, 23, 422–30.
13 K. Yang, H. Peretz-Soroka, Y. Liu, and F. Lin, *Lab Chip*, 2016, 16, 943–958.
14 J. C. Jokerst, J. M. Emory, and C. S. Henry, *Analyst*, 2012, 137, 24–34.
15 J. Gorbatsova, M. Jaanus, M. Vaher, and M. Kaljurand, *Electrophoresis*, 2016, 37, 472–475.
16 K. F. Lei, in *Microfluidics in Detection Science*, Royal Society of Chemistry, Cambridge, Ed: F. H. Labeed, H. O Fatoyinbo, 2014,1–28.
17 M. F. Maitz, *Biosurf. Biotribol.*, 2015, 1, 161–176.
18 R. P. Gandhiraman, C. Volcke, V. Gubala, C. Doyle, L. Basabe-Desmonts, C. Dotzler, M. F. Toney, M. Iacono, R. I. Nooney, S. Daniels, B. James, D. E. Williams, *J. Mater. Chem.*, 2010, 20, 411-416.
19 J. Saez, J. Etxebarria, M. Antoñana-Diez, and F. Benito-Lopez, *Sens. Actuators B, Chem.*, 2016, 234, 1–7.
20 R. Byrne, F. Benito-Lopez, and D. Diamond, *Mater. Today*, 2010, 13, 16–23.
21 M. Czugala, R. Gorkin III, T. Phelan, J. Gaughran, V. F. Curto, J. Ducrée, D. Diamond, and F. Benito-Lopez, *Lab Chip*, 2012, 12, 506-509.
22 G. Zanchetta, R. Lanfranco, F. Giavazzi, T. Bellini, and M. Buscaglia, *Nanophotonics*, 2017, 6, 627-645.
23 M. Czugala, C. Fay, N. E. O'Connor, B. Corcoran, F. Benito-Lopez, and D. Diamond, *Talanta*, 2013, 116, 997–1004.
24 F. Giavazzi, M. Salina, R. Cerbino, M. Bassi, D. Prosperi, E. Ceccarello, F. Damin, L. Sola, M. Rusnati, M. Chiari, B. Chini, T. Bellini, and M. Buscaglia, *Proc. Natl. Acad. Sci.*, 2013, 110, 9350–9355.
25 D. Prosperi, C. Morasso, F. Mantegazza, M. Buscaglia, L. Hough, and T. Bellini, *Small*, 2006, 2, 1060–1067.
26 R. Lanfranco, F. Giavazzi, M. Salina, G. Tagliabue, E. Di Nicolò, T. Bellini, and M. Buscaglia, *Phys. Rev. Appl.*, 2016, 5, 54012.
27 J. de Jong, R. G. H. Lammertink, and M. Wessling, *Lab Chip*, 2006, 6, 112-115.
28 F. Evenou, J.M. Di Meglio, B. Ladoux, and P. Hersen, *Lab Chip*, 2012, 12, 171-177.
29 F. Tasselli, in *Encyclopedia of Membranes*, Springer Berlin Heidelberg, Berlin, Heidelberg, Ed: E. Drioli**,** L. Giorno, 2014, pp. 1–3.
30 J. Saez, L. Basabe-Desmonts, and F. Benito-Lopez, *Microfluid. Nanofluid.*, 2016, 20, 116.
31 J. Elizalde, M. Antoñana, L. Matthys, F. Laouenan, and J. M. Ruano-López, in *International Conference on Miniaturised Systems for Chemistry and Life Sciences, MicroTAS, 2013*, 2013, 790–792.
32 H. C. van de Hulst, *Light Scattering by Small Particles*, Dover, New York, Opt. Comm, 1957.
33 R. Piazza and V. Degiorgio, *Opt. Commun.*, 1992, 92, 45–49.
34 I. Langmuir, *J. Am. Chem. Soc.*, 1918, 40, 1361–1403.
35 B. Zhao, C. W. MacMinn, and R. Juanes, *Proc. Natl. Acad. Sci.*, 2016, 113, 10251–10256.

8

Integration of Microporous Materials II: Phantom Microbeads for Pollutants Detection in Water*

This Chapter describes the proof of concept of the integration of perfluorinated microbeads with refractive indexes similar to that of water, hosted in a novel multilayer cyclic-olefin polymer microfluidic device, for the easy a non-invasive optical detection of surfactants in water in a continuous mode.

---

*Parts of this Chapter have been published in: J. Saez; R. Lanfranco; M. Buscaglia; F. Benito-López, Phantom microbeads chromatography column in microfluidics, *20th International Conference on Miniaturized Systems for Chemistry and Life Sciences, MicroTAS 2016*, 2016, 1366-1367.

8.1 Introduction

As explained in previous Chapters water pollution is one of the biggest concerns of society. Among all water pollutants, oils and surfactants are especially harmful to human health and the environment and they should be continually monitored to avoid water contamination[1]. Therefore, it would be extremely important to develop analytical systems capable of continuous and extensive monitoring of the quality of water[2]. In analytical laboratories, liquid chromatography and mass-spectroscopy are widely employed approaches for sensing and further determination of contaminants in liquids and solubilised media, as it was mentioned in Chapter 7.

Microfluidics have emerged as environmental analysis platforms enabling autonomous rapid detection and identification at the point of need (see Chapter 2). Therefore, microfluidic devices are an alternative to more conventional equipment for improving sensing techniques at the point of need, bringing laboratory equipment to the site.

In the context of microfluidics for environmental, biological and pharmaceutical applications, emulsification methods have been used to generate emulsions that will interact or release an analyte with time[4, 5]. Among the different emulsification methods described[6], membrane emulsification[7] is a simple method that has received increasing attention over the last 10 years, with potential applications in many fields such as in separation science as it was explained in Chapter 7. The method consists of a dispersed phase (fluorinated oil) that is forced through the pores of a porous membrane, while a continuous phase (water + surfactants) flows along the membrane surface. Droplets grow at pore outlets until they detach with a certain size. The size of detachment depends on the balance between the drag force on the droplet from the flowing continuous phase, the buoyancy of the droplet, the interfacial tension forces and the driving pressure. The final droplet size and size distribution are not only determined by the pore size and size distribution of the membrane, but also by the degree of coalescence, both at the membrane surface and in the bulk solution. Multiple parameters can affect the characteristics of the resulting emulsion, *e.g.* polydispersity and average pore size, membrane type, average porosity, crossflow velocity, transmembrane pressure, and choice of emulsifier[8].

The combination of microfluidics and perfluorinated materials[9] into microfluidic devices could be an interesting approach for pollutants detection in water. Therefore, this chapter delves into this new concept of the integration of phantom microbeads packed as conventional columns in microfluidic devices for the sensing of different refractive index solution mixtures as demonstrated in Chapter 7. The material is a perfluorinated polymer alike to the one presented in Chapter 7, in this case, named Fomblin MD40®.

8.2 Experimental

8.2.1 Materials and Equipment

For the preparation of the membrane, Fomblin MD40® was generously donated from Solvay Specialty Polymers (Bollate, Italy). CIBA Irgacure 651 was purchased from Sigma-Aldrich (Madrid, Spain). Sodium dodecyl sulphate was purchased from Sigma Aldrich (Milan, Italy).

For the fabrication of the microfluidic device Zeonor COP sheets from Zeonex (Jena, Germany) and Pressure Sensitive Adhesive from Adhesive Research (Limerick, Ireland) were used. A Graphtec FC8000-60 cutting plotter was used for cutting COP and PSA structures (Graphtec®, USA). The microfluidic device was connected to an Elvefow system, (Paris, France) and a flow sensor from Sensirion (Stäfa, Switzerland) by female and male luer connectors from ChipShop (Jena, Germany) and PEEK and PTFE tubing from VICI Valco Instrument (TX, USA) of 1/32" and 1/16", respectively.

A custom optical apparatus to measure the intensity of light scattered by the microbead column was designed and set-up on an optical board using optomechanical components purchased from Thorlabs (Newton, NJ, USA). The light of a LED with a peak wavelength of 592 nm was purchased to Lumileds (Suresnes, France) and a CCD camera to Stingray Allied Technology (Stadtroda, Germany).

8.2.2 Phantom Microbeads Fabrication

In order to obtain the best microbeads to be integrated into the chromatography column, several conditions are required:

1. Microbeads should not be monodisperse, to avoid optical complications such as diffraction or structure-related features that can complicate the optical analysis;
2. but they should not be extremely polydisperse, to avoid liquid flow problems within the column (such as percolation or formation of preferential flow channels).

The best situation for our purpose is to obtain polydispersed microbeads capable of generating an improved optical modeling of the porous substrate.

A membrane emulsification method was applied to produce the microbeads[10, 11]. This specific method generates quite monodisperse droplets (less than 12 %) of uniform size quickly. Moreover, it is also possible to choose the average size of the droplets by selecting the appropriate membrane.

The dispersed phase that contains the Fomblin MD40® (Figure 8.1) and 0.1 % wt of CIBA IrgaCure 651 as photoinitiator was pumped under gas pressure at 11 bar through the pores of an SPG membrane (10.1 µm) into the SDS aqueous continuous phase (% wt), which flows across the centre of the membrane. The resulting droplets had a quite wide polydispersity, probably due to the high emulsification pressures required by the high viscosity of the Fomblin MD 40®. Microbeads were UV polymerised for 10 min at 500 W, keeping the emulsion under low stirring. After polymerisation, the microbeads were washed with MilliQ water, obtaining a low light scattering. The generated microbeads had a diameter of 16 ± 4 µm, measured from microscope images of the sample with the help of the ImageJ software (see Figure 8.2). A good chemical stability in water and mechanical resistance of the microbeads were observed after the fabrication process, remaining stable for several months after production.

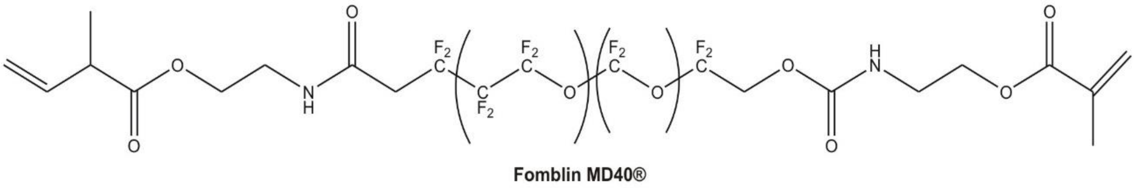

Figure 8.1: Fomblin MD® chemical structure.

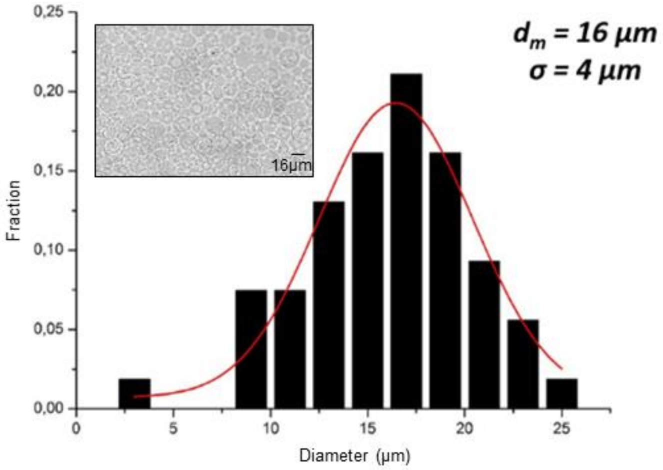

Figure 8.2: Histogram of the size diameter distribution of the microbeads in the emulsion, and a picture of the microbeads (inset).

8.2.3 Microfluidic Device Design and Fabrication

Two different designs and fabrication protocols for the microfluidic device were tested. The first microfluidic device was fabricated with five xurographied 100 µm COP layers bonded together by the *Origami* technique, as explained in Chapters 3 and 4, and bonded by thermocompression. The design consisted of three inlets (to prevent blocking) that converged in a 1 mm width channel of 300 µm height and 5 cm length, which thinners to 100 µm close to the outlet in order to retain the phantom microbeads as chromatography columns depicted in Figure 8.3.

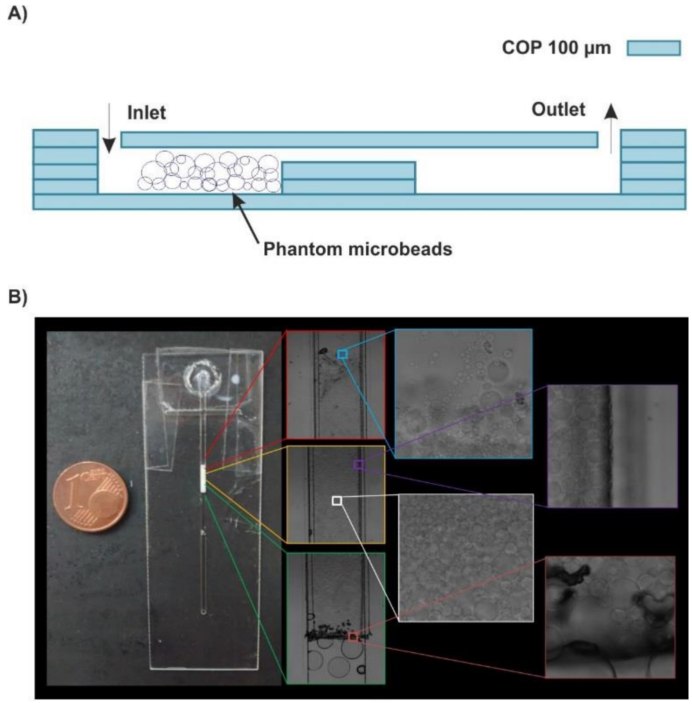

Figure 8.3: A) Cross section structure of the first generation of the microfluidic device (not in scale). B) Microfluidic device with an integrated phantom microbeads column and a zoom picture containing the packed phantom microbeads (X5, X20 magnification, 1 mm channel width).

The second and final generation of the device was fabricated with nine layers of 100 µm COP, as explained above. This microfluidic device was designed with three inlets (3 mm diameter) (to prevent blocking) that converged in a 3 mm width channel of 500 µm height and 5 cm length, which thinners to 100 µm close to the outlet in order to retain the phantom microbeads as a chromatography column (Figure 8.4). To make the microfluidic device more robust, two layers of COP, one on the top and another on the bottom, were added and, therefore, prevented the microfluidic device to crack when high pressures were applied.

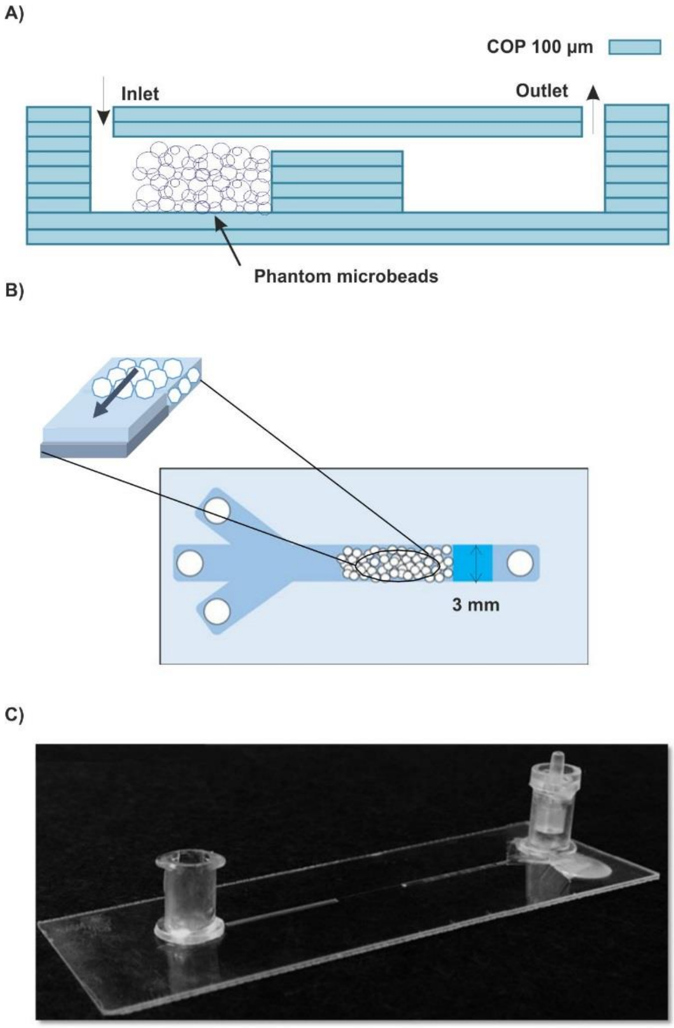

Figure 8.4: A) Cross section structure of the second generation of the microfluidic device (not in scale). B) Top view scheme of the microfluidic device with an integrated phantom microbeads column. C) Microfluidic device with coupled female (inlet) and male Luer (outlet) connectors.

8.2.4 Optical Set-up and Measurement Protocol

A custom optical apparatus to measure the intensity of light scattered by the phantom microbeads was designed and set-up on an optical board using optomechanical components, as shown in Figure 8.5. The light of a red LED with a wavelength of 625 nm was collimated and shaped to reduce the stray light contribution, possibly originated by reflections from the edges of the channels. A lens collects the back-scattered light at about 45° relatively to the transmitted beam and forms an image of the microbeads column surface on a CCD camera to monitor the scattered light intensity. A LabView (National Instruments) program registers the images captured by the CCD camera at a speed of 1 fps. The images were then analysed using the ImageJ software (National Institutes of Health) as follows: the contrast was adjusted in the same way for all the data collected and a moving average was performed over 5 frames to reduce the noise. Then, the averaged intensity of the image acquired from the microbeads column was computed as a function of time.

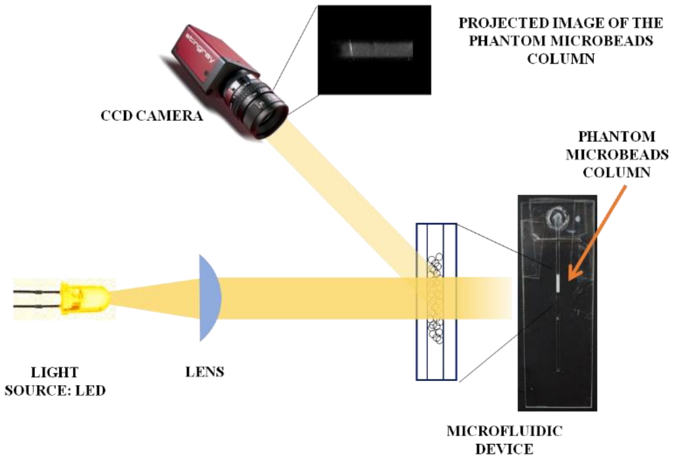

Figure 8.5: Optical set-up used to study the scattered light produced by the phantom microbeads column. It is composed of a light LED source, lens, the microfluidic device and a CCD camera.

The intensity of the light scattered by the phantom microbeads and acquired by this optical set-up provides a quantification of the molecular adsorption on the inner surface of the microbeads, in a similar way to what was explained in Chapter 7. Experiments were performed using water/glycerol mixtures. The surfactant was dissolved in deionised water. All the experiments were performed at room temperature 25 °C. After each experiment, the tubes and connectors of the fluidic system were washed with fresh water.

8.3 Results and Discussion

8.3.1 Configuration of the Microfluidic Device

The phantom microbeads were constricted into the microfluidic device whose design ensures no clogging. Inside the microfluidic channel, a wall with a passage narrower than the average colloids diameter is created. The fabrication material of choice, COP, allows the light pass through due to its high transparency. In this way, the surfactant monitoring and detection could be done inside the microfluidic device by using an optical scattering signal that changes due to surfactants presence in the flowing water.

The microfluidic device was proven to resist up to 1 bar of pressure during experimental conditions due to the two extra layers of COP (top and bottom). No cracks or leaking were observed during experiments when using this configuration.

8.3.2 Test of the Microbeads Column for Surfactant Detection

The optical set-up presented in the experimental section allows for the detection of surfactants in water. First, the microfluidic device was placed in the optical set-up and connected to an Elveflow system to manipulate the liquid at high pressure. Thanks to the geometry of the microfluidic device and the optical set-up, it is possible to see the liquid sample passing through the column and to monitor the scattered light intensity generated by the sample (see Figure 8.6). The intensity of the scattered light was measured using the same protocol described in Chapter 7, when different concentrations of glycerol/water solutions flowed through the phantom microbeads chromatography column, as a proof of principle.

Figure 8.6: Shows the measuring of the scattered light of the colloids inside the microfluidic device.

For instance, when different mixtures of glycerol/water were injected, the scattering light changes due to the refractive index difference between the phantom microbeads and the solution. These data are collected in Table 1 and Figure 8.7. This enables the characterisation of the optical response of the device, which is required for the use of the system to quantify molecular pollutants in real water samples, as it was performed in Chapter 7.

Table 1. Increasing concentrations (% w/w) of glycerol/water mixtures and their respective refractive index.

Glycerol/Water (% w/w)	Refractive index (η)
1	1.3342
4	1.3376
8	1.3424
12	1.3472
16	1.3521

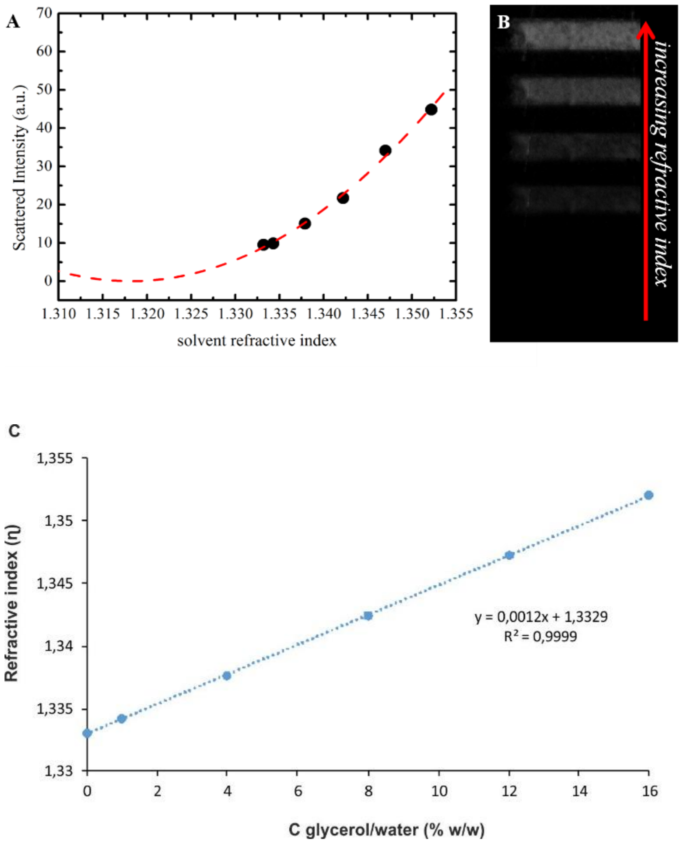

Figure 8.7: A) Normalised scattered intensity as a function of the soaking solvent's refractive index for different glycerol/water increasing concentrations. B) Increment of the scattered light captured by the CCD camera (background subtracted) from the microbeads column. C) Linear tendency of glycerol/water mixtures with the refractive index.

8.4 Conclusions

This Chapter described, for the first time, the fabrication of a microfluidic device with an integrated invisible column that potentially could optically detect pollutants in water, as a proof of concept. Glycerol/water mixtures were monitored using a scattering technique with a simple, homemade optical detection set-up. This could open the possibility of using these types of microfluidic devices in real scenarios for the detection of surfactants in rivers at the point of need.

The optical set-up can be further optimised and miniaturised, while real water samples polluted with surfactants will be tested, as in the case of the membrane presented in Chapter 7.

8.5 References

1 T. Ivankovic and J. Hrenovic, *Archvs. Ind. l Hyg. Toxic.,* 2010, 61, 95-100.
2 F. Long, A. Zhu and H. Shi, *Sensors,* 2013, 13, 13928-13948.
3 H. Weil and T. I. Williams, *Nature,* 1950, 166, 1000-1001.
4 C. Charcosset, *In Membrane Processes in Biotechnology and Pharmaceutics,* 2012.
5 E. Piacentini, M. Dragosavac and L. Giorno, *Curr. Pharm. Des.,* 2017, 23, 302-318.
6 Z. Cui, E. Drioli and Y. M. Lee, *Prog. Polym. Sci.,* 2014, 39, 164-198.
7 S. M. Joscelyne and G. Trägårdh, *J. Memb. Sci.,* 2000, 169, 107-117.
8 M. Destribats, S. Gineste, E. Laurichesse, H. Tanner, F. Leal-Calderon, V. Héroguez and V. Schmitt, *Langmuir,* 2014, 30, 9313-9326.
9 R. Lanfranco, F. Giavazzi, M. Salina, G. Tagliabue, E. Di Nicolò, T. Bellini and M. Buscaglia, *Phys. Rev. App.,* 2016, 5.
10 C. Charcosset, I. Limayem and H. Fessi, *J. Chem. Technol. Biotechnol.,* 2004, 79, 209-218.
11 C. Charcosset and H. Fessi, *Rev. Chem. Eng.,* 2005, 21, 1-32.

9

Ionogel-based Nitrite and Nitrate Handheld Sensor Device*

The increment of uncontrolled nutrients concentration in water is the subject of increasing environmental concern. In particular, the increment of nitrate causes the eutrophication of algae, leading to fauna and flora demise. To favour an easy and adequate monitoring of this environmental problem, an ionogel-based sensor was developed for the image analysis detection and colorimetric determination of nitrite and nitrate in water. The sensor consists of a small poly(methyl)methacrylate device cut by a CO_2 laser ablation system where both, the detection and the calibration zones are integrated. A simple photograph of the whole device, followed by colour processing of the different sections of the device was used for the determination of nitrite concentrations.

*****Parts of this Chapter have been patented in: J. Saez, F. Benito López, Dispositivo microfluídico portátil para detectar nitrito-nitrato, University of the Basque Country, Spain, P201631376, 26/10/2016.

9.1 Introduction

In recent years, important environmental monitoring developments have appeared in response to the increasing contamination of natural, industrial and municipal waters by toxicants and water pollutants such as harmful chemical agents. As in the case of surfactant pollutants (Chapters 7 and 8), the determination of nutrients concentration in water bodies is very important because it directly affects to water life equilibrium. The increment of uncontrolled nutrients concentration in water could lead to environmental modifications. The increment of nitrate causes toxicity to human health and marine life degradation such as eutrophication of algae and uncontrolled increase of algae blooms, leading to flora and fauna destruction[1]. One example of eutrophication of algae can be found in the eastern part of the Minor Sea salty lagoon in Spain where a variety of green and red algae species, among others[2], coexist.

Therefore, the constant monitoring of nitrate concentrations in continental waters can be considered as a preventive action that could help environmental agencies in the protection of the environment. These institutions normally operate using physical sampling and transportation to well-equipped facilities where the analysis is carried out by highly trained personnel, using sophisticated instrumentation. This strategy benefits obtaining very precise and accurate results and adjusts to regulatory legal proceedings. In contrast, unpractical and outmoded techniques are sometimes used, and most of the time expenses associated with maintaining all these facilities, instrumentation and personnel lead to bulky costs. The use of microfluidic technologies could help approaching water monitoring to society by the implementation of low cost and practical, easy to use devices.

An integrated microfluidic device can perform biological or chemical processing, where sampling, pretreatment, and analysis can be carried out in a single device. Since the first description presented by Manz *et al.*[3], lab on a chip (LOC) devices are being in constant development and can be explained by simply shrinking an entire laboratory to a chip format. LOC devices offer many practical advantages compared to other traditional analytical platforms; for example, the reduced dimensions of microfluidic components allow for the manipulation of small volumes of fluids which leads to less reagent consumption, reduced costs, and less waste generation, as described in previous Chapters.

Current nitrate detection techniques include electrochemical[4, 5], capillary/column[6, 7], and biosensing[8], among others. However, spectrophotometric methods are the most popular by far, due to the excellent limits of detection (nanomolar), wide dynamic range and cost efficiency[9]. In this sense, the spectrophotometric assay based on the Griess reagent[10] has been very popular for over a century. The colorimetric determination of nitrite by the Griess reagent is chemically robust, offers excellent analytical performance and has been applied in the development of several analytical microfluidic platforms[11-13]. However, these microfluidic platforms are usually complicated devices consisting of reagents reservoirs, pumps, valves and detector modules making the final platform expensive and/or not adequate for on-site use. As an example, Czugala *et al.* [14] developed a wireless microfluidic analytical platform consisting in a cradle that holds the microfluidic device, a variety of LEDs for the actuation of photoresponsive valves and a wireless Paired Emitter-Detector Diode (PEDD). Computer and batteries were also necessary. Cogan *et al.*[15, 16] developed a platform for the direct determination of nitrate using chromotropic acid in natural waters. The fully integrated sensing platform consists of a sample inlet with filter, storage units for the chromotropic reagent and standards for self-calibration, a pumping system which controls the transport and mixing of the sample, a microfluidic mixing and detection device, and waste storage, all contained within a ruggedised, waterproof housing. The optical detection system consists of a light emitted diode (LED) light source with a photodiode detector, which enables sensitive detection of the formation of coloured complexes.

Consequently, it is possible to obtain nitrite and nitrate concentration determination in water samples from an accurate and precise measurement of its colour change after the Griess or another similar type of coloured reaction occurs. Therefore, the possibility of analysing colour in an easy and portable manner would reduce device fabrication and so analysis costs. In this regards, video and photo analysis of colour is becoming an important way of sensing for novel analytical devices, but mostly demonstrated for paper-based microfluidics. For instance, Lopez-Ruiz *et al.*[17] used a smartphone for the detection of nitrite in paper-based microfluidic devices.

Colour can be accurately defined by three chromaticity parameters: lightness (*L*), redness (*a*) and yellowness (*b*). The *L* value refers to the measurement of the lightness or the amount of light reflected, *a* value indicates the intensity of the red (positive values) or green (negative values) coloration, while the *b* value displays the intensity of the yellow (positive values) or blue (negative values) coloration. Other widely used colour space is the *LCH* system, which uses L, Chroma (*C*), and Hue angle (*H*) parameters. *C* is related to the intensity or saturation of the colour, and *H* is linked to the name of the colour (red, blue, yellow)[18]. Measurement of the *L, a* and *b* chromaticity parameters can be afforded by digital image analysis after appropriate calibration by the implementation of an easy application and can be converted to the *LCH* space by Equations 9.1 and 9.2 (see section 9.2.3[19]).

On the other hand, smart materials have been gaining increasing attention due to their autonomous behaviour in response to changes in their local environment[20] without human manipulation[21], as the examples presented in Chapters 4, 5 and 6. In particular, hydrogel materials are a kind of smart materials that respond to the external agent by uptaking (swelling) or releasing (shrinking) a large quantity of water, which leads to an abrupt change in their structural volume. However, the practical applicability of hydrogels in microfluidic devices is limited due to their discrete shrinking with increasing temperature, low material robustness, rather slow expansion kinetics and degree of actuation, as explained before. All these drawbacks lead to look for alternatives such as ionogels. The use of ionogels improves the physical robustness of the stimuli-responsive gel[22] (see Chapter 5). Moreover, the low vapour pressure of ionic liquids and their ability to plasticise the gel polymer structure permits long-term reagent storage[23]. Up to now, ionogels have been used mostly as valves or pumps (see Chapter 5) to minimise costs and avoid human manipulation[24, 25]. Also, it was described that IL such as thiosalicylate-based IL are capable of binding to a variety of metals such as cupper (II) and cobalt (II) for the fabrication of an optode membrane for metals sensing[26].

The aim of the work presented in this Chapter is to propose a methodology for the colorimetric detection and determination of nitrite and nitrate in water samples by using ionogel-based sensors that incorporate the Griess reagent in its polymer matrix in a portable, easy to use hand-held device configuration.

9.2 Experimental

9.2.1 Materials and Equipment

For the synthesis of the ionogels, *N*-isopropylacrylamide (NIPAAm), *N,N'*-methylene-bis(acrylamide) (MBAAm), 2,2-Dimethoxy-2-phenylacetophenone photoinitiator (DMPA) and, 1-ethyl-3-methylimidazolium ethyl sulfate (IL-1) and trihexyltetradecyl-phosphonium dicyanamide (IL-2) ionic liquids were purchased from Sigma-Aldrich (Madrid, Spain).

Sodium nitrate and sodium nitrite stock solutions were purchased to Sigma-Aldrich (Madrid, Spain).

Whatman Filter paper with Grade 595 and metallic zinc (Zn^0), both from Sigma-Aldrich (Madrid, Spain) were used to fabricate the paper-based nitrate reduction area.

1 mm thickness poly(methyl)methacrylate (PMMA) slides were purchased from Goodfellow (Huntingdon, UK). The fabrication of the devices was carried out using a CO_2 laser ablation system from Universal Laser Systems (Vienna, Austria). The UV light source used for photopolymerisation was a BONDwand UV-365 nm obtained from NEI Corporation (Somerset, NJ, USA). UV-Vis spectra were recorded on a UV-Vis-NIR Perkin-Elmer Lambda 900 spectrometer (Madrid, Spain).

The surface images of the ionogel were obtained by FEI Quanta 2000 low vacuum scanning electron microscope (SEM) (Hillsboro, OR, USA) system at an accelerating voltage of 20 kV, with magnification values of 70×.

Pictures were taken with a Canon EOS 1000D model camera and calibrated by using X-rite card with the Colour-Checker Passport v. 1.0.2 program, both from X-Rite Inc. (Grand rapids, MI, USA) and followed by Photoshop CC program from Adobe Systems Inc. (Mountain view, CA, USA) image analysis.

9.2.2. Preparation of the Ionogels

Two different ionogels were synthesised by mixing the NIPAAm monomer (2.00 mmol), the MBAAm (0.04 mmol) crosslinker and the photoinitiator DMPA (0.02 mmol) in a molar ratio 100:2:1 and dissolved in 1 mL of IL-1 or IL-2. The mixture was stirred and heated to 45 °C for approximately 10 min. The reaction mixture solution was pipetted into the reservoirs (3 µL each) of the PMMA device and the gels were photopolymerised at 365 nm (1600 mW cm^{-2}) for 10 min at 8 cm distance from the reservoirs. The ionogels were thoroughly washed three times with ultrapure water and ethanol to get rid of the non-polymerised ionogel excess. Then, the 1-ethyl-3-methylimidazolium ethyl sulphate (IO-1) and the trihexyl tetradecyl-phosphonium dicyanamide (IO-2) ionogels were embedded with the Griess reagent and left to dry for 12 h. The chemical structures of the components of the ionogels are illustrated in Figure 9.1.

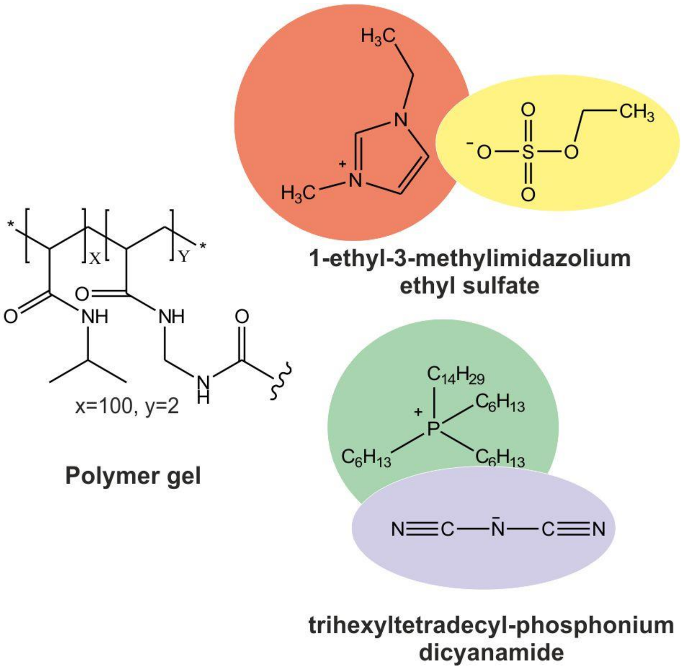

Figure 9.1: Chemical structure of the components of the ionogel. Left: polymer gel based on NIPAAm and MBAAm; top right: 1-ethyl-3-methylimidazolium ethyl sulphate IL; bottom right: trihexyl tetradecyl-phosphonium dicyanamide IL.

9.2.3 Handheld Device Fabrication

The device was envisioned as a single sensor unit where sample injection, chemical reactions, and analyte detection take place in a run. The sensor was fabricated in PMMA material and cut by CO_2 laser ablation. Each sensor was designed with five calibration reservoir points, 5 mm^2 each and a "key-shape" paper-based microfluidic reservoir for combined nitrite and nitrate determination, composed by a square reservoir of 5 mm^2 (N2) and a channel of 4 mm length, 1 mm width that ends in a 2 mm diameter inlet.

Further modifications of the device were realised to detect separately nitrite and nitrate. Two new reservoirs were added to the microfluidic device, one for the detection of nitrite in the sample (N1) and another for the evaluation of the matrix effect of the sample (M). The device has 1 mm total thickness, 22 mm and 10 mm size and each reservoir is 25 mm^2 size.

In both configurations, the nitrate present in the sample can be easily revealed by reducing it to nitrite with metallic Zn^0, which oxidises to Zn^{2+}, as the value of nitrite after reduction of the sample minus the value of the nitrite sample (N2-N1). An emulsion of Zn^0 in ultrapure water was deposited within a paper channel and placed in the "key-shape" channel (4 mm length, 1 mm width) as shown in Figure 9.2.

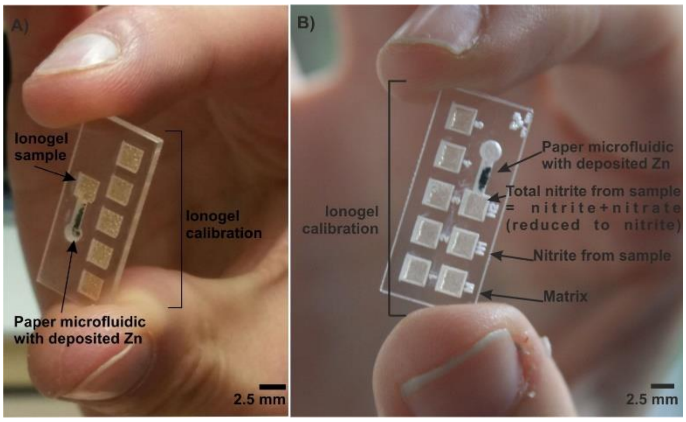

Figure 9.2: Pictures of the ionogel-based nitrate sensors. (A) First generation of the sensor, which consists of five calibration ionogel points and a sample ionogel reservoir connected to a paper-based microfluidic with deposited Zn^0. (B) Second generation of the sensor, which consists of five calibration ionogel points (1-5), a matrix ionogel point (M) and nitrite from sample (N1) and nitrate (N2) (nitrite from sample plus reduced nitrite from the nitrate present in the sample) ionogel reservoirs, where N2 is connected to a paper-based microfluidic with deposited Zn^0.

9.2.4. Measurement Protocol

Three pictures were taken from each device. A neutral grey paper that completely filled the viewfinder was selected as background for all the pictures. All the pictures were taken with a standard digital camera. Each picture was taken including the device and an X-Rite ColorChecker Passport card placed on the background for the colour calibration as shown in Figure 9.3. The camera image plane was placed leveled in parallel to the plane of the device and the chart colour card. Once all was set, a properly exposed photographic image was shot with the camera, which was set to store the raw-mode and JPG pictures at once.

Figure 9.3: Picture of the device obtained using the X-Rite ColorChecker Passport card as the colour standard for further calibration.

All pictures taken in raw-mode were calibrated before further use. Calibration is necessary for any standard camera to assure the accuracy of the colours[27]. Therefore, a camera profile that characterises the camera sensor was obtained using the program Colour-Checker Passport v. 1.0.2 and the photo information was modified with this profile in Photoshop CC. Photographs were calibrated with the CR_Calibrator_CC24 JavaScript Photoshop plug-in and checked with the Read_Colors_CC2 JavaScript plug-in[28]. During the calibration process, the chromaticity values of the 24 patches of the X-Rite ColorChecker Passport card accurately known were compared with those of the patches shown in the image taken of the device and of the card. In this way, the script opens the image multiple times modifying the Photoshop colour sliders and selecting the settings that best fit all of them. A visual layer of the card colours was created to check that the calibration was successful, showing the theoretical and measured colours together. Once the calibration is finished, the raw calibrated image was saved in JPG format to be used in the following steps.

Each picture in JPG format was opened in the Photoshop CC program to estimate the representative chromaticity values (*L*, *a* and *b*, which could be taken for each point of the image) of each reservoir. After discarding the background and those parts of the picture affected by shadows and reflections, a centered point of 3x3 pixels was selected for each picture and their *L*, *a* and *b* values were measured. The average of each chromaticity parameter was considered to be representative of the colour of the sample in the picture. The corresponding chroma (*C*) and hue (*H*) parameters were calculated according to Equations 9.1 and 9.2[18].

$$C = \sqrt{\left(a^2 - b^2\right)} \tag{9.1}$$

$$H = \arctan\left(a/b\right) \tag{9.2}$$

9.3 Results and Discussion

9.3.1 Fabrication of the Devices and Ionogel Integration

The xurography method of cyclic olefin polymer (COP) followed by thermocompression was considered due to its fast and cheap fabrication protocol[29]. Nevertheless, this method was observed to be tedious to generate a large amount of these type of devices since the reproducibility was sometimes low due to the misalignment of the reservoirs and channel through several layers. Therefore, it was decided to use PMMA and CO_2 laser ablation. The reservoirs and channel of the device were successfully aligned with a good consistent reproducibility from device to device.

The volume of the photopolymerised ionogel highly affects the degree of its swelling, and consequently, its capability to retain more liquid. Volumes of less than 3 µL are not sufficient to fill the reservoir, while volumes bigger than 3 µL swell too much during hydration and so the ionogel peels out from the reservoir. Thus, 3 µL of solution were chosen for the 25 mm^2 reservoirs, while for the reservoir with the channel 6 µL of solution were necessary. Ionogels were photopolymerised under UV light as soon as they were drop-casted into the reservoirs. Several photopolymerisation times and ionogel solutions were investigated to generate a homogeneous, well-spread, porous structure. The ideal polymerisation times for each ionogel were 15 and 10 min for IO-1 and IO-2, respectively. It was observed that with this protocol ionogels were retained in the reservoir even after hydration; therefore, no surface functionalisation was necessary to covalently attach the ionogels to the device reservoirs.

9.3.2 Ionogels Characterisation

Both ionogels are porous and able to accommodate large volumes of water. Nevertheless, the dicyanamide anion of the IL of IO-2 strongly bonds with water molecules as demonstrated by Gallagher *et al.*³⁰, generating a more stable ionogel structure to embed the Griess reagents and, at the same time, to accommodate in its structure the water which contains nitrite/nitrate for detection. Moreover, IO-2 swells less than IO-1 generating a more stable structure in the reservoirs of the device[31].

SEM pictures of the surface of the IO-2 with and without the embedded Griess reagent were obtained (Figure 9.4). The presence of the Griess reagent changes the morphology of the polymer matrix structure. In Figure 9.4 A, the IO-2 presents a homogeneous swollen structure, while in Figure 9.4 B, as it is clearly observed that globular and porous microdomains appear over the swollen structure of the ionogels due to the presence of the Griess reagent embedded in the IO-2 matrix.

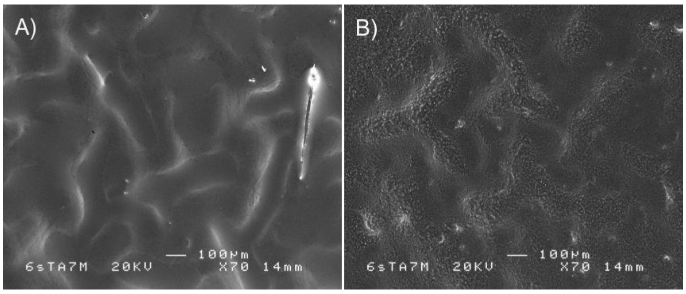

Figure 9.4: SEM images of the surface of the IO-2 taken with 70x magnification A) without Griess reagent and B) with Griess reagent.

UV-Visible spectra of both ionogels with the embedded Griess reagent and after the reaction with nitrite were taken. The maximum absorbance for the formation of the coloured azo dye from the Griess reaction with nitrite was found to be 532 nm in both ionogels (see Figure 9.5). Figure 9.6 clearly shows that both ionogels present similar values of absorbance but, since the IO-1 is not transparent, the background value is much higher, thus being a worse candidate for the colorimetric analysis of NO_2 than the IO-2.

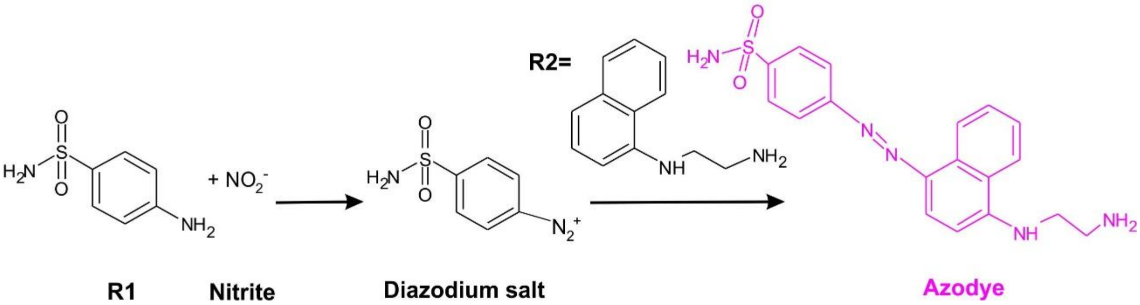

Figure 9.5: Representation of the Griess reaction with nitrite. Sulphanilamide (R1) reacts with nitrite to form a diazodium salt that in presence of *N*-(1-naphthyl) ethylendiamine (R2) forms the pink azo dye.

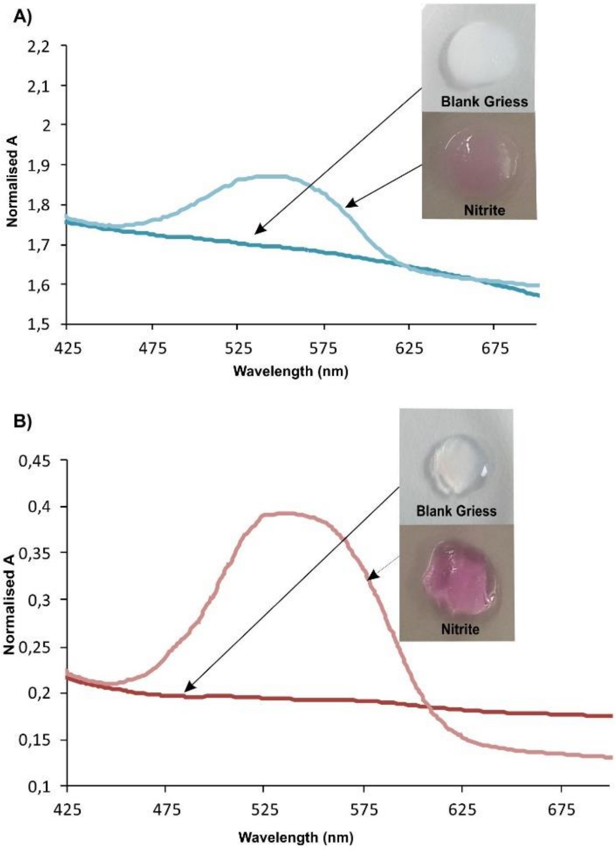

Figure 9.6: UV/Vis spectra of A) IO-1 with Griess reagent and after reaction with nitrite; and B) IO-2 with Griess reagent, and after reaction with nitrite. Inside: pictures of the ionogels before and after reaction of Griess reagent with nitrite.

9.3.3 Performance of the Sensor

As a proof of principle, nitrite calibration solutions were prepared in the linear range of 0-10 ppm, as explained in the experimental section, and 3 µL of each were added to the five reservoirs of the calibration section of the device. After 30 min of incubation, distinguishable shades of pink-orange colour were observed for each of the added nitrite concentration. Then, the nitrate sample was added to the inlet reservoir placed just before the key-shaped reduction section formed by the paper-based microfluidic containing the Zn^0. The sample moved towards the ionogel sensing area (M2) by the paper capillarity forces, revealing a final orange colour in the reservoir. The colour comes from the Griess reaction with the nitrite, which was generated after reduction of the nitrate with Zn^0 in the paper-based microfluidic section of the device.

Then, image treatment of the calibration area and the N2 sample reservoir, following the protocol explained in the experimental section, was carried out.

The Partial Least Squares PLS1 calibration model[32] was constructed from the *L, a, b* data obtained for the five calibration samples placed in the corresponding reservoirs in the device. These data have been collected in Table 9.1.

Table 9.1: Data used for the construction of the PLS1 model for the determination of nitrite concentration using the devices described in this Chapter.

[NO_2^-] (mg L^{-1})	***L***	***a***	***b***
0	62	4	7
2.5	61	3	8
5	61	3	9
7.5	63	2	8
10	65	1	6
Sample	60	2	7

As an example of the quality of the calibration models obtained using this multivariate approach, Figure 9.7 presents the calibration and validation lines obtained with the data in Table 9.1 showing the agreement between the real (Measured) and predicted values of the dependent variable in the model, in this case, the nitrite concentration. As it can be appreciated, the measured and the predict concentrations are close to each other.

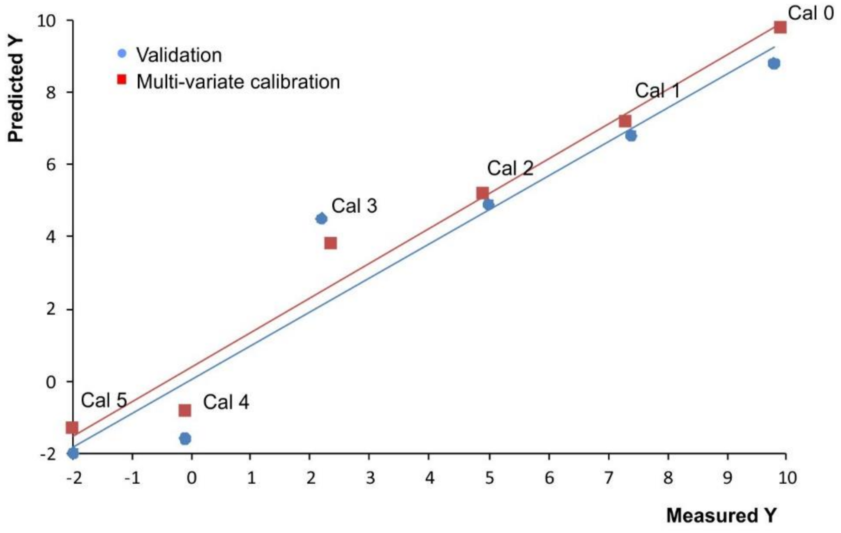

Figure 9.7: Multivariate calibration model (red) and validation (blue) curves generated after image analysis of the Cal 5 (0 mg L^{-1}), Cal 4 (2.5 mg L^{-1}) Cal 3 (5 mg L^{-1}), Cal 2 (7.5 mg L^{-1}) and Cal 1 (10 mg L^{-1}) nitrite solutions.

After the application of this model to the first generation of the device, the results showed a concentration of 5.0 ± 0.5 mg L^{-1} of nitrate in the sample reservoir, which agrees well with the spiked solution of 5.0 ppm of nitrate added at the inlet of the device.

9.4 Conclusions

In this Chapter, the design, fabrication, characterisation and preliminary performance of an ionogel-based nitrate/nitrite sensor integrated into a hand-held device with a paper-based microfluidic section have been carried out. The sensor uses a colorimetric Griess reagent method for the determination of nitrite, and theoretically nitrate, in water samples, integrated into the ionogel matrix. As a result, it was preliminary proven that nitrite and nitrate concentrations could be determined accurately by image analysis with a further calibration of a taken picture.

Further developments of the sensor will tend to facilitate the simultaneous nitrite and nitrate detection and analysis by a smartphone with an image analysis application. The device will facilitate both nitrite and nitrate concentration determination at the point-of-need with this cheap, portable, and reagent manipulation free device.

9.5 References

1 M. F. Chislock, E. Doster, R. A. Zitomer and A. E. Wilson, *Nature Edu Knowledge,* 2013, 4, 10-12.

2 J. García-Pintado, M. Martínez-Mena, G. G. Barberá, J. Albaladejo and V. M. Castillo, *Sci. Total Environ.,* 2007, 373, 220-239.

3 A. Manz, N. Graber and H. M. Widmer, *Sens. Actuators B, Chem.,* 1990, 1, 244-248.

4 M. P. N. Bui, J. Brockgreitens, S. Ahmed and A. Abbas, *Biosens. Bioelectron.,* 2016, 85, 280-286.

5 J. Liang, Y. Zheng and Z. Liu, *Sens. Actuators B, Chem.,* 2016, 232, 336-344.

6 G. Persichetti, G. Testa and R. Bernini, *Sens. Actuators B, Chem.,* 2015, 732-739.

7 S. Cho, T. S. Park, T. G. Nahapetian and J. Yoon, *Biosens. Bioelectron.,* 2015, 74, 601-611.

8 M. Sohail and S. B. Adeloju, *Talanta,* 2016, 153, 83-98.

9 M. Shariati-Rad, M. Irandoust and M. Haghighi, *Int. J. Environ. Sci. Technol.,* 2015, 12, 3837-3842.

10 B. F. Rider and M. G. Mellon, *Ind. Eng. Chem., Anal. Ed.,* 1946, 18, 96-99.

11 A. D. Beaton, C. L. Cardwell, R. S. Thomas, V. J. Sieben, F. Legiret, E. M. Waugh, P. J. Statham, M. C. Mowlem and H. Morgan, *Environ. Sci. Technol.,* 2012, 46, 9548-9556.

12 G. Persichetti and R. Bernini, *Talanta,* 2016, 155, 145-152.

13 X. Wang, M. R. Gartia, J. Jiang, T. Chang, J. Qian, Y. Liu, X. Liu and G. L. Liu, *Sens. Actuators B, Chem.,* 2015, 209, 677-685.

14 M. Czugala, C. Fay, N. E. O'Connor, B. Corcoran, F. Benito-Lopez and D. Diamond, *Talanta,* 2013, 116, 997-1004.

15 D. Cogan, J. Cleary, T. Phelan, E. McNamara, M. Bowkett and D. Diamond, *Anal. Methods,* 2013, 5, 4798-4804.

16 D. Cogan, C. Fay, D. Boyle, C. Osborne, N. Kent, J. Cleary and D. Diamond, *Anal. Methods,* 2015, 7, 5396-5405.

17 N. Lopez-Ruiz, V. F. Curto, M. M. Erenas, F. Benito-Lopez, D. Diamond, A. J. Palma and L. F. Capitan-Vallvey, *Anal. Chem.,* 2014, 86, 9554-9562.

18 J. M. Pereira-Uzal, *Gestion del Color en procesos de digitalizacion*, Marcombo, Barcelona, 2013.

19 O. Liñero, M. Cidad, G. Arana, C. Nguyen and A. de Diego, *Microchem. J.,* 2017, 134, 284-288.

20 R. Byrne, F. Benito-Lopez and D. Diamond, *Mater. Today,* 2010, 13, 16-23.

21 B. Ziólkowski, L. Florea, J. Theobald, F. Benito-Lopez and D. Diamond, *Soft Matter,* 2013, 9, 8754-8760.

22 F. Benito-Lopez, M. Antoñana-Díez, V. F. Curto, D. Diamond and V. Castro-López, *Lab Chip,* 2014, 14, 3530-3538.

23 M. Tijero, R. Díez-Ahedo, F. Benito-Lopez, L. Basabe-Desmonts, V. Castro-López and A. Valero, *Biomicrofluid.* 2015, 9 .

24 M. Czugala, C. Fay, N. E. O'Connor, B. Corcoran, F. Benito-Lopez and D. Diamond, *Talanta,* 2013, 116, 997-1004.

25 T. Akyazi, J. Saez, J. Elizalde and F. Benito-Lopez, *Sens. Actuators B, Chem.,* 2016, 233, 402-408).

26 A. Kavanagh, R. Byrne, D. Diamond and A. Radu, *Analyst,* 2011, 136, 348-353.

27 H. Y. Cao, T. Li, R. Dong and H. Zhou, *3rd Int. Conf. Info. Sci. Control Eng. (ICISCE),* 2016, 54-58.

28 R. Gardner, Adobe Photoshop ACR Calibration Scripts, 2010.

29 J. Saez, J. Etxebarria, M. Antoñana-Diez and F. Benito-Lopez, *Sens. Actuators B, Chem.,* 2016, 234, 1-7.

30 S. Gallagher, A. Kavanagh, B. Zíolkowski, L. Florea, D. R. Macfarlane, K. Fraser and D. Diamond, *Phys. Chem. Chem. Phys.,* 2014, 16, 3610-3616.

31 T. Akyazi, N. Gil-González, L. Basabe-Desmonts, E. Castaño, M. C. Morant-Miñana and F. Benito-Lopez, *Sens. Actuators B, Chem.,* 2017, 247, 114-123.

32 K. H. Esbensen, *Multivariate data analysis in practice*, CAMO Software AS, Oslo, 2006.

10

Final Remarks and Future Work

10.1 Final Remarks and Future Work

Researchers are currently working on the development of low-cost microfluidic devices for the environmental monitoring and assessment of the quality of our waters at the point where this information is needed. Ideally, these systems should make accurate measurements and report the results, wirelessly, to the place where they are demanded. This possibility can automatically speed up actuation protocols for preventing damage to the environment. In this regard, microfluidic devices able to detect chemical compounds or molecules of biological interest have been proven to operate easily and autonomously, which is one of the main requirements for on-site analysis. Moreover, it is clearly demonstrated in Chapter 3, that the use of biocompatible plastic polymers such as COP, PSA, and PMMA for device fabrication reduce the price of the final systems, making them also very attractive for mass production. One of the main drawbacks of the above-presented platforms is the requirement of conventional elements such as valves, pumps, reagent storage containers, and energy outputs, for running samples.

To overcome these limitations, the results presented in this thesis demonstrate the great potential derived from the use of smart materials such as hydrogels, poly(ionic liquid)s and ionogels as sensors and as actuators for fluidic control and sensors. The *in-situ* generation of a biocompatible calcium alginate microvalve inside a microfluidic device (see Chapter 4) has efficiently proven to behave as an actionable microvalve at mild temperatures allowing for flow control. Moreover, alginate microvalves can be easily erased with an ethylendiamine-tetraacetic acid (EDTA) solution, ensuring the reusability of the whole device. These microvalves are low cost to produce in terms of materials, and their *in-situ* fabrication and removal open the possibility of creating large arrays of microvalves in complex microfluidic structures. However, the presented work is just a proof-of-concept and repeatability tests should be done to enhance its implementation in real platforms. Moreover, the design of the microfluidic device has not been completely optimised yet. A quantitative step for the applicability of this technology will arise when the valve can be fabricated or removed independently from the main microfluidic channel. This could be performed by generating an extra channel for the $CaCl_2$ solution. This will ensure that all the solutions that form/erase the alginate actuator ($CaCl_2$, sodium alginate and EDTA) are independently controlled.

The possibility of using hybrid p(*N*-isopropylacrylamide) p(NIPAAm) with spirobenzopyran (SP) refer as (p(SPNIPAAm)) ionogels as actuators in Lab-on-a-Disc (LoaD) devices was demonstrated in Chapter 5. This could have important implications in the practical implementation of disc-based microfluidics in real scenarios, as it potentially opens the way towards the generation of LoaD microfluidic systems in which the photonic actuation stimulus can be totally separated from the reagents, which is compatible with a freely spinning disc configuration. It also opens the possibility of multiple-use of these valves, by re-swelling the p(SPNIPAAm) ionogel with an acidic solution in a controlled manner. This configuration increases the toolbox of microfluidic components previously developed by Czugala *et al*.[1]. Despite the promising results obtained, the repeatability of the photo-responsive actuator is not proven yet. To finalise this work, repeatability and reproducibility tests would need to be carried out and the implementation of analytical applications, such as the nitrite determination by the Griess method, would be a nice test-bed. In addition to this, recent publications have presented new materials that do not need the addition of the HCl solution to protonate the spiropyran derivative. For instance, the work published by Ziolkowski, *et al*.[2] has showed a new poly(*N*-isopropylacrylamide)-based photoresponsive gel containing copolymerised spiropyran as the photo-switch and an acrylic acid as the proton source. These types of materials could be integrated within the LoaD configuration presented in Chapter 5 and generate a simpler microfluidic device, thus reducing the manufacturing price and increasing the ease of operation.

Tributylhexyl phosphonium sulfopropyl acrylate ionic liquid monomer was used in this work to produce a poly(ionic liquid) hydrogel based actuator. In contrast with alginate microvalves and photo-switchable actuators, this hydrogel is thermoresponsive (see Chapter 6). The thermoactuation process was repeated six times with good performance, thus suggesting the possibility of using these types of actuators for more than six times. Although the repeatability of the poly(ionic liquid) hydrogel based actuator has been demonstrated, improvements in the design of the microfluidic device could be done by reducing the dimensions of the actuator or generating an actuator that is not in direct contact with the main channel, likely by integrating it with a protective membrane. Moreover, a more sophisticated microfluidic device could be generated by increasing the number of valves in the microfluidic or by changing the actuator configuration shape.

Until now, most of the platforms remain as first prototypes since it is easy to produce functional devices without considering the price of the final platform. Among other possible challenges, effective flow control is a priority, as described in this thesis. Another factor to be considered is to provide easy storable and robust sensor devices, even reliable at remote locations.

The integration of perfluorinated polymers as membranes and colloids into microfluidic devices for surfactants detection in real water samples was demonstrated in this thesis (Chapters 7 and

8). Despite the large amount of particulate matter found, the analysis of the river water showed the effectiveness of the adopted microfluidic cross-flow design to avoid the clogging of the membrane. Therefore, the membrane microfluidic device could enable the continuous monitoring of water without the need of, for instance, pre-treatment of the sample. On the other hand, colloids were integrated like a column into microfluidic devices and glycerol/water mixtures were monitored using a scattering technique with a simple, homemade optical detection set-up. This could open the possibility of using these types of microfluidic devices in real scenarios for the detection of surfactants in rivers at the point of need. The optical set-up can be further optimised and miniaturised, while real water samples polluted with surfactants can be tested in a continuous mode, as done in the case of the membrane. Further developments of those devices are expected to enhance the specificity of the detection by functionalising the inner surface of the membrane or by adding a spectral analysis of the optical signal without affecting the main features of the system. Another possibility for enhancing robustness could be the fabrication of these type of microfluidic devices by 3D printing.

Ionogels and ionic liquids have been presented in literature as possible alternatives for reagent storage in microfluidic devices, since it was proven they could store reagents for molecules or biomolecules detection. In this sense, an ionogel-based nitrite/nitrate sensor integrated into a hand-held device with a paper-based microfluidic section was developed (see Chapter 9). The Griess reagent was stored inside the ionogel material for the colorimetric determination of nitrite and nitrate (once it has been reduced to nitrate) in water samples. To be able to detect nitrite and nitrate at the point-of-need, image analysis was successfully explored as a detection technique. Further developments of the sensor will tend to facilitate separate nitrite and nitrate detection and to ease the repetitive sample analysis using these devices by implementing, for instance, an image analysis application for smartphones or other mobile platforms. In this way, both nitrite and nitrate concentration determination at the point-of-need would be facilitated with this cheap, portable, and reagent manipulation free device.

The work presented in this Thesis it can be understood as a first step in the development of new analytical tools and in further improvements it can not be forgotten to validate the new devices, with all the analytical rigor.

10.2 References

1 M. Czugala, D. Maher, F. Collins, R. Burger, F. Hopfgartner, Y. Yang, J. Zhaou, J. Ducrée, A. Smeaton, K. J. Fraser, F. Benito-Lopez and D. Diamond, *RSC Adv.,* 2013, 3, 15928-15938.
2 B. Ziólkowski, L. Florea, J. Theobald, F. Benito-Lopez and D. Diamond, *Soft Matter,* 2013, 9, 8754-8760.

Acknowledgements

There are so many people that have contributed to this exciting moment, my Thesis defense, and I would like to thank all of them:

I would like to thank Dr. Fernando Benito López for giving me the opportunity of fulfilling a long-time dream by offering me the chance to come back to Spain to complete my doctoral studies. Your guidance, advice and help make me progress both personally and scientifically. Thank you for all of your support, understanding and humour during these last years. Also thanks for the Japanese, Indian, Greek, Lebanese, Irish, and French food… Gracias Fer! I will dare to call you my friend.☺

I would like to thank also Prof. Luis Angel Fernández Cuadrado. Luis, sin tí no hubiese llegado a este punto de mi vida, a estar a punto de doctorarme. Tú fuiste el que sembró la semilla de la investigación, y ha ido creciendo poco a poco como nuestra amistad. Además, durante todo este periodo has sido mi confidente y me has animado cuando más lo he necesitado. Gracias por esto y por ser mi amigo. PD: Te debo unas cuantas cañas…☺

I would like to thank also the people from Microfluidics Cluster UPV/EHU that I spent these last years with: Tugce, I have spent with you this experience because we started together. We both thought that three years were too far and look to us now: You are recently both a doctor and married-Teşekkür Tugce! Jaio eta Maite zer egingo duzue ni gabe? Bazkalorduan galduko zara…Eskerrik asko zure laguntza eta konfiantzagatik. Falta motako zaituztet! Sorte on Post-doctoritza eta Doctoritza-ekin. Y Gracias Enrique por hacernos tan amenos los cafés, sabes que me vuelves loca, y no de amor precisamente, pero eres un gran chico. Suerte con el doctorado! Lourdes, muchas gracias por tus buenas ideas y tu contagioso entusiasmo y talento. Nunca olvidaré el viaje a Savannah…*what happens in Savannah, remains in Savannah*…

Eta IBEA mintegiko pertsonak eskertu nahiko nituzke ere. Beti izan zarete oso abegitsuak nirekin. Asko gogoratuko naiz San Alberto, Santo Tomas eta Mungiako Jaia-en bazkariak eta farretaz!

Thanks to people from DCU (specially Larisa and Alex) and UCF for making my stays both in Dublin and Orlando more enjoyable. I will also want to thank people from NAPES Project, Dermot, Simon, Aymen, Claire, Angela, Colm, Stephanie, Amel, Marco, Roberta, Albert, Jeroen, Mark… and more!

Gracias a las personas de IK4-Ikerlan y microLIQUID: Jorge, Maria, Marta... Grandes personas, siempre dispuestas a echarte una mano. Espero volver a veros pronto!

Gracias a mi familia, a mi tía Espe y mi prima Marta, por ser las mejores amigas, consejeras, confidentes y pilares fundamentales de mi vida. Ama y Aita por el apoyo tanto en formación como moral que me habéis dado a lo largo de mi vida, por el garrote que mostráis ambos frente a la vida, por ser mi modelo a seguir y por apoyarme en todas las decisiones buenas o malas que haya tomado. A Aritz por ser el hermano más guapo de todo Euskadi (chicas está soltero) y por enseñarme a dar la importancia necesaria, sólo a los problemas que la requieran, y a aprender a vivir más el día a día, *"Carpe diem"*. Sigo trabajando en ello… Love you all!

Y por último me gustaría agradecer a mi compañero de vida durante los casi últimos 3 años. Tú, Iker Larrañaga, has aguantado de todo, has sabido celebrar y disfrutar de mis logros y me has acompañado, soportado mi mal humor y subido el ánimo en los malos momentos y siempre con una broma vacilona, algo de música y una sonrisa. Te quiero papasote!

No sé qué me deparará el destino después de leer la Tesis, quizás me lleve a otro país y con suerte me devuelva pronto, pero como dijo Jane Austen *"If adventures will not befall a young lady in her own village, she must seek them abroad".*